Simulation of Ship-Wave-Ice Interactions in the Arctic

By: Luofeng Huang

Principal supervisor: Professor Giles Thomas
Co-supervisor: Professor Guoxiong Wu

A thesis submitted for the degree

of

Doctor of Philosophy

Department of Mechanical Engineering

University College London (UCL)

2021

Declaration

I, Luofeng Huang, confirm that the work presented in this thesis is my own. Where information has been derived from other sources, I confirm that this has been indicated in the work.

Signature:

Abstract

Global climate change is presenting opportunities for new networks of maritime transportation through the Arctic. However, these sea routes are often infested by floating sea ice, which brings uncertainties to shipping operators, designers and builders.

This work aimed to develop reliable simulation approaches for shipping scenarios in the presence of sea ice and investigate the associated changes to ship calm water resistance. For this purpose, computational fluid dynamics and ice solid mechanics were combined to model the potential ship-wave-ice interactions. Specifically, models were developed to simulate the two primary scenarios of a cargo ship operating in the Arctic, respectively a waterway with floating ice floes and an open-water channel created by icebreakers. Additionally, to build understanding of the Arctic sea condition, two other models were developed simulating the interaction of ocean waves with a rigid ice floe and then an elastic ice sheet, which provided a new solver capable of modelling hydroelastic fluid-structure interactions. Based on validation against experiments, these models provided the ability to accurately predict the ship-wave-ice interactions and the ice-induced resistance changes.

Through conducting a systematic series of simulations, it was found that ice floes can increase the ship resistance by the same order of magnitude as the open water resistance, but this is strongly dictated by the ship beam, ice concentration, ice thickness and floe diameter. An open-water ice channel was found to increase the ship resistance by up to 15% compared to the situation without ice, particularly when the channel width is less than 2.5 times the ship beam and the ice thickness is

greater than 5% of the ship draught.

Moreover, this work developed a procedure to derive simple ice-resistance equations from the simulation results, enabling fast prediction of ship fuel consumption in sea ice fields and incorporation into a new Arctic Voyage Planning Tool.

Impact statement

The emerging Arctic sea routes offer shorter voyage distances compared to their traditional counterparts and provide access to rich reserves of oil, gas, mines, fishing grounds and tourism. Attracted by the unexploited resources and potential financial, time and emission savings, the shipping industry is keen on maximising the opportunities afforded by Arctic shipping. Yet, the floating ice present in the Arctic sea routes is holding back the stakeholders with navigational concerns. Therefore, reliable simulation models are required to correctly predict the ice resistance on ships, so that the industry can prepare accordingly.

Addressing this challenge, this work provided new models that can accurately simulate ship operation in floating ice floes and in open-water channels between ice sheets. The models can be applied to predict the ice resistance on a given ship. This will in turn allow naval architects to optimise ice-going vessels by comparing potential hull forms and comparing retrofits of a hull form; marine engineers to equip the vessels with adequate propulsion systems; and structural engineers to assess ice loads on a hull and plan scantlings to strengthen key areas.

The work also developed a procedure to derive a simple ice-resistance equation based on systematic simulations. During the European Union's Horizon 2020 project – SEDNA (Safe maritime operations under extreme conditions, the Arctic case), the ice resistance question was combined with open-water resistance equations to provide a quick prediction of a ship's total resistance and fuel consumption for a given ice-infested route. This facilitated a voyage planning tool that links with real-time metocean and ice data to calculate a ship's fuel consumption along potential routes, allowing ship operators to select routes with lower energy costs. This software is currently being commercialised by project partner GreenSteam.

The output of this work can also contribute to future international guidelines and regulations for polar maritime transportation. For example, based on the developed simulation approaches, associations such as the International Towing Tank Conference could develop a fuller guideline on how to model ship-wave-ice interactions. The findings regarding ice resistance on ships could help the International Maritime Organisation to extend their Polar Code to formulate advice on ship operations in floating ice floes and in open-water ice channels, and the Finnish-Swedish Ice Class Rules may do the same to expand their scenarios.

Moreover, this work provided higher education and research institutions with tools and knowledge to account for the transforming Arctic environment. As the Arctic used to be covered by continuous level ice all year round, new knowledge for the emerging ice-floe environment has been urgently required, not only for shipping, but also to gain a better understanding of global warming and how to deal with it. For example, contemporary climate models still cannot accurately predict Arctic ice evolution and global temperature change. One of the main reasons is that they need to improve the parametrisation that represents wave-ice interactions, because ocean waves propagating in the ice fields dictate the ice layout and the associated ice-reflected solar radiation. The provided computational models for wave-ice interactions could fill this gap and potentially help remedy the inaccuracies in current analytical methods.

Acknowledgements

Whilst I unexpectedly enjoyed this whole process of carrying out and presenting my PhD, this project wouldn't have existed if Professor Giles Thomas didn't possess such a keen eye and ear for what might prove valuable. Such a perspicacious and enthusiastic supervisor is what I am most grateful for. He is a remarkable coach, a terrific teacher and a wonderful editor. I learn something new in every one of our conversations and always look forward to his calls.

I have eternal gratitude to Professor Guoxiong Wu who endorsed my research potential and recommended me to retain at UCL as a PhD student. He taught me to scrutinise the mathematical and physical links that are easily overlooked behind a good-looking simulation. His rigorous and challenging attitude remains inspiring as much as humbling.

Numerous scholars have demonstrated trust in my supposed skills and provided the present work with constructive advice. They include but not limited to Jukka Tuhkuri, Hrvoje Jasak, Jonas W. Ringsberg, Philip Cardiff, Željko Tuković, Håkan Nilsson, Luke Bennetts, Mike Meylan and Yiannis Ventikos.

Several important elements should be factored into the completion of this work: the use of the UCL High Performance Computing Facility and associated support services, without which this extensive computational project wouldn't have been possible; the technical input from Minghao Li and Bojan Igrec, who didn't leave me alone with my ambitious ideas and helped me break through; the writing and presenting skills taught by Sunny Bains that not only help me interpret better but also give me confidence; the countless hours I spent in gym together with Anna

Chiara Faralli that provided much-needed fuel; and the unfailing companionship of Daniela Benites Munoz and Katherine Wang over these years, during which I got myriad helps as well as happy memories.

I am indebted to many colleagues who meanwhile are truly valued friends, especially Blanca Pena, Enrico Anderlini, Chris Ryan, Yuanchang Liu, Kang Ren, Tuomas Ruma, Chris Cassar, Rui Song, Andrea Grech La Rosa, Abbas Dashtimanesh, Faheem Rehman, Gabriela Lam, Sasan Tavakoli, Azam Dolatshah, Dimitris Stagonas, Zhiyuan Li and Yuzhu Pearl Li.

This work is fortunate to be part of a European Union's Horizon 2020 project - SEDNA: Safe maritime operations under extreme conditions, the Arctic case. I hence benefited enormously from the project experience and expert opinions; special thanks go to the SEDNA partners.

Last but not least, I am particularly grateful for the scholarships received from Lloyds Register Foundation, UCL Faculty of Engineering Sciences and China Scholarship Council.

List of publications

Journal articles as part of this work

Huang, L., and Thomas, G., 2019. Simulation of wave interaction with a circular ice floe. *Journal of Offshore Mechanics and Arctic Engineering*, 141(4).

Huang, L., Ren, K., Li, M., Tuković, Ž., Cardiff, P. and Thomas, G., 2019. Fluid-structure interaction of a large ice sheet in waves. *Ocean Engineering*, 182, pp.102-111.

Huang, L., Li, M., Romu, T., Dolatshah, A. and Thomas, G. 2020. Simulation of a ship operating in an open-water ice channel. *Ships and Offshore Structures*, pp.1-10.

Huang, L., Tuhkuri, J., Igrec, B., Li, M., Stagonas, D., Toffoli, A., Cardiff, P. and Thomas, G., 2020. Ship resistance when operating in floating ice floes: a combined CFD&DEM approach. *Marine Structures*, 74, 102817.

Huang, L., Li, Z., Ryan C., Ringsberg, J., Pena, B., Li, M., Ding, L. and Thomas, G. Ship resistance when operating in floating ice floes: derivation, validation, and application of an empirical equation. *Under Review*.

Huang, L., Igrec, B., and Thomas, G. New tools to generate natural ice floe fields for computational models. *Under Review*.

Conference proceedings as part of this work

Huang, L., 2018. An opensource solver for wave-induced FSI problems. *CFD with Opensource Software*, at: Gothenburg, Sweden.

Huang, L., Li, M., Tukovic, Z. and Thomas, G., 2018. Simulation of the hydroelastic response of a floating ice sheet. *The 13th OpenFOAM Workshop*, at: Shanghai, China.

Huang, L., Dolatshah, A., Cardiff, P., Bennetts, L., Toffoli, A., Tukovic, Z. and Thomas, G., 2019. Numerical simulation of hydroelastic waves along a semi-infinite ice floe. *The 34th International Workshop on Water Waves and Floating Bodies (IWWWFB)*, at: Newcastle, Australia.

Huang, L., Li, M., Igrec, B., Cardiff, P., Stagonas, D. and Thomas, G., 2019. Simulation of a ship advancing in floating ice floes. *the 25th International Conference on Port and Ocean Engineering under Arctic Conditions (POAC)*, at: Delft, Netherland.

Huang, L., Li, Z., Ryan, C., Li, M., Ringsberg, J., Igrec, B., Grech La Rosa, A., Stagonas, D. and Thomas, G., 2020. Ship resistance when operating in floating ice floes: a derivation of empirical equations. *The 39th International Conference on Ocean, Offshore & Arctic Engineering (OMAE)*, Virtual Conference.

Huang, L., Bennetts, L., Cardiff, P., Jasak, H., Tukovic, Z. and Thomas, G., 2020. The implication of elastic deformation in wave-ice interaction. *The 15th OpenFOAM Workshop*, Virtual Conference.

Contents

Nomenclature

α	Waterline angle
δ	Wave period
η	Free surface elevation
γ	Buttock angle
λ	Wavelength
$\mathbf{F}$	Force vector
$\mathbf{u}$	Displacement vector
$\mathbf{v}$	Velocity vector
μ	Dynamic viscosity
ν	Poisson's ratio
Ω	Torque vector
ω	Wave angular frequency
Ψ	Wave energy
ρ	Density
a	Wave amplitude
B	Ship beam at waterline

C Ice concentration

Co Courant number

D Equivalent diameter of an ice floe's upper surface

d Water depth

E Young's modulus

Fr Froude number

g Gravitational acceleration

H Wave height

h Ice thickness

k Wave number

L Length of an ice sheet

L_{pp} Ship length between perpendiculars

m Mass

p Pressure

R Wave reflection coefficient against an ice sheet

$R_{channel}$ Ship resistance in an ice channel

R_{ice} Ship resistance induced by ice

R_{ow} Ship resistance in open water without ice

R_{water} Ship resistance induced by water

T Wave transmission coefficient against an ice sheet

T_M Ship draught at midship

U Ship speed

W Width of an ice channel

6-DOF Six degrees of freedom

AIV Arctic In-service Vessel

ASPM Arctic Ship Performance Model

CFD Computational Fluid Dynamics

CSM Computational Solid Mechanics

DEM Discrete Element Method

FSD Floe Size Distribution

FSI Fluid-Structural Interaction

FSICR Finnish Swedish Ice Class Rules

FVM Finite Volume Method

ITTC International Towing Tank Conference

JBC Japan Bulk Carrier

KCS KRISO Container Ship

MIZ Marginal Ice Zone

NSR Northern Sea Route

NWP Northwest Passage

RANS Reynolds-Average Navier-Stokes

RAO Response Amplitude Operator

VOF Volume of Fluid

VPT Voyage Planning Tool

List of Figures

List of Tables

Chapter 1

Introduction

1.1 Background

With global warming, the sea ice extent in the Arctic is reducing quickly. As shown in Figure 1-1, the Arctic ice extent usually hits a maximum in March and a minimum in September [1], and satellite images have observed its summer minimum to have decreased by approximately 12% per decade [28]. According to this trend, an ice-free Arctic could appear by the middle of this century [29].

The ice reduction creates open water and leads to the notion that commercial shipping through the Arctic will be viable [30], with numerous waterways opening for travelling between continents and the Arctic, which are used to access oil, gas, mines, fishing grounds and tourism. In addition, there are two major shipping routes becoming navigable, the Northwest Passage (NWP) and the North Sea Route (NSR), which can be used as alternatives to the Panama and Suez canals to connect Europe, Asia and America [2], as illustrated in Figure 1-2. Compared to their current counterparts, both new routes can reduce the travel distance by up to 40%, signifying substantial time, cost, fuel and emissions savings [31].

There are formidable challenges coming hand-in-hand with the benefits of Arctic shipping. One of the most obvious is to understand the potential navigation environment for ships. The effects of ice reduction on the navigability of the Arctic can be more complex than anticipated. Rather than providing a pure open-ocean environment, the melting ice cover also evolves into numerous ice floes floating on the sea surface, as shown in Figure 1-3. Such ice-floe fields have been predicted to be the most ubiquitous ice condition of future Arctic [14], but its influence on ships has yet to be fully understood.

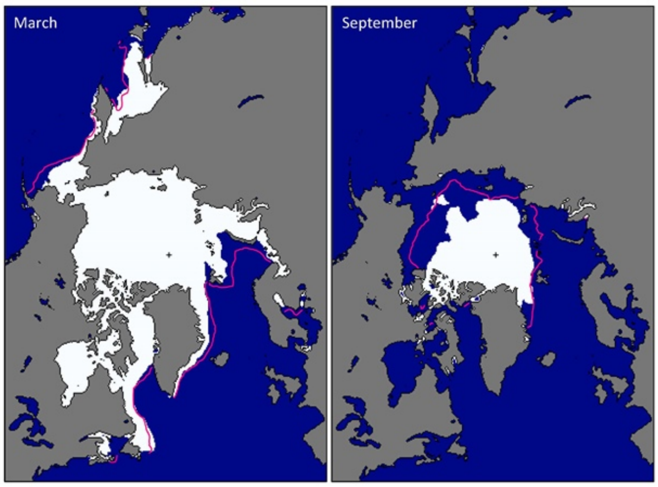

Figure 1-1: Average monthly sea ice extent in March 2016 (left) and September 2016 (right): illustrates the respective winter maximum and summer minimum extents. The coloured line indicates the median ice extent during the period 1981-2010, from which a distinct ice reduction is present [1]

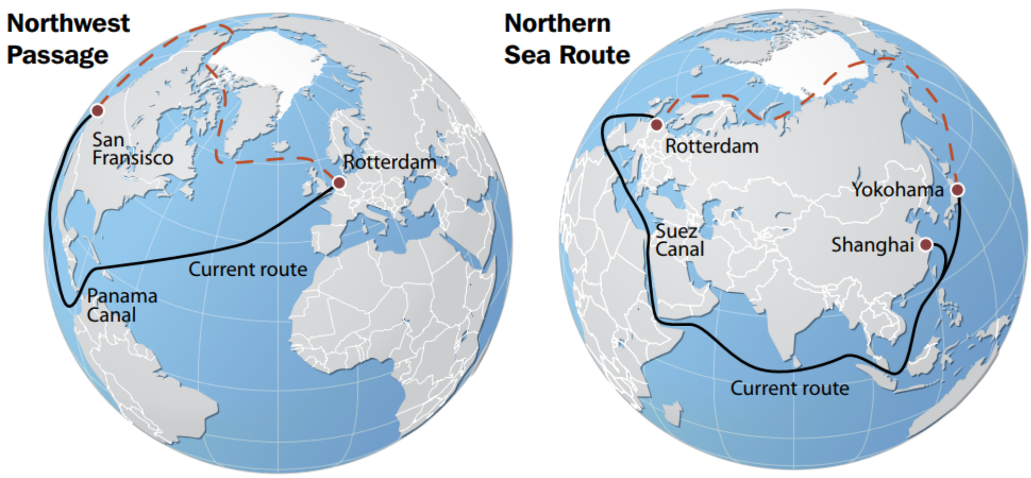

Figure 1-2: Comparison between the Arctic shipping routes (red dashed line) and their current counterparts (black solid line) [2]

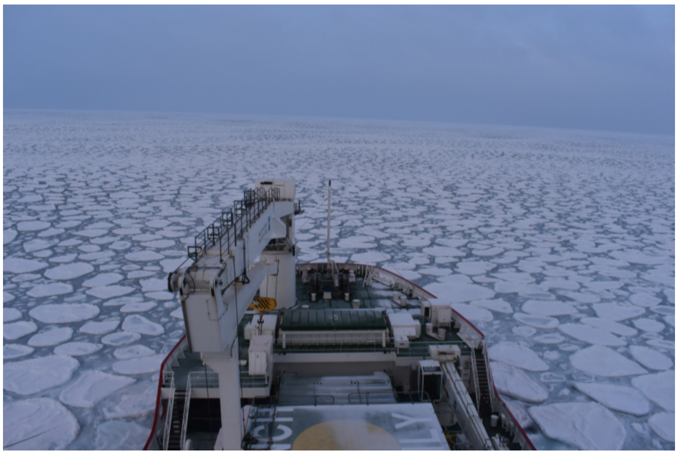

Figure 1-3: A ship surrounded by floating ice floes (Credit: Alessandro Toffoli)

1.2 Problem definition

To clarify the uncertainty brought by floating ice to Arctic shipping and facilitate corresponding hull design, power estimates and route planning, this work aims to develop reliable models that can represent shipping scenarios in the presence of sea ice and investigate the associated changes to ship resistance in open water. There are two primary scenarios for the proposed problem. The first scenario is a cargo ship operating in a waterway infested by floating ice floes, as identified to be the dominant ice condition for the emerging Arctic shipping routes. Moreover, certain segments of the shipping routes can still be seasonally covered by consolidated ice, which are unnavigable for cargo ships and icebreaker assistance would be required in this case. Therefore, the second scenario represents a cargo ship operating in a channel created by icebreakers in continuous ice, a standard solution to maintain the navigability.

Additionally, the ice-floe environment allows ocean surface waves to propagate through it. In such a event, the waves can dictate the ice distribution, and meanwhile the ice can affect the wave propagation. For example, waves can cause large floes to break up into smaller floes, until the floes are sufficiently small to survive intact in the waves [32]; meanwhile, waves attenuate when passing through ice floe fields [33]. Therefore, following wave propagation and attenuation from open ocean to permanent ice sheets, the size of ice floes generally increase [34]. Smaller floes are more susceptible to melting [35] and waves also introduce warm water to further increase the melting rate [36], significant for atmosphere-ice thermal exchange. These processes are currently accounted for in climate models through simple empirical equations that are not satisfactorily accurate [37]. To better model wave-ice interactions is very important for predicting the environmental conditions for Arctic shipping and achieving voyage planning. Thus, this work also intends to build advanced models for the wave-ice interactions that can be useful to understand the Arctic sea states and ice conditions.

1.3 Literature review

1.3.1 Arctic ice and shipping activities

1.3.1.1 Historical observation

Since the late 1970s when satellite observations began, the Arctic ice extent has decreased rapidly, as shown in Figure 1-4. Such reduction is most significant in September, at a rate of -12.9 $\pm$ 1.47% per decade [38], evidenced by an obvious transition from ice-covered areas to open water, as shown in Figure 1-5. The melt of sea ice is actually a process of volume loss, which includes not only the reduction of ice extent but also a decrease of thickness [39]. A combination of submarine and satellite measurements indicates the Arctic sea ice has thinned by more than 50% in the past 50 years [5], as shown in Figure 1-6.

The ice melting has created more complex conditions than level ice coverage and open water. Level ice is also evolving into broken ice floes floating on the sea surface, pronounced as a decrease of ice compactness [40]. Meanwhile, those floes tend to be circular under the effect of wave wash and floe-floe collisions, thus known as pancake ice, as shown in Figure 1-7. Such a status is known as the Marginal Ice Zone (MIZ) [41], as illustrated in Figure 1-8; with the process of global warming, MIZ is taking an increasing proportion in polar regions and is predicted to be a primary environment of future Arctic [14, 42].

The reduction in ice extent, thickness and compactness leads to an increased impetus for Arctic maritime activities. On one hand, the decrease of the ice-covered area opens a larger navigable area and results in that vast quantities of natural resources such as oil, gas and minerals are becoming exploitable; on the other hand, the ice thinning increases the ability of ice-breakers to create paths, thus further improving the accessibility of commercial ships to the Arctic.

There has been a significant growth of complete transits of the NWP and the NSR, especially for the NSR that hosted more than 60 transits in 2019, as shown in Figure 1-9. Nevertheless, this amount is very small compared approximately 1700 transits through the traditional routes [43]. Thus, there is still huge potential for the Arctic shipping routes to share the carrying capacity.

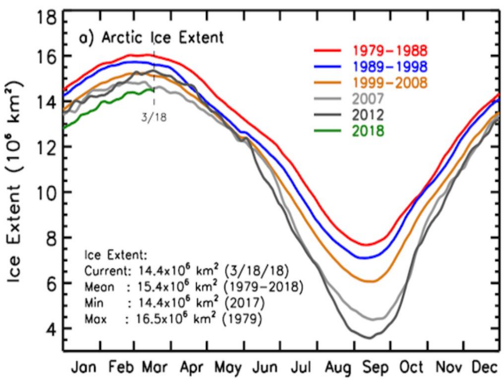

Figure 1-4: Satellite observation of the sea ice extent till the March of 2018 [3]

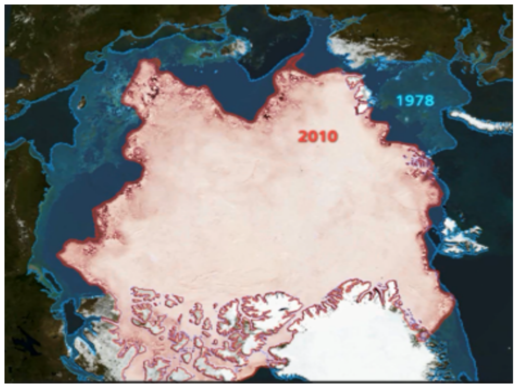

Figure 1-5: Arctic ice extent in September of the year 1978 and 2010 [4]

1.3.1.2 Future prediction

Multiple prediction models have indicated that the retreat of the Arctic ice will not slow down, and it has become a consensus that an almost ice-free Arctic will appear by mid-century [29, 31], as shown in Figure 1-10. This will be accompanied by a stable increase of navigable days per year, which can be seen in Figure 1-11. There seems to be bright promise for LNG carriers to bring Arctic gas to market; oil tankers doing the same with oil; cargo shipping serving Siberian communities; and various specialised ships, for instance, Japanese freezer ships could

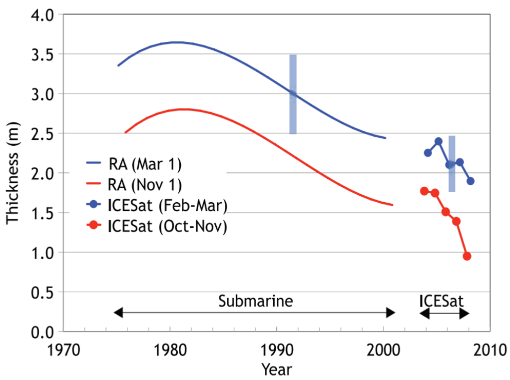

Figure 1-6: The decreasing trend of the Arctic ice thickness [5]

Figure 1-7: Pancake ice condition [6]

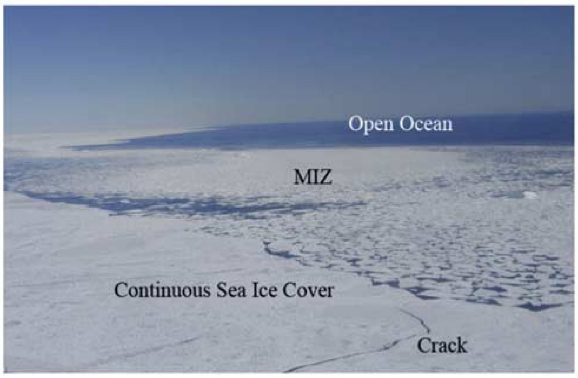

Figure 1-8: A comparison among the Marginal Ice Zone (MIZ), continuous ice cover and open ocean [7]

purchase seafood from US fishermen and deliver it straight to Europe via the NSR [29]. Moreover, the Arctic also contains 13% of the world's undiscovered oil, 30% of the gas and abundant deposits of valuable minerals [44]. With projects commencing such as the Yamal LNG facility, exploration activity will only increase in the next few years [43].

In practice, a navigable Arctic may come earlier than expectations. Existing prediction models have not performed accurately against historical observations, which have shown a larger loss of sea ice than predicted [45]. This suggests that large-scale activities of Arctic shipping may occur even sooner, attracting special research interest and investment from stakeholders.

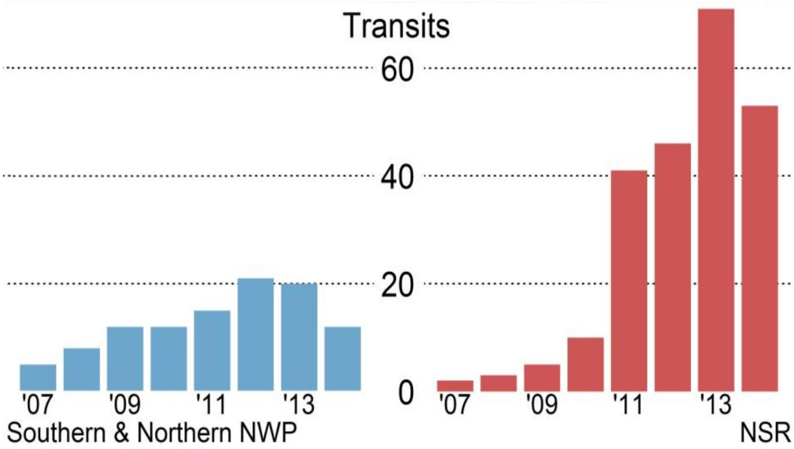

Figure 1-9: The number of transit per year through the Northwest Passage (NWP) and the Northern Sea Route (NSR) [8]

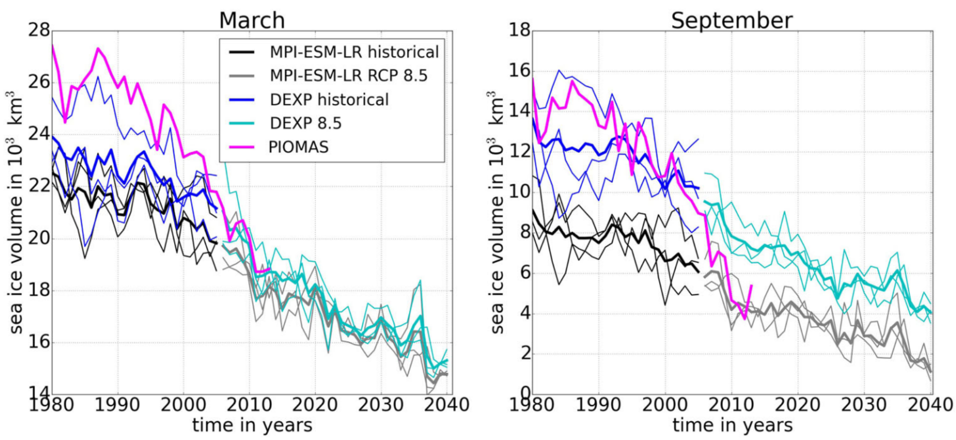

Figure 1-10: The decreasing trend of the Arctic sea ice: historical observations and future predictions [9]

1.3.2 Wave-ice interactions

The changing ice conditions increases new wave-ice dynamics in the Arctic. As shown in Figure 1-8, incoming waves from open ocean can interact with ice floes in the MIZ and then the continuous ice cover. Based on the relative size of ice to waves, relevant research has been broken down into wave interactions with small ice floes and with a large ice sheet, which are reviewed respectively in this section.

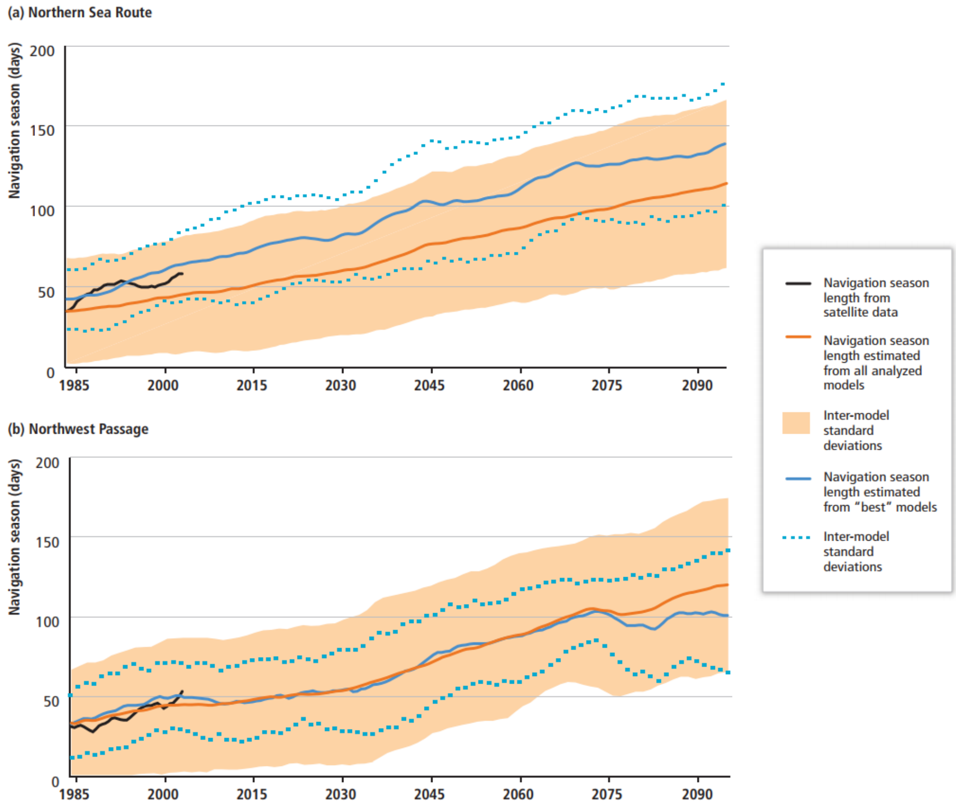

Figure 1-11: Projected duration of the navigable period of the Northern Sea Route and the Northwest Passage [10]

1.3.2.1 Ocean waves with small ice floes

In the MIZ, ocean waves can induce the movement of a solitary ice floe and lead to the distinctive behaviour of multiple ice floes, such as collision [46], herding [47] and rafting [48]. Meanwhile, the incoming waves can be scattered by an ice floe to cause directional spreading thus attenuated by a group of ice floes [33]. Based on the long wavelength and small amplitude waves that are common in the MIZ, previous studies usually consider the ocean waves to compose of regular waves, and the ice floe is assumed to be rigid according to its relatively small dimension.

Meylan et al. [49] conducted wave tank experiments to investigate the wave-induced motions of a solitary floating disk. They recorded the movement trajectory of the disk and decomposed it into six-degrees-of-freedom (6-DOF) motions. Alongside drifting with the wave flow, the disk was found to undergo oscillatory motions at the same frequency as the incident waves. They also observed wave scattering when the dominating wavelength is less than twice of the disk diameter and found the scattering can reduce the motion amplitudes of the disk. However, they used a barrier around the edge of the disk to prevent overwash, i.e. wave running over the top of the disk surface. Based on the findings of Meylan et al. [49], Yiew et al. [19] carried out further experiments to study the influence of overwash on the disk motions, by comparing the motions of two disks, with and without the edge barrier. They found overwash tends to happen with short wavelengths or large wave amplitudes and has a suppression effect on the disk motions.

Considering the prohibitive cost of experimental testing, theoretical models have the potential to provide more efficient and economical solutions. Grotmaack and Meylan [50] applied a slope-sliding model to predict the wave-induced surge motion of an ice floe. The model assumes the floe does not affect the incoming wave field, so it is not applicable in a short-wave condition where scattering is expected to happen. Meylan and Squire [51] and Montiel [52] developed a linear potential-flow/thin-plate model that includes the wave field surrounding the floe due to scattering. It can predict the wave-induced surge, heave and pitch motions of an ice floe; after validation against the experiments of Yiew et al. [19], this model was shown to be accurate for the case without overwash but lack accuracy when notable overwash occurs.

Theoretical models are built upon certain ideal assumptions, by which exact analytical solutions may be obtained but are limited by corresponding applicabilities. For example, they usually assume the nonlinearity, viscosity and turbulence of the fluid are negligible and thus the wave amplitude should be sufficiently small. These assumptions exclude some influential phenomena in wave-ice interactions, e.g. overwash. Although Skene et al. [22] recently incorporated the nonlinear shallow water equations with the linear potential-flow/thin-plate model to predict the depth of the overwash water, their method was only one-way coupling, i.e. no back coupling from overwash to predict the surrounding fluid domain or the ice floe motions. Due to the very small freeboard of sea ice, overwash is a highly frequent phenomenon thus of great importance, while a gap remains on accurately modelling it and studying its role in wave-ice interactions.

A remedy to this can be using the Computational Fluid Dynamics (CFD) technique to numerically solve the nonlinear Navier-Stokes equations, by which it is possible to obtain a fully-coupled solution between the fluid domain and floating-body motions. The wave-ice interaction including overwash can be considered as a combination of two typical CFD applications: (a) wave response of a floating body (b) green water load. For both of topics, related CFD methods have been applied successfully [53], so technically it is possible to build a CFD model to simulate the interaction of waves with a floating ice floe including overwash. Another reason to apply the CFD method is that it would be easy to import complex geometry files to further study the coupling wave-ice effect on a structure, important for Arctic engineering.

CFD has barely been applied to the ice-floe problem. Only one publication has been found, in which Bai et al. [54] used an opensource CFD code, OpenFOAM [55], to predict the wave-induced movement of a solitary ice floe. Their computational results show good agreement with experimental results when overwash occurs, which suggests CFD could be a suitable method. Addtional relevant work needs to be conducted with CFD; for example, Bai et al. [54] modelled the ice floe in square shape rather than the more common pancake shape, and the role of overwash and scattering remains to be analysed. Furthermore, the CFD model of waves with a solitary floe will need to be expanded to incorporate multiple ice floes.

1.3.2.2 Ocean waves with a large ice sheet

Different from the ice-floe scenario discussed above, ice sheets in the Arctic can be kilometres long, having a very small thickness-to-length ratio. In this situation, the wave response of an ice sheet is dominated by the elastic deformations rather than rigid body motions, known as the hydroelasticity of sea ice. A review of this phenomenon has been given by Squire [56], where the author notes its modelling is a key challenge of polar science and engineering. Noting that the Arctic ice sheets are getting increasingly thin [39], the effects of sea ice hydroelasticity are becoming more significant.

Studies on sea ice hydroelasticity have mainly modelled an ice sheet as a thin elastic plate subjected to regular ocean waves. Experimentally, Meylan et al. [57] conducted wave basin tests to measure the wave response of a plastic plate. They found that the plate deforms due to wave propagation. Performing similar experiments, Sree et al. [58] observed that a high aspect-ratio plates tended to follow the wave-shape, and they reported wave attenuation due to the presence of the plate. Sree et al. [20] also found that the wavelength and wave celerity inside the plate are larger than those of an open water situation. Dolatshah et al. [59] conducted real ice tests to study the wave-induced ice vibration and breakup. When encountering an ice sheet, waves partially pass through and are partially reflected, for which Nelli et al. [21] measured the proportion of the transmitted & reflected waves, expressed as transmission & reflection coefficients. With increasing wavelength, waves were found to be transmitted more and reflected less. Their experiments also indicated the reflection coefficient is insensitive to wave amplitude, while the transmission coefficient can be reduced by the energy dissipative "overwash" phenomenon, which is strongly dictated by the incoming wave amplitude. The depths of overwash water at different wave conditions were reported by Skene et al. [22].

Theoretical work started by obtaining the transmission and reflection coefficients of surface waves propagating against a semi-infinite ice sheet. These models were based on linearised theories that can also be applied to Very Large Floating Structures (VLFS) [60]. In this approach, potential flow theory is employed in the fluid domain and the ice sheet is treated as a linear elastic thin plate. Fox and Squire [61] considered the problem of wave transmission & reflection from open water into an ice sheet. The Eigenfunction Expansion Method (EEM) was adopted for the velocity potentials underneath the open water surface and ice sheet, and an iterative conjugate gradient method was used to impose continuity between these two parts. The transmission and reflection coefficients of waves were obtained, alongside their relationship with the incident wavelength, ice thickness and water depth. Other methods were also applied to the same case, e.g. Chung and Fox [62] employed the Wiener-Hopf method; Hermans [63] used the Green's function method. Although the above studies ignored the submergence of the ice sheet, the ice draught was afterwards included by Bennetts et al. [64], William and Squire [65] and William and Porter [66]. Apart from a semi-infinite ice sheet, relevant linear models were also applied to the case of a finite ice sheet. Meylan and Squire investigated the hydroelasticity of a solitary ice sheet [67, 51] and a pair of ice sheets [68]. Wang and Meylan [69] used the Green's function method to solve the fluid domain surrounding an ice sheet and calculated the wave-induced ice deformation by the finite-element method. In addition, Smith and Meylan [70] investigated the influence of ice thickness on wave transmission.

Works based on theoretical models have provided great insights into sea ice hydroelasticity; however, similar to the small ice-floe scenario, theoretical methods could not include overwash in the large ice-sheet case. Although Meylan et al. [57] provided a linear theoretical model that proves valid to predict wave-induced ice flexure even for high-amplitude wave conditions, Toffoli et al. [71] and Nelli et al. [21] demonstrated the theoretical approach cannot accurately predict the transmission and reflection coefficients when significant overwash occurs, which is because of the exclusion of energy dissipation associated with overwash. To obtain more realistic solutions, CFD may be considered as an alternative, but in this case the ice can no longer be assumed as rigid. When the size of an ice sheet is sufficiently large, a structural solution is required to model the ice deformation in waves, and then the influences of ice deformation on the surrounding waves need to be accounted for. In such a situation, a Fluid-Structure Interaction (FSI) approach is required to obtain both structural and fluid solutions and couple them together.

Tukovic et al. [72, 73] developed an FSI code based on OpenFOAM (fsiFoam solver). It employed a partitioned FSI scheme to include the two-way coupling between fluid and structure, where the fluid and solid solutions are solved separately and coupled via the fluid-solid interface. An advantage of this approach is that it employs the Finite-Volume Method for both fluid and solid domains [74]. Most current FSI works involve a combination of solvers, usually with a finite-volume (FV) solver for the fluid flow and a finite-element (FE) solver for the structural analysis, which requires a third code for coupling, data interpolation and simulation management. Thus, the combined FV+FE approach for the fluid and solid domains will tend to increase computational costs and impose limitations on the coupling method. In contrast, the entirely FV approach of Tukovic et al. [73] makes an all-in-one solver under the framework of OpenFOAM. Furthermore, a benefit of its open-source nature is the flexibility to add extended models, e.g. viscoelastic, thermoelastic, and poroelastic solids [75, 76].

One gap of this FSI approach is that it is only applicable to single-phase fluid modelling [77]. In other words, it currently cannot be applied to maritime applications containing both air and water. Therefore, in order to simulate sea ice hydroelasticity, the approach needs to be extended to be capable of modelling multi-phase flows. For this, one potential solution is to expand the approach Tukovic et al. [73] to include the Volume of Fluid (VOF) method [78], a method well validated in modelling ocean free surface.

1.3.3 Ship operation in various ice conditions

This section in order reviews four common scenarios of ship operation in ice conditions:

The Arctic region used to be covered by consolidated ice all year round and was only accessible by icebreakers. The ice coverage mostly has a flat surface, thus referred to as level ice, which is the most classical ice condition for polar ship operation. This is the first scenario to be reviewed - icebreaker in level ice.

To enable commercial, non-icebreaking, ships to navigate through regions covered by level ice, a standard solution is to use icebreakers to create channels. There are two types of ice channels identified for this purpose - brash ice channel and open-water ice channel, which are respectively the second and third scenarios.

Moreover, global warming has induced a widespread transformation of Arctic level ice into broken ice floe fields, presenting shipping routes that are navigable for commercial ships but infested by floating ice floes. This gives the fourth scenario - a commercial ship operating in floating ice floes.

1.3.3.1 Icebreaker in level ice

When an icebreaker is advancing in level ice, the ship-ice contact causes ice crushing and produces broken ice pieces that can slide along the hull and provide friction [79], as shown in Figure 1-12. The icebreaking process induces the majority of the total ship resistance in level ice, alongside a smaller proportion induced by the water underneath the ice [80].

The ship resistance in level ice has been widely studied since it is essential for icebreaker performance. Model tests [81, 82, 11] have reported that the level-ice resistance is dictated by the ice thickness and hull form. Based on experimental and sea-trial data, empirical equations [83, 84, 85] were derived to express the ship resistance as a function of influential hull particulars, ship speed, ice thickness, ice strength and friction.

Modelling methods has also been widely developed for this classical scenario. Hu and Zhou [86] applied a numerical method to predict the level ice resistance, which is more time-consuming than empirical equations but can be incorporated with a realistic hull geometry. They compared the proposed numerical method and previous empirical equations to calculate the resistance of an icebreaker in level ice of a range of thickness and speed. Following validation against model tests, the numerical prediction performs more stably than empirical formulae, with deviations of less than 10% for all the tested conditions, while each of the empirical equations is less accurate in a certain thickness/speed range. Li et al. [87, 88, 89] developed a finite-element-based model for icebreaking vessels and validated the model prediction against full-scale measurements. More modelling work for this case can be found in the review of Xue et al. [90]. Generally speaking, various methods have reported good accuracy in predicting the ice resistance in this scenario.

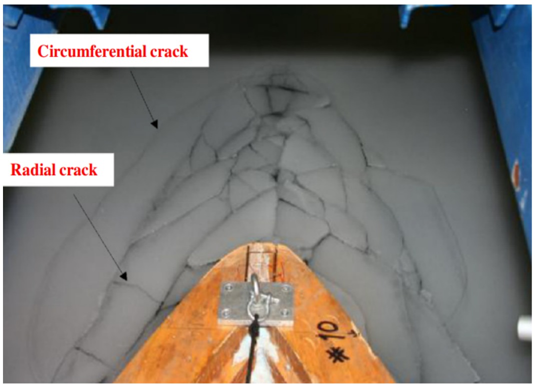

Figure 1-12: Experimental view of an icebreaker advancing in level ice [11]

Figure 1-13: Commercial ships travelling in a brash ice channel [12]

1.3.3.2 Ship in a brash ice channel

Brash ice refers to an accumulation of ice fragments. A brash ice channel, as shown in Figure 1-13, is usually created by an icebreaker in level ice so that commercial ships are able to operate as needed. Kitazawa and Ettema [91] compared model tests of ships operating in brash-ice channels with in open water, which shows that that the ice-added resistance can be several times greater than the water resistance. They also concluded that the brash-ice resistance is almost linearly proportional to the thickness of the brash-ice layer, and the resistance is little affected by the channel width when the channel is wider than twice of the ship beam.

The Finnish Swedish Ice Class Rules (FSICR) [92] provide empirical formulae to predict the resistance of commercial vessels in a brash ice channel, which has been widely used. However, recent model-test work [93] reported that the FSICR formulae overestimate the brash ice resistance, showing there is still space for FSICR to improve the accuracy; for example, the size and shape of ice pieces have not been taken into consideration [94].

On the other hand, numerical models have been developed and appeared to be more comprehensive, typically using the Discrete Element Method (DEM) to model the ice fragments [95, 96]. The DEM simulation of Knono et al. [97] shown good agreement with experiments in predicting the ship resistance in a brash ice channel; Luo et al. [98] also reported good accuracy of DEM in predicting the brish-ice resistance. More examples can be found in the review of Tuhkuri and Polojarvi [96], presenting promising capabilities of DEM in modelling the interactions of a ship/structure with small ice pieces.

1.3.3.3 Ship in an open-water ice channel

Since the resistance increment induced by brash ice is a considerable burden for commercial ships operating in ice channels, new technology has been developed for modern icebreakers to clean the broken ice fragments produced during the ice-breaking process. One such method is turning the azimuth-propulsion units inwards by 15 $\sim$ 30 degrees, called ”toe-in” mode, with which the flushing effect can push the broken ice pieces under the ice sheets, thus cleaning the channel and making it slightly wider. This technique has shown effective for negating the brash ice resistance component, as well as reducing the chance of blockages in the new channel due to freezing of the broken ice pieces [99]. This approach therefore results in an open-water channel between two large ice sheets, as shown in Figure 1-14, an alternative for brash-ice channels that will increase in likelihood. Since the shipping season will remain variable and unreliable in the first half of this century, commercial ships will continue to require ice-breaker escort assistance [8]. Therefore, the importance of studying this scenario is rising.

To date, limited research into ship performance in open-water ice channels has been conducted, with few experimental investigations found in literature. Leiviska et al. [100] conducted model tests of an oil tanker with a range of open-water ice channels of different ice thicknesses and channel widths. In their results, an open-water ice channel was seen to induce a markedly higher resistance than that of a pure open-water situation without any ice, and the resistance increment was found to be influenced by channel width and ship speed. In particular, the resistance increments are evident when the channel width is less than three times of the ship beam. Heinonen [101] reported on model tests for an icebreaker in open-water ice channels and also observed that the close proximity of the ice edge to the ship can increase the resistance. However, both Leiviska et al. [100] and Heinonen [101] did

Figure 1-14: Open water channel created by an icebreaker (Credit: Aker Arctic)

Figure 1-15: Experimental view of a ship advancing in floating paraffin slices [13]

not give collective conclusions and claimed that more studies are required to clarify the underlying mechanism.

There is no modelling work found on the case of open-water ice channel, but a similar and well-studied scenario is the operation of a ship in a canal. Existing studies found that the ship resistance in a canal relates to the wave reflection and flow change induced by the canal walls [102]. However, the ship hydrodynamics discovered in a canal scenario may not be directly applied to open-water ice channels, as there are certain important differences between these two cases. Figure 1-16 provides a schematic comparison of a ship operating in open water, a canal and an open-water ice channel. The proposed problem is different from a canal as the ice has a limited thickness and is floating on the water surface. In addition, the water depth in a canal is usually restricted, thus limiting underkeel clearance, while an ice channel tends to be in deep water. Nevertheless, in term of method, as CFD has been validated in the canal case [103], it could be practical to employ similar numerical theories while applying the ice-channel geometry to confine the ship flow.

1.3.3.4 Ship in floating ice floes

Satellite and field observations in recent years have reported very different Arctic ice conditions from the traditional level ice. During the navigable summer season, numerous floating ice floes are observed along the emerging Arctic shipping routes, usually in pancake shape. Figure 1-17 demonstrates the dominance of the

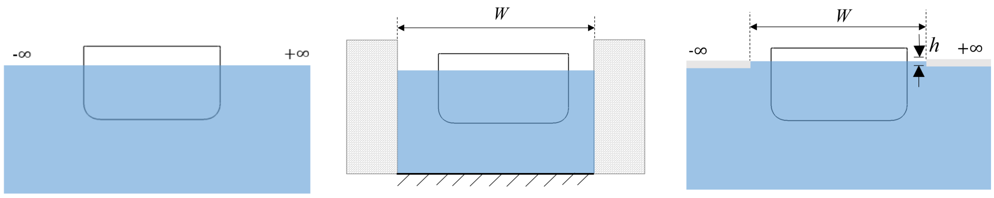

(a) Open ocean (b) Canal (c) Ice channel

Figure 1-16: Comparison of ship operating in three different scenarios: open ocean, canal and open-water ice channel; W is the width of the channel and h is the ice thickness

ice-floe condition (green and blue) along the measured routes, reported by field observations in the autumn of 2015, while level ice (red) only occupies a small portion. The emerging ice-floe conditions are navigable for commercial ships without icebreaking capabilities, despite requiring icebreaker assistance when encountering level ice. Thomson et al. [14] predicted that the proportion of pancake ice will keep increasing with the climate change effect and become the dominant ice condition of future Arctic shipping.

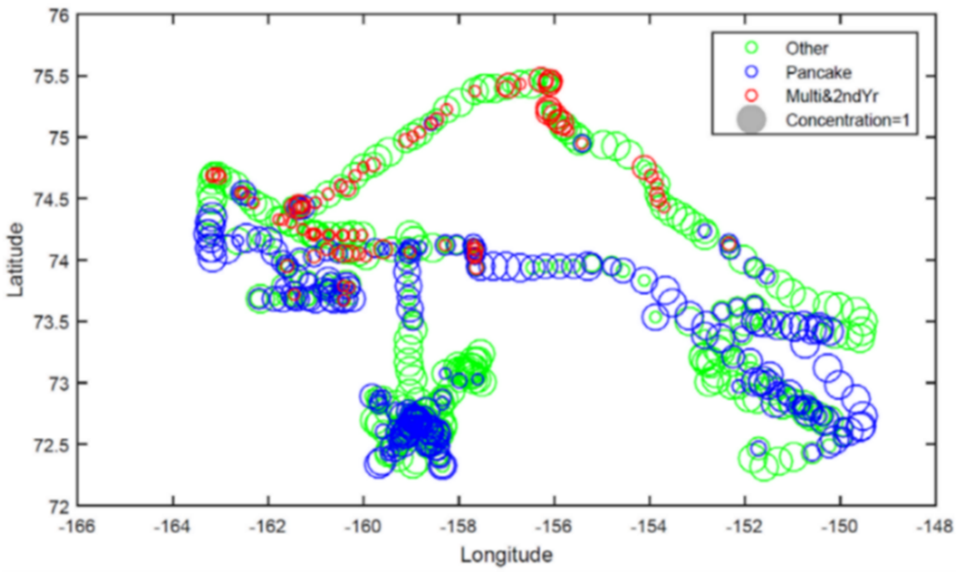

Figure 1-17: Ice conditions along shipping routes of Western Arctic, measured in Autumn 2015 [14]

As an emerging scenario, the study of ship performance in ice floes has only started in recent years. Guo et al. [23] measured the resistance of an advancing ship in a towing tank with numerous pieces of floating paraffin wax, mimicking ice floes, as shown in Figure 1-15. They reported that such floating floes can induce significant resistance increments on the ship, indicating the importance of accurately predicting the ice resistance. Subsequently, Luo et al. [13] conducted similar experiments but in head sea conditions to assess the seakeeping performance of a ship surrounded by floes. They reported the presence of floes can increase the heave and pitch response of a ship.

Considering the complexity of such experiments and the shortage of field-measurement data, developing a reliable computational model can be a cost-effective way to provide insights into the ship performance in floating ice floes. Successful modelling of broken ice-floe fields has been achieved using the Discrete Element Method (DEM), since this method allows the calculation of the contact force of ice-ice and ice-structure, which is essential for modelling ship operation in ice floes.

Currently, one gap in related DEM simulations is how to accurately account for the force of the surrounding fluid on ice, which is usually implemented by empirical equations [96]. Due to this deficiency, previous simulations of a ship advancing in ice floes ignored the effect of fluid flow [104, 105, 106, 26], which can make the modelling insufficiently realistic. The process of a ship advancing in floating ice floes can be summarised as the following ship-wave-ice interaction: ship advancement generates waves; waves interact with ice floes; ice floes make contacts with each other and with the ship. The ship-generated waves can play a key role within the process; for example, it can change the velocity (magnitude and direction) of floes, especially when the floes are small. Therefore, ignoring the wave effect may considerably influence the ice load on a ship.

One solution could be using CFD to provide fluid forces for DEM ice floes, since CFD has proved to be a mature method to obtain the wave generated by an advancing ship [107], as well as accurate in predicting the motions of ice floe in waves [54]. Other potential approaches could be combining the Lattice Boltzmann method (LBM) [108] or the Smooth Particle Hydrodynamics (SPH) [109] with structural solutions to model the ship-wave-ice interaction, but the applications and validation of SPH and LBM in ocean engineering are still rare when compared with CFD. One disadvantage of CFD comparing with empirical/theoretical predictions is that it needs much higher computational power. However, as DEM requests very high computational power itself, compared with using DEM solitarily, using CFD to provide fluid solutions for DEM will not significantly increase the required computational cost. Based on the above reasons, it is recommended to combine CFD with DEM to achieve the ship-wave-ice coupling.

Another challenge in the modelling of ice-floe fields is how to import natural ice distributions into computational models. In polar regions, ice floes are randomly distributed and of a range of sizes [110]. Even though computational models are capable of simulating the structure-wave-ice interaction, the initial size and location of each floe need to be prescribed. For example, in the computational models of Janssen et al. [108] amd Sun and Shen [15], ice floes are set to have a uniform size and a uniform initial distance between each other, as shown in Figure 1-18; this is not a natural condition and the result can be subjected to the initial setup, e.g. the relative positions between ship and floes can considerably influence the ice load. Therefore, there is the need to import natural ice distributions to realistically simulate the physical processes associated with Arctic ice-floe fields.

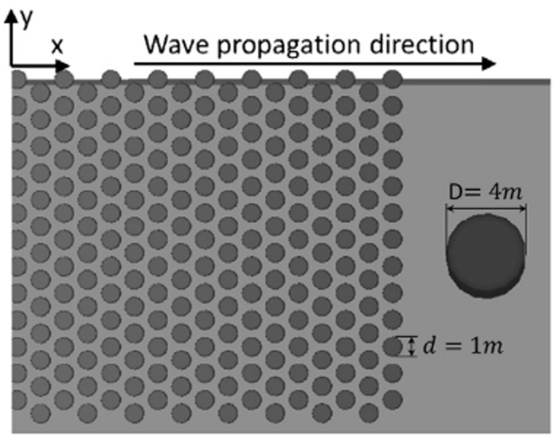

Figure 1-18: Regular pancake-ice field used by Sun and Shen [15]

1.4 Research gaps

Following the literature review, there are clear gaps in the modelling of potential wave-ice interactions and shipping scenarios in the Arctic.

For wave-ice interactions, analytical methods have been used as the standard in previous studies, but their ideal assumptions have been found to induce inaccuracies due to the exclusion of some nonlinear features, especially the overwash behaviour. The CFD method, with the potential to remedy this issue, has however barely been applied in this field. In addition, a new hydroelastic method is required to model the interaction of waves with large ice sheets, as the wave-induced ice deformation needs to be accounted for.

For ship operations in various ice conditions, numerous studies have been conducted for traditional level-ice and brash-ice-channel scenarios, with corresponding modelling methods well established. Yet there has been a lack of work investigating the scenarios of ship operations in an open-water ice channel and in floating ice floes. Both these scenarios appeared in recent years and so far there is no valid modelling approach for either of them.

1.5 Research vision

Based on the identified research gaps, this work aims to develop valid computational models to simulate four specific cases and perform systematic simulations to investigate them: (I) the interaction of ocean waves with a rigid ice floe; (II) the interaction of ocean waves with an elastic ice sheet; (III) the operation of a cargo ship in an open-water ice channel; (IV) the operation of a cargo ship in floating ice floes.

Cases (I) and (II) aim to provide a set of modelling methods for polar wave-ice interactions, which can cover the scenarios where sea ice needs to be modelled as either rigid or elastic, depending on its characteristics. Case (III) and (IV) are primary ice conditions that a commercial ship can encounter in an ice-infested Arctic sea route; specifically, an open-water vessel is able to operate by itself in ice floe fields, while consolidated ice can exist in certain segments of its route, in which case icebreaker assistance would be required and the ship would be operating in an ice channel. Therefore, Case (III) and (IV) can combine into a modelling strategy for the design and power estimates of a typical ice-going commercial vessel.

1.6 Research approach

To meet the vision of this work, valid modelling approaches are required to be established for the four identified cases. Based on the literature review, it is proposed to use CFD as the foundational technique for all of the four cases, since CFD has revealed a superior capability in the modelling of ship and wave hydrodynamics, which is essential in the identified cases. Additionally, since the research cases are interactive problems between ship, wave, and sea ice, as illustrated in Figure 1-19, CFD is required to be coupled with various solid solutions of sea ice, specifically, in Case (I) with rigid ice motions, in Case (II) with elastic ice deformations, in Case (III) with the restriction of ice sheets, and in Case (IV) with the collisions of ice floes with each other and with a ship. It is found that rigid ice motions may be modelled by the six-degree-of-freedom equations; elastic ice deformations may be modelled by computational solid mechanics; the restriction of ice sheets may be modelled using the wall boundary condition validated in a similar canal case; and ice-floe collisions may be modelled by the discrete element method. In particular, it is crucial to apply/develop appropriate coupling algorithms between CFD and these solid solutions.

The work will start with the cases of wave-ice interactions and then move on to the ship-wave-ice interactions, since the investigations for Cases (I) and (II) are expected to provide constructive insights into modelling the ice sheets and floes in Cases (III) and (IV).

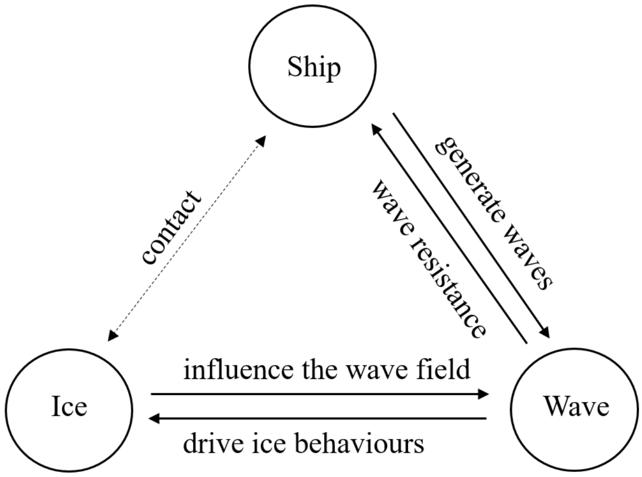

Figure 1-19: Illustration of ship-wave-ice interactions as broken down into subprocesses

1.7 Research questions

Regarding wave-ice interactions:

- What is the valid simulation approach to model the interaction of ocean waves with a small ice floe?
- What is the valid simulation approach to model the interaction of ocean waves with a large ice sheet? This approach should account for the wave-induced ice deformation.
- What are the interactive behaviours between ocean regular waves and a floating ice floe/sheet? This is a two fold problem, including the response of the ice in waves, as well as the influence of the ice presence on the wave propagation. Also, how do the interactions change with the relative wave-ice dimensions? What is the influence of overwash on the wave-ice interactions?

Regarding ship-wave-ice interactions:

- What is the valid simulation approach to model the operation of a ship in an open-water ice channel?

- When a ship is operating in an open-water ice channel, how does the resistance change compared with a pure open-water condition and what is the underlying reason? How is the ice-induced resistance change affected by relevant environmental/operational variables, e.g. ship speed, ice thickness and channel width?

- What is the valid simulation approach to model the operation of a ship in a waterway with floating ice floes?

- When a ship is operating in floating ice floes, how does the resistance change compared with a pure open-water condition and what is the underlying reason? How is the ice-induced resistance change affected by relevant environmental/operational variables, e.g. ship speed, ice thickness, ice concentration and floe diameter?

1.8 Thesis outline

Following this introduction chapter, Chapter 2 will introduce the numerical theories to be employed in the remaining chapters. Chapter 3, 4, 5 and 6 will in turn report work on each of four cases, which includes practicalities on building the computational model, the model's verification and validation, systematic simulations with respect to influential variables, and analyses into the phenomena. Chapter 7 will develop an approach to incorporate the results from relatively slow computational simulations into applications that require rapid computing, e.g. a real-time Arctic voyage planning tool. Chapter 8 will summarise the project and discuss its implications and limitations, and then provide suggestions for future work.

Chapter 2

Numerical methods

This chapter presents the numerical theories applied in this project and their principal equations. In the first part, CFD solutions for fluid flows is introduced, e.g. the pressure and velocity fields in a computational domain. Particularly, the fluid solutions include the methods for modelling free surface and ocean waves, since these are involved in this project. The second part of this chapter presents the solid solutions for modelling ice rigid motions, ice elastic deformations and ship-ice/ice-ice collisions. These solid solutions are incorporable with CFD solutions to model relevant interactions. The final part introduces the computational procedure to yield the solutions.

2.1 Fluid solutions

2.1.1 Navier-Stokes equations

Based on the continuity of mass and momentum, the velocity and pressure of a fluid domain can be solved using the Navier-Stokes equations for incompressible, isothermal and Newtonian flow, as expressed in Equation 2.1 and 2.2.

$$\nabla \cdot \mathbf{v} = 0 \tag{2.1}$$

$$\frac{\partial(\rho \mathbf{v})}{\partial t} + \nabla \cdot (\rho \mathbf{v}\mathbf{v}) = -\nabla p + \nabla \cdot \tau + \rho g \tag{2.2}$$

where $\mathbf{v}$ is velocity vector, p is pressure, ρ is the density, $\tau = \mu\left(\nabla\mathbf{v} + \nabla\mathbf{v}^T\right)$ is the viscous stress, μ is the dynamic viscosity and g is gravitational acceleration.

2.1.2 Turbulence modelling

Ship operations and wave-structure interactions can induce turbulent fluid behaviours. The turbulent flow contains unsteady vortices, which leads to fluctuating changes of pressure/velocity and certain dissipation of kinetic energy. Thus it is of great importance to account for the turbulent effects in computational modelling so as to secure accuracies. One approach for modelling the turbulent effects is to extend the Navier-Stokes equations into the Reynolds-Average Navier-Stokes equations (RANS) where instantaneous turbulent velocity is decomposed into its time-averaged and fluctuating components, as expressed in Equation 2.3 and 2.4.

$$\nabla \cdot \overline{\mathbf{v}} = 0 \tag{2.3}$$

$$\frac{\partial(\rho\overline{\mathbf{v}})}{\partial t} + \nabla \cdot (\rho\overline{\mathbf{v}}\overline{\mathbf{v}}) = -\nabla\overline{p} + \nabla \cdot (\overline{\tau} - \rho\overline{\mathbf{v}'\mathbf{v}'}) + \rho g \tag{2.4}$$

where $\overline{\mathbf{v}}$ is the time-average velocity, $\mathbf{v}^{'}$ is the fluctuating component. Since the fluctuating one has increased the number of unknowns, an extra turbulence model is required to close the equations. For ocean engineering simulations that have a similar scale as the proposed cases in this project, the most common turbulence models are the $k-\varepsilon$ family and the $k-\omega$ family, both have a number of branches specialising in different problems [111].

The solution to close the equations is given below using the standard $k-\varepsilon$ model as an example, since other $k-\varepsilon$ and $k-\omega$ variants are similar. It can be seen in Equation 2.4 that the RANS equations introduced an additional term $\rho\overline{\mathbf{v}'\mathbf{v}'}$. This additional term can be expressed through the Boussinesq hypothesis:

$$-\rho\overline{\mathbf{v}'\mathbf{v}'} = \mu_t(\nabla\overline{\mathbf{v}} + \nabla\overline{\mathbf{v}}^T) - \frac{2}{3}\rho k\mathbf{I} \tag{2.5}$$

where μ_t is the eddy viscosity. The way the $k-\varepsilon$ model works is by expressing μ_t as the turbulent kinetic energy (k) and the rate of dissipation of turbulent kinetic energy (ε):

$$\mu_t = C_\mu \frac{\rho k^2}{\varepsilon} \tag{2.6}$$

Then, k and ε can be solved through their transport equations:

$$\frac{\partial(\rho k)}{\partial t} + \nabla \cdot (\rho \overline{\mathbf{v}} k) = \nabla \cdot [(\mu + \frac{\mu_t}{\tau_k})\nabla k] + P_k + P_b - \rho\varepsilon \tag{2.7}$$

$$\frac{\partial(\rho \varepsilon)}{\partial t} + \nabla \cdot (\rho \overline{\mathbf{v}} \varepsilon) = \nabla \cdot [(\mu + \frac{\mu_t}{\tau_\varepsilon})\nabla \varepsilon] + C_1 \frac{\varepsilon}{k}(P_k + P_b) - C_2 \rho \frac{\varepsilon^2}{k} \tag{2.8}$$

where P_k is the production of mean velocity shear, P_b is the production of buoyancy; $C_\mu = 0.09$, $\tau_k = 1.0$, $\tau_\varepsilon = 1.3$, $C_1 = 1.44$ and $C_2 = 1.92$ are empirical values [112].

2.1.3 Free surface modelling

Since ocean-related problems involve both water and air, there is a need to split the fluid domain into two phases and capture the free surface in between. For this purpose, the Volume of Fluid (VOF) method [78] is applied. The VOF method introduces a passive scalar α, denoting the fractional volume of a cell occupied by a specific phase. In this case, a value of $\alpha = 1$ corresponds to a cell full of water and a value of α = 0 indicates a cell full of air. The local density and viscosity of each cell is determined according to Equation 2.9 and 2.10, and a linear approximation is applied to satisfy the continuity of the free surface, as expressed in Equation 2.11 [113]. Furthermore, the evolution of free surface with time is solved by the advective equation of α, as expressed in Equation 2.12 [114].

$$\rho = \alpha \rho_{water} + (1-\alpha)\rho_{air} \tag{2.9}$$

$$\mu = \alpha \mu_{water} + (1-\alpha)\mu_{air} \tag{2.10}$$

$$\overline{\mathbf{v}} = \alpha \overline{\mathbf{v}}_{water} + (1-\alpha)\overline{\mathbf{v}}_{air} \tag{2.11}$$

$$\frac{\partial \alpha}{\partial t} + \nabla \cdot (\overline{\mathbf{v}}\alpha) + \nabla \cdot [\overline{\mathbf{v}_r}\alpha(1-\alpha)] = 0 \tag{2.12}$$

where $\overline{\mathbf{v}}_{water}$ and $\overline{\mathbf{v}}_{air}$ are the velocities of the nearest water cell and air cell respectively and $\overline{\mathbf{v}_r} = \overline{\mathbf{v}}_{water} - \overline{\mathbf{v}}_{air}$ is the relative velocity between them [115]. In this study, $\rho_{water} = 998.8kg/m^3, \mu_{water} = 8.90 \times 10^{-4} N \cdot s/m^2; \rho_{air} = 1kg/m^3, \mu_{air} = 1.48 \times 10^{-5} N \cdot s/m^2$ and g is set as 9.81 m/s^2.

The free surface between air and water is constructed through all cells with $0 < \alpha < 1$, as illustrated in Figure 2-1.

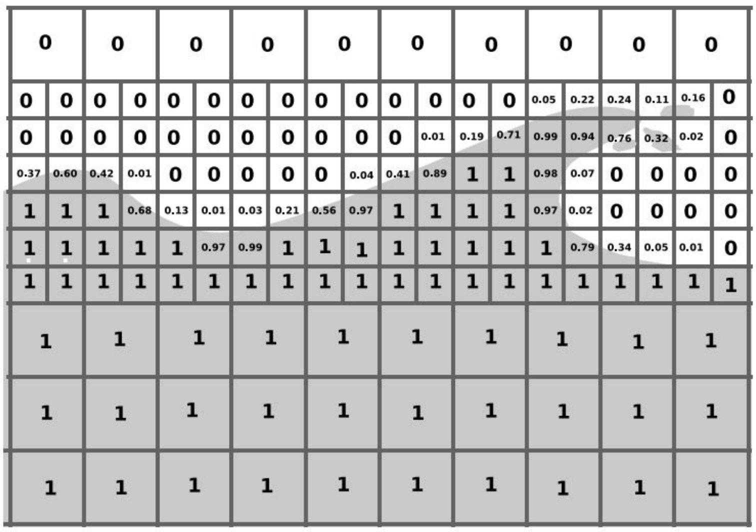

Figure 2-1: Illustration of free surface construction and the corresponding α values [16]

2.1.4 Wave modelling

The modelling of waves includes generation of desired waves at the inlet boundary and a wave absorption in front of the outlet boundary to avoid waves being reflected back and interfering the desirable wave field. For the Arctic wave-ice interactions investigated in this project, the incident waves are commonly of a large wavelength and a small wave height, which may be modelled as regular waves [57, 21]. By prescribing the fluid solutions in the upstream, regular waves can be generated and propagate towards the downstream, according to the linear Stokes wave theory [116]:

$$\eta = d + \frac{H}{2}\cos(kx - \omega t) \tag{2.13}$$

$$v_i = \frac{\pi H}{\delta}\frac{\cosh k(\zeta + d)}{\sinh kd}\cos(kx - \omega t) \tag{2.14}$$

$$v_j = \frac{\pi H}{\delta}\frac{\sinh k(\zeta + d)}{\sinh kd}\sin(kx - \omega t) \tag{2.15}$$

in which, η is the free surface elevation, v_i and v_j are respectively velocity components that parallel and perpendicular to the propagation direction, H is the wave height (double of the wave amplitude a), δ is the wave period, k is the wave number, d is the still water depth, ζ is the vertical location relative to the still water level and ω is the angular frequency. In the computational models of this work, H and δ are given in advance, and the wavelength ($\lambda = 2\pi/k$) is solved by the dispersion relation: $k \tanh kh = \kappa, \kappa = \omega^2/g$.

Inside the wave absorption zone, waves are dissipated by an artificial damping force so that a still water surface can be achieved [117]. Specifically, in the wave absorption zone the momentum Equation 2.4 is modified into:

$$\frac{\partial(\rho\overline{\mathbf{v}})}{\partial t} + \nabla\cdot(\rho\overline{\mathbf{v}}\overline{\mathbf{v}}) = -\nabla\overline{p} - \nabla\cdot(\overline{\tau} - \rho\overline{\mathbf{v}'\mathbf{v}'}) + \rho g - \rho\chi(\overline{\mathbf{v}} - \overline{\mathbf{v_{str}}}) \tag{2.16}$$

The last term is the artificial damping force that dissipates the wave motion, where χ is the damping coefficient in units of s^{-1}, and it increases smoothly in the wave propagation direction. $\overline{\mathbf{v_{str}}}$ is the background stream velocity that is exempted from damping, which equals zero when there is no current.

2.2 Solid solutions

2.2.1 Rigid-body motion

With the fluid solutions, the fluid force ($\mathbf{F_h}$) on a solid body can be calculated by integrating the solutions on the solid surface, as expressed in Equation 2.17. If the solid body is not fixed, the fluid force can induce its movement, known as rigid-body motions. The motions can be decomposed into six-degrees-of-freedom (6-DOF), as a combination of translation and rotation. This can be solved using the translational and rotational equations based on the mass centre of the structure (G), as expressed in Equation 2.18 and 2.19.

$$\mathbf{F_h} = \int (-\overline{P}\mathbf{n} + \overline{\tau} \cdot \mathbf{n}) dS \tag{2.17}$$

$$\mathbf{F} = m \frac{\mathrm{d}\overrightarrow{V_G}}{\mathrm{d}t} \tag{2.18}$$

$$\Omega = [J] \cdot \frac{\mathrm{d}\overrightarrow{\omega_G}}{\mathrm{d}t} + \overrightarrow{\omega_G} \times ([J] \cdot \overrightarrow{\omega_G}) \tag{2.19}$$

where $\mathbf{F}$ and Ω are the total force and torque on the structure, induced by its gravity and the fluid force; m and $[J]$ are the mass and inertia moment tensor, and $\overrightarrow{V_G}$ and $\overrightarrow{\omega_G}$ are respectively the translational and rotational velocity vectors of the floating structure.

2.2.2 Elastic deformation

When the elastic response of a solid body is evident, the deformation on the solid shape needs to be taken into consideration. To model a deformable solid body, the solid body can also be descretised into a set of cells, and the solid deformation can be described by integrating the displacements of all the cells, known as Computational Solid Mechancis (CSM). The displacement may be solved according to conservation of momentum. In order to account for nonlinear ice deformations, this work applies the nonlinear St. Venant Kirchhoff hyperelastic law to solve the stress inside a solid body, as implemented by Tukovic et al. [118] and Cardiff et al. [76]. The mathematical model in total Lagrangian form (reference configuration) may be written as:

$$\oint_{V_0} \rho_{solid} \frac{\partial}{\partial t}(\frac{\partial \mathbf{u}}{\partial t})\, dV = \oint_{S_0} \mathbf{n} \cdot (\Sigma \cdot \Gamma^T)\, dS + \oint_{V_0} \rho_{solid} g\, dV \tag{2.20}$$

where $\mathbf{u}$ is the displacement vector, $\Gamma = \mathbf{I} + (\nabla u)^T$ is the deformation gradient tensor, and $\mathbf{I}$ is the second-order identity tensor and Σ is the second Piola-Kirchhoff stress tensor, which is related to the Cauchy stress tensor σ through Equation 2.21. The Cauchy stress may be obtained based on the fluid force ($\mathbf{F_h} = \mathbf{n} \cdot \sigma$), and the stress-strain relationship is dictated by Equation 2.22.

$$\sigma = \frac{1}{\det \Gamma} \Gamma \cdot \varepsilon \cdot \Gamma^T \tag{2.21}$$

$$\varepsilon = 2G\Upsilon + \Lambda \mathrm{Tr}(\Upsilon)\mathbf{I} \tag{2.22}$$

where the Green-Lagrange strain tensor Υ is defined in Equation 2.23, and G and Λ are the Lamés coefficients, related to the material properties of Young's modulus E and Poisson's ratio ν, following Equation 2.24 and 2.25.

$$\Psi = \frac{1}{2}[\nabla \mathbf{u} + (\nabla \mathbf{u})^T + \nabla \mathbf{u} \cdot (\nabla \mathbf{u})^T] \tag{2.23}$$

$$G = \frac{E}{2(1+\nu)} \tag{2.24}$$

$$\Lambda = \frac{\nu E}{(1+\nu)(1-2\nu)} \tag{2.25}$$

2.2.3 Collisions

The Discrete Element Method (DEM) is suitable for modelling floating ice floes that tend to have collisional behaviour. In DEM, ice floes are modelled as elements in the Lagrangian framework and they are allowed to move in the Eulerian CFD domain. The movement of each element is governed by the rigid-body-motion equations (Equation 2.18 and 2.19). However, the total force on an element here also includes a solid-solid contact force, $\mathbf{F_c}$, i.e. $\mathbf{F} = mg + \mathbf{F_h} + \mathbf{F_c}$.

The contact force $\mathbf{F_c}$ is calculated by a penalty method [95], in which two colliding solid bodies are allowed to have a small overlap, according to the motion solutions over a timestep. Where a contact occurs, the overlap is modelled as a linear spring-dashpot system where the spring (K) accounts for the elastic response and the dashpot (b) reflects the energy dissipation during the contact, by which the normal and tangential components of $\mathbf{F_c}$ are calculated according to Equation 2.26 and 2.27 respectively. Subsequently, the contact force pushes the overlapped bodies apart so that the overlap is minimised in the solution of the current timestep.

$$\mathbf{F_n} = -Kd_n - bv_n{}' \tag{2.26}$$

$$\mathbf{F_t} = \begin{cases} -Kd_t - bv_t{}', & \text{if } \mid d_t \mid < \mid d_n \mid C_f \\ \mid Kd_n \mid C_f \cdot \mathbf{n}, & \text{if } \mid d_t \mid \geq \mid d_n \mid C_f \end{cases} \tag{2.27}$$

where d_n and d_t are overlap distances in the normal and tangential directions respectively, $v_{n,r}$ and $v_{t,r}$ are the normal and tangential components of the relative velocity between the two contact bodies, C_f is the friction coefficient. In this study, C_f is set at 0.35 for ice-ice contact and 0.05 for ship-ice contact; K is set at $6 \times 10^4 N/m$ and $b = 2C_{damp}\sqrt{KM_{eq}}$, in which C_{damp} is set at 0.067 and M_{eq} is the equivalent mass of two contact bodies, calculated as $M_{eq} = M_A M_B/(M_A + M_B)$. These parameter values are selected based on corresponding tests and guidelines [119, 120].

2.3 Computational procedure

2.3.1 Time discretisation

To obtain the computational solutions, within a certain computational domain and over a certain time duration, the procedure in this work involves two types of discretisation, in space and time respectively. In space, the computational domain is divided into a set of non-overlapping cells, known as a mesh; in time, the temporal dimension is split into a finite number of timesteps; the interval between two adjacent timesteps is known as the timestep size (Δt). For a single timestep, the solution of all the cells can be obtained integrally by solving assigned governing equations. Then, the solution over a certain time duration is the connection of the solution at each timestep.

The temporal discretisation is easier than spatial; in this study, it is realised through the first-order temporal discretisation scheme that approximates a designated transient parameter (denoted as u) using the solution at the current timestep and the one from the previous timestep:

$$\frac{\mathrm{d}(\rho u \mathbf{v})}{\mathrm{d}t} = \frac{(\rho u \mathbf{v})^{t=n+1} - (\rho u \mathbf{v})^{t=n}}{\Delta t} \tag{2.28}$$

The second-order temporal discretisation scheme, which uses the solution at the current timestep and two previous timesteps, is also tested for this study. Nonetheless, the results do not show a notable difference from those yielded through the first-order temporal discretisation.

2.3.2 Spatial discretisation

The spatial discretisation of this work is realised through the Finite Volume Method (FVM) [121]. To solve the governing equations over numerous cells, the procedure can be explained through the example of two neighbouring cells, marked as the owner cell and the neighbour cell as in Figure 2-2. The required solution includes desired variables at the centroid of each cell, as well as the face flux between the cells.

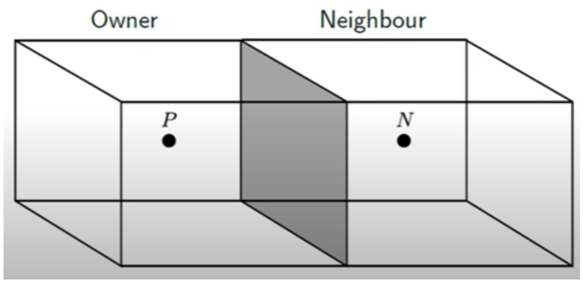

Figure 2-2: Illustration of two neighbouring cells in FVM [17]

Considering the owner cell P, the Navier Stokes equations in the spatial domain can be integrated into the following form:

$$\oint_V [\nabla \cdot (\mathbf{vv}) + \frac{1}{\rho}\nabla P - \nabla \cdot \tau - g] dV = 0 \tag{2.29}$$

Then, each term can be integrated separately:

$$\oint_V [\nabla \cdot (\mathbf{vv})] dV = \oint_V [-\frac{1}{\rho}\nabla P] dV + \oint_V [\nabla \cdot \tau] dV + \oint_V [g] dV \tag{2.30}$$

The integration of a vector term is solved through the Gauss' Divergence Theorem, as given in Equation 2.31 and Figure 2-3, in which **F** denotes an arbitrary vector.

$$\oint_V [\nabla \cdot \mathbf{F}] dV = \oint_S [\mathbf{F} \cdot \hat{\mathbf{n}}] dS \tag{2.31}$$

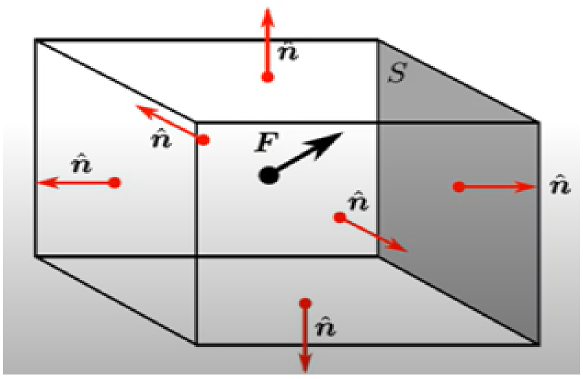

Figure 2-3: Illustration of the Gauss' Divergence Theorem [17]

The above process calculates the solutions at each cell centroid, but to obtain the face flux between cells, the solutions obtained at cell centroids need to be interpolated to the cell surfaces. In this study, the second-order upwind differentiation is used to interpolate the results.

The first and second order upwind schemes are both introduced below for comparison. The first-order upwind scheme determines the transported quantity of a face depending on flow direction and only one neighbouring cell on each side, as shown in Figure 2-4. The second-order upwind scheme determines the transported quantity of a face depending on flow direction and two neighbouring cells on each side, as shown in Figure 2-5.

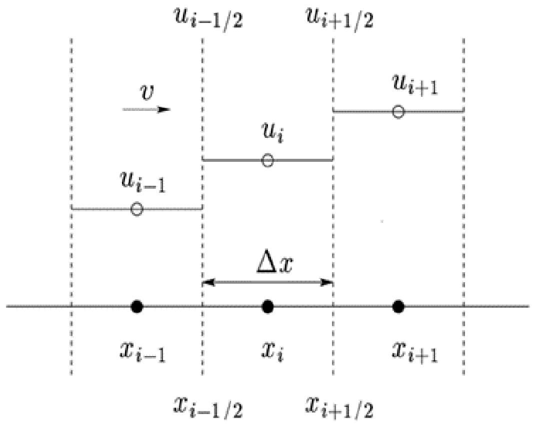

Figure 2-4: Illustration of the first-order upwind scheme [18]: if $v > 0$, $u_{i-1/2} = u_{i-1}$, $u_{i+1/2} = u_i$; if $v < 0$, $u_{i-1/2} = u_i$, $u_{i+1/2} = u_{i+1}$

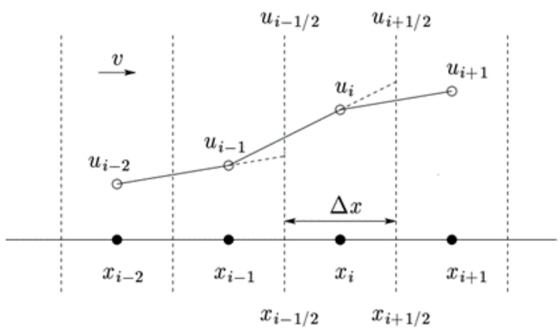

Figure 2-5: Illustration of the second-order upwind scheme [18]: if $v > 0$, $u_{i-1/2} = (3u_{i-1} - u_{i-2})/2$, $u_{i+1/2} = (3u_i - u_{i-1})/2$; if $v < 0$, $u_{i-1/2} = (3u_i - u_{i+1})/2$, $u_{i+1/2} = (3u_{i+1} - u_{i+2})/2$

Both first and second order upwind schemes are tested for this study, showing that the first-order one causes significant inaccuracies. Therefore, it is necessary to use the second-order spatial interpolation.

2.3.3 Pressure-velocity coupling

Directly solving the Navier Stokes equations is currently one of the most challenging mathematical problems. However, the pressure and velocity solutions can be obtained through numerical algorithms. In this study, the PISO algorithm is applied [122]. The algorithm can be summed up as follows:

- According to the initial boundary conditions (for the first timestep) or the solution from the previous timestep (for an intermediate or final timestep), the discretised momentum equation is solved to compute a velocity field, noting that this velocity field does not satisfy the continuity equation.

- This velocity field is used to calculate a pressure field, but this pressure requires correction as it is from a velocity field that does not satisfy the continuity equation.

- Then this pressure field is substituted into the continuous equation to get a new velocity field, which is now satisfying the continuity equation.

- The updated velocity field that satisfies the continuity equation is used to correct the pressure field.

- The corrected pressure field is substituted into the continuous equation to get the final velocity field of the current timestep.

2.3.4 Choice of software

In this project, there were a total of three software packages used for the different cases, i.e. Flow-3D, OpenFOAM, STAR-CCM+. It should be noted that, all three packages have identical CFD solutions, but the choice was made based upon which software provided the best possibility to couple the additional ice solid solution required for each case. Specifically, OpenFOAM gives the required flexibility to fully achieve CFD+CSM coupling, and STAR-CCM+ has a robust DEM package that can be coupled with CFD.

Chapter 3

Wave interaction with a rigid ice floe

A floating ice floe can move with incoming ocean waves and meanwhile affect the wave pattern. In this chapter, a computational model is built to simulate the interaction of regular waves with a circular ice floe, as illustrated in Figure 3-1. A series of simulations are presented to categorise the motions of the floe in different wavelength and wave amplitude conditions, and the simulations are validated against experiments. Furthermore, overwash and scattering behaviours are demonstrated, and their roles in the wave-ice interaction are analysed in detail.

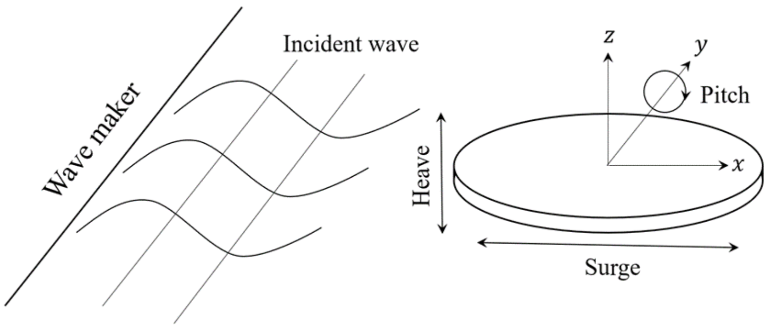

Figure 3-1: Schematic of the case: a circular ice floe is freely floating on the water surface and subjected to incoming regular waves generated by a numerical wavemaker, where the surge, heave and pitch motions are its main hydrodynamic responses

A version of this chapter has been published as: Huang, L., and Thomas, G., 2019. Simulation of wave interaction with a circular ice floe. *Journal of Offshore Mechanics and Arctic Engineering*, 141(4).

3.1 Computational modelling

3.1.1 Boundary conditions

A three-dimensional cuboid computational domain was established, defined by the earth-fixed Cartesian coordinate system $O-xyz$, as shown in Figure 3-2. The (x,y) plane parallels the undistributed water surface, and the z-axis is positive upwards. The computational domain is 2 m wide and 1 m high, and its length is five times of the target wavelength (λ). A no-slip wall condition was applied to the bottom boundary to model the presence of the seabed, and a static pressure condition was defined to the top boundary to account for the atmosphere. The domain was filled with water to a depth of $d = 0.83$ m, and the water surface was initialised as still. This water depth in is set as per the experiments of Yiew et al. [19] for the purpose of validation. The inlet boundary was set at the left, where regular waves are continuously generated and propagating towards the positive x-direction, and a wave absorption zone was placed at the outlet to eliminate the reflection of waves from the outlet boundary. The wave generation and absorption are both one-wavelength long and mathematically realised by prescribing the free surface elevation and velocity components, as introduced in Section 2.1.4.

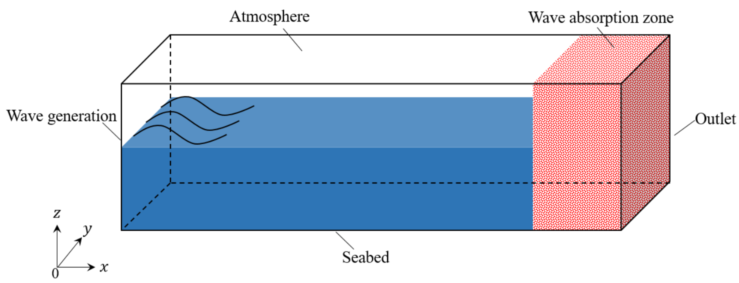

Figure 3-2: Sketch of the computational domain and the applied boundary conditions

For the purpose of validation, the ice and wave parameters set in this study follow an accordant manner with the experiments of Yiew et al. [19]. As shown in Figure 3-3, two rigid disks, with and without an edge barrier, were employed to model ice floes, named as Disk B and Disk NB respectively. The edge barrier attached on Disk B can prevent waves from flowing onto the upper surface of the disk, so that the influences of overwash can be investigated by comparing the wave response of the two disks. The density of the disks was set at 636 kg/m^3.

Each disk was initialised as floating on the undistributed water surface, with its mass centre locating at two wavelengths away from the inlet in the x-direction, the middle section of the y-direction and its buoyancy-gravity equilibrium position in the z-direction. The tested wave conditions cover a wavelength from λ = 0.69 $\sim$ 4.91 m combined with a wave amplitude of a = 10 $\sim$ 40 mm. For each single wave condition, the two disks were put into the CFD model separately.

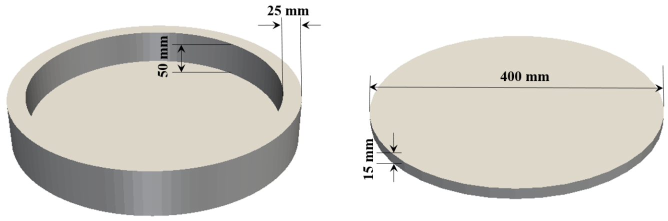

Figure 3-3: The geometry of the two disks. Left panel: the disk with an edge barrier (Disk B); right panel: the disk without edge barrier (Disk NB)

With the generated waves continuously propagating from the inlet to the outlet, the positioned disk is expected to leave its initial equilibrium position and move with the incoming waves. No artificial restraint was applied to the movement, so the disk was allowed to move freely. The wave-induced movement of a disk can be considered as the combination of translation and rotation, which was solved with the rigid-body motion equations in the body-fixed system based on the mass centre of the disk $G-x'y'z'$, as expressed in Equation (2.18) and (2.19).

3.1.2 Discretisation

The computational domain was divided into a hexahedral mesh, as shown in Figure 3-4. Local mesh refinements were applied at the free-surface area and the area where the disk is expected to move. The cells around the floating disk are partially blocked by the disk volume, and the blockage is described by fractional cell volumes and areas on cell sides [123]. The blockage updates after each timestep to satisfy a two-way coupling between the fluid solutions and floe movement.

The size of each timestep was determined by a prescribed value, Courant number (Co):

$$Co = \frac{v\Delta t}{\Delta x} \tag{3.1}$$

where Δt is the timestep size, $v/\Delta x$ is its normal velocity divided by the distance between the cell centre and the neighbour cell centre. For every timestep, there exists a maximal $v/\Delta x$ value in the domain, and Δt can be calculated by the product of that value and Co. This allows an optimal Δt being selected according to the transient fluid state. The value of Co was prescribed at 1 in this study, which is a rule-of-thumb value for similar problems. The computation was performed using the Flow-3D solver [124], where the RANS equations coupling with VOF were solved through FVM, alongside the renormalisation-group $k-\varepsilon$ model [125] to account for turbulent effects, as introduced in Section 2.1.2 and 2.1.3. The renormalisation-group $k-\varepsilon$ model has shown great performance in modelling curving flows that are expected in this case [124].

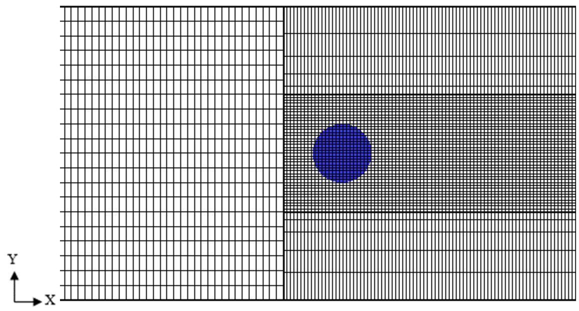

(a) Plan view

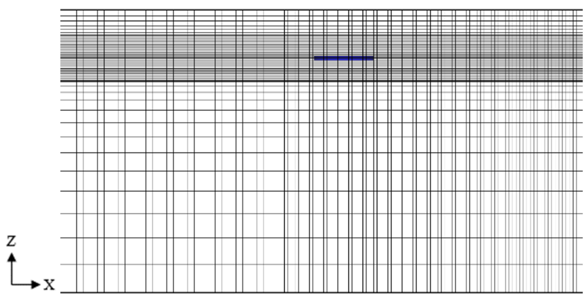

(b) Profile view

Figure 3-4: Mesh layout of the model. High resolution was applied to the free surface area and where the disk is expected to move

3.2 Results and discussion

With the waves continuously being generated and propagating, a regular wave field gradually forms in the domain, and after that, the disk is expected to conduct periodic motions with stable incoming waves. This indicates the simulation has entered its steady state, and valid data were taken only after the periodic motions begin.

The wave-induced disk movement was decomposed into 6-DOF motions for analysis. As the incident waves are unidirectional, the wave-induced movement of a disk is basically within the $x-z$ plane, composed by translational motions along the x-axis and z-axis, alongside a rotational motion along the y'-axis, i.e. surge, heave and pitch. The surge is a combination of a harmonic oscillation with a drift, while the heave and pitch are just harmonic oscillations. These harmonic oscillations were induced by the elliptical wave motion, while the drift was forced by the wave celerity.

To investigate the relationship between the disk motions and incident waves. The surge, heave, pitch amplitudes were calculated and compared with the corresponding wave motion amplitudes through the Response Amplitude Operators (RAOs). After the drift was eliminated, the surge amplitude (a_s) was calculated as half the difference between the average peak and trough values of its oscillation, and the heave amplitude (a_H) and pitch amplitude (a_P) were calculated through the same procedure. Subsequently, the motion amplitudes were used to obtain the RAOs, following:

$$RAO_{surge} = \frac{a_S}{a \coth kd} \tag{3.2}$$

$$RAO_{heave} = \frac{a_H}{a} \tag{3.3}$$

$$RAO_{pitch} = \frac{a_P}{ka} \tag{3.4}$$

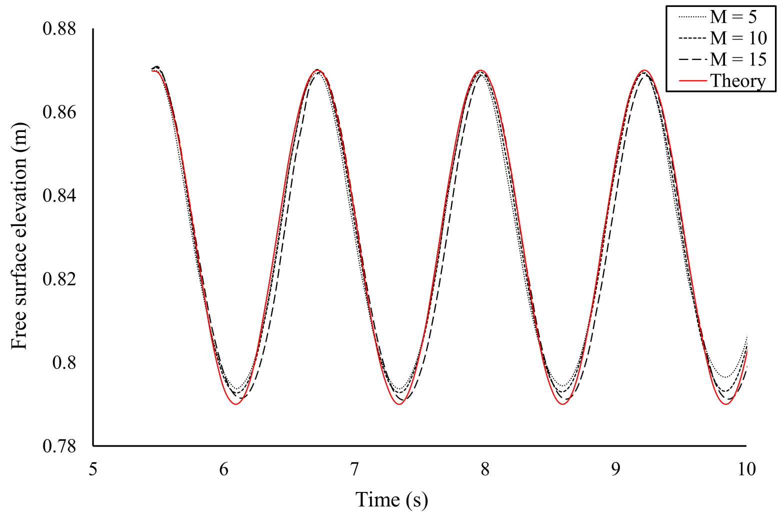

Figure 3-5: Generated waves with different cell numbers per wave height. The target waves are of λ = 2.38 m and a = 40 mm

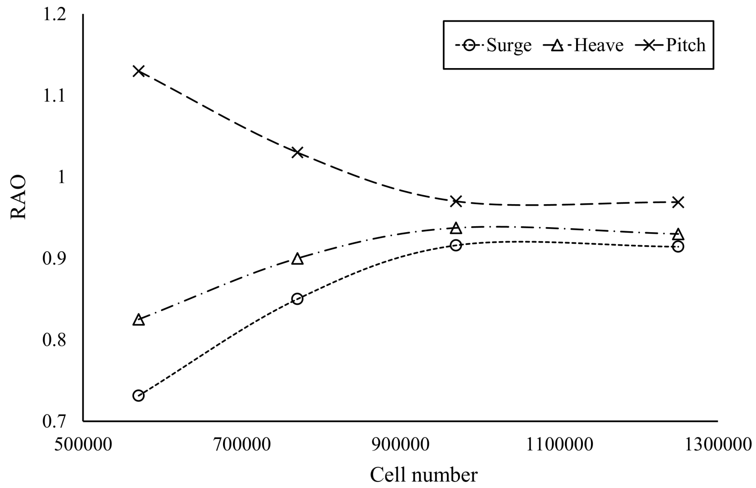

Figure 3-6: RAOs obtained with different total cell numbers. The applied wave condition was λ = 2.38 m and a = 40 mm

3.2.1 Mesh sensitivity tests

As the computational cost increases with the cell number, mesh sensitivity tests aim to get an accurate solution with as few cells as possible. In this work, two tests were conducted. The first test was to verify the quality of wave generation and propagation. For the large wavelength and small amplitude waves that are of interest, at the free surface area the mesh density is sensitive in the vertical direction.

Therefore, the cell number per wave height (M) was varied to see the influence on generated waves, from M = 5 $\sim$ 15. For the mesh density in the wavelength direction, 100 cells per wavelength were always used, which is the minimal cell number matching with M = 5 $\sim$ 15 to secure an error of less than 1% [126]. In the wave tests, the floating disk was taken away and replaced by a probe to record the free surface elevation. Figure 3-5 presents the recorded free surface elevation at different M values, alongside the ideal value. Based on the test, M = 15 was chosen to generate the mesh around the free surface, as the wave field obtained at this density was very close to the target.

The second test was conducted to secure proper solving of the disk motions. The mesh density was globally scaled, and four sets of mesh were produced, consisting of 570k, 770k, 970k and 1.25 million cells respectively. The RAOs of the disk were calculated with the four meshes respectively, and the results are shown in Figure 3-6. It shows the RAOs converge to stable values with the cell number increased, and the convergent RAO values are close to the experimental data of Yiew et al. [19]. The cell number of 970k was selected, as further increasing the cell number did not effectively improve the results. This set of mesh corresponds to around 40 cells per disk diameter (D) and 6 cells per disk thickness.

3.2.2 Validation

The CFD model was validated against the experiments conducted at the University of Tasmania [19]. For the simulations at different wavelength and amplitude conditions, computational results include the surge, heave, pitch RAOs of both Disk B and Disk NB. The comparison between the computational results (CFD) and experimental data (Exp.) is presented in Figure 3-7, as a function of non-dimensional incident wavelength (λ/D). For error analysis, the deviation between the two results was calculated as:

$$Deviation = \frac{|CFD - Exp.|}{Exp.} \times 100\% \tag{3.5}$$

Overall, the CFD model demonstrates a good agreement with the experiments in predicting the disk motions. For surge, heave and pitch, the mean deviations are 2.4%, 2.5% and 2.8% respectively. The deviation does not vary significantly at any specific wavelength or amplitude regime. This is because the mesh density of each simulation was set according to the incident wave condition, rather than a constant size. As the deviations are slight and there is no obvious over/under-estimate trend identified, the deviations can be considered as the uncertainty of numerical calculation [127] or experimental measurement, which means the applied CFD approach is reasonable and accurate.

The average deviations of Disk B and Disk NB are similar, at 2.7% and 2.4% respectively. Previous studies found it difficult to predict the motions of Disk NB. For example, for the RAOs predicted by the potential-flow/thin-plate model, the average deviations for the three motions are $1\% \sim 4\%$ for Disk B but increase to $4\% \sim 7\%$ for Disk NB [19]. The reason for this difference is the existence of overwash with Disk NB. The study of Bennetts and Williams [128] also indicates that the presence of overwash causes considerable inaccuracy to their prediction models.

Overwash has been found to be a highly nonlinear process [22], so it is hard to be included in a linear model. Even for a fully nonlinear CFD model, the method to model the free surface should be carefully chosen. For example, the free surface can also be considered as single-phase by enforcing the free surface boundary conditions on it [129]. This method is not applicable in an overwash situation, where the overwash water can be discontinuous on the floating body [128], so it can no longer be treated as a continuous boundary. Therefore, a two-phase modelling via the VOF method is recommended to handle the overwash problem. Using an appropriate turbulent model is also important, since turbulent flow has been observed when strong overwash happening [22].

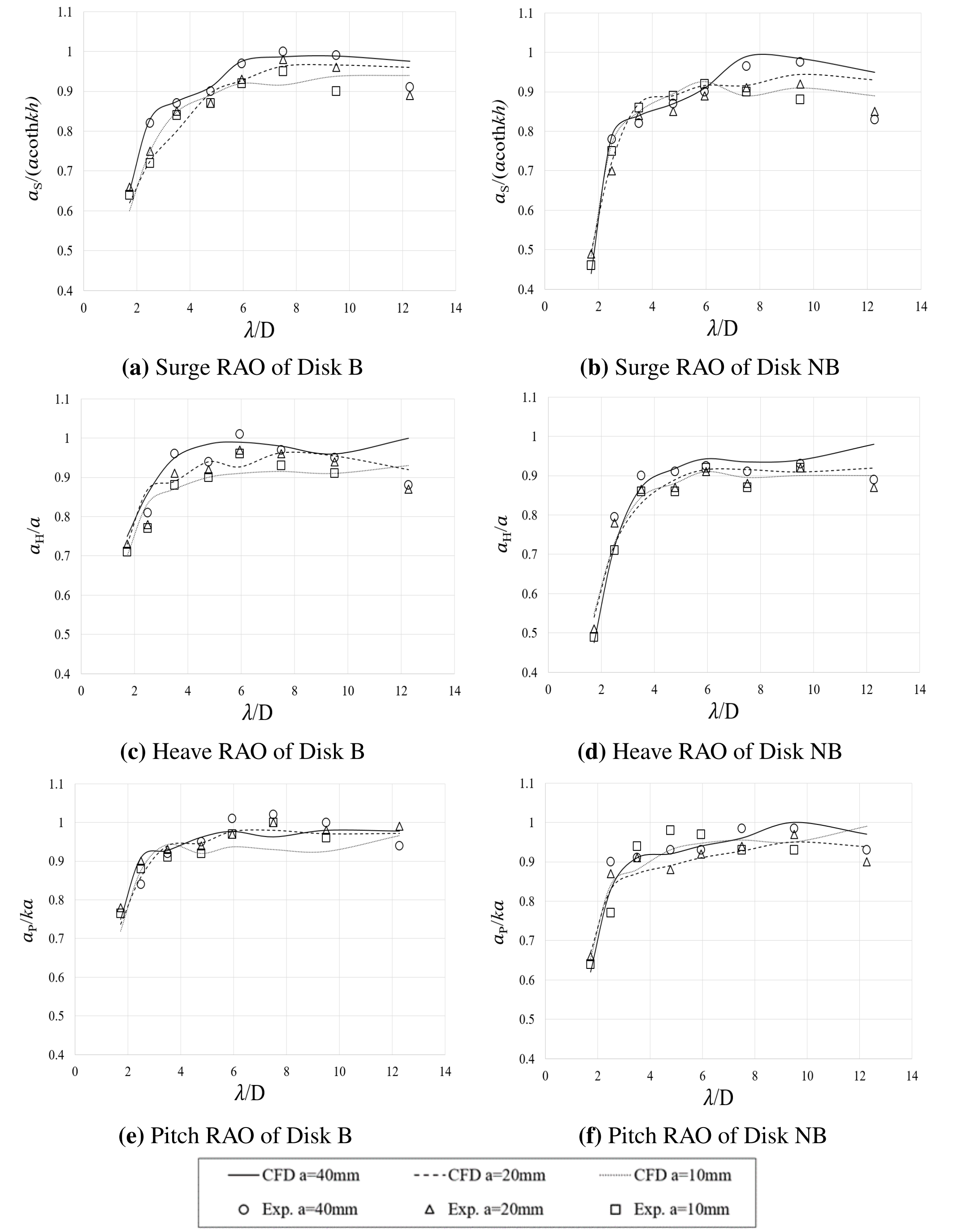

(a) Surge RAO of Disk B

(b) Surge RAO of Disk NB

(c) Heave RAO of Disk B

(d) Heave RAO of Disk NB

(e) Pitch RAO of Disk B

(f) Pitch RAO of Disk NB

Figure 3-7: Computational and experimental [19] RAOs, as a function of non-dimensional wavelength

3.2.3 Overwash

Overwash was observed in the simulations of Disk NB. The extent of overwash generally gets stronger with a larger wave amplitude or a smaller wavelength. From weak to strong, two types of overwash were identified, named partial overwash and full overwash. Both are presented in Figure 3-8. The process of partial overwash is shown in (a) and (c): water only washes over the head and tail areas of the disk; full overwash is shown in (b) and (d): water flows through the upper surface of the disk.

Since overwash was prevented by the edge barrier of Disk B, the influence of overwash was investigated by comparing the wave response of Disk B and Disk NB. Figure 3-9 shows the RAOs of both the disks, together with the observed overwash type. Data were selected from the largest wave amplitude group ($a = 40mm$) and in short-wave conditions, where overwash was most obvious. Overwash was inconspicuous in a long-wave condition (when $\lambda/D > 3$). It can be seen that Disk NB generally has smaller RAOs than Disk B. RAO difference between the two disks is most significant for the heave and least for the surge. For surge and heave, the RAO difference increases with a stronger overwash. This results from the load of the overwash water on top of the disk, which suppresses the transitional movement of the disk. Pitch seems to be unaffected by partial overwash, which means the water at head and tail areas of the disk may provide a rotational torque, acting as an offset to the overwash suppression. In contrast, full overwash can notably suppress pitch.

The influence of wave amplitude on overwash is presented in Figure 3-10, where only heave RAO is presented since surge and pitch reveal similar trends. It shows the RAO of Disk B is insensitive to wave amplitude. For Disk NB, its RAO is insensitive to wave amplitude when partial overwash occurs. However, when full overwash appears, the RAO decreases obviously as wave amplitude increases. This is because a larger wave amplitude increases the water depth above the disk, which can enhance the suppressing effect. The fact that the RAOs vary with wave amplitude signifies the nonlinearity of overwash. In the linear theory, the RAOs should be constant values for a single wavelength, but the present results indicate such a theory is not applicable when notable overwash occurs.

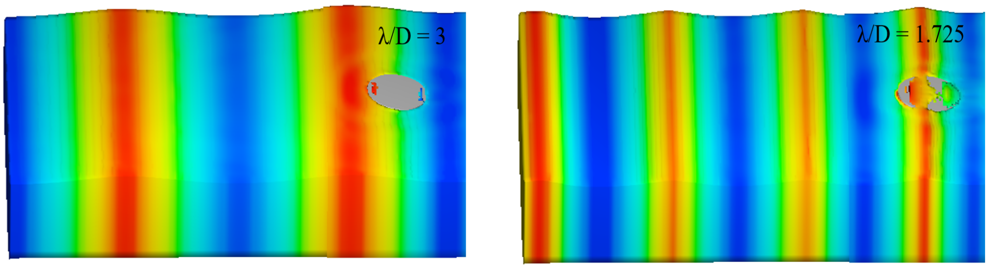

(a) Partial overwash overview **(b)** Full overwash overview

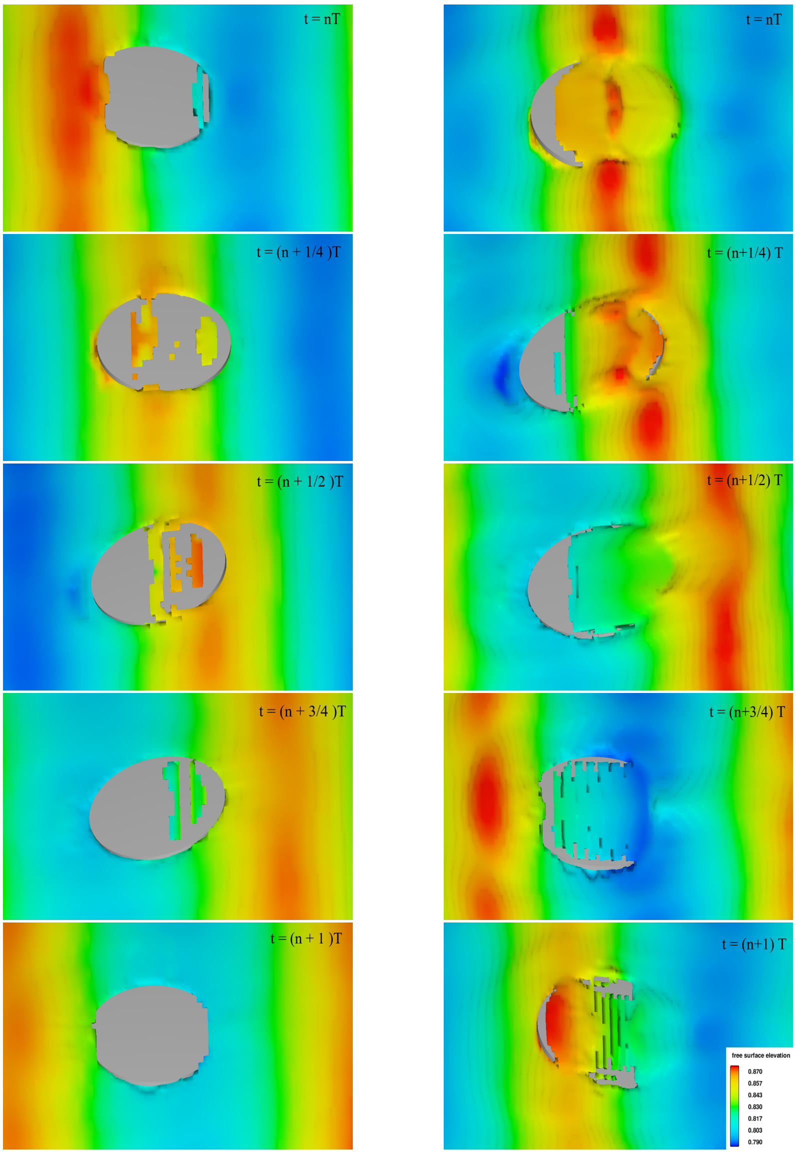

(c) Partial overwash close-up animation **(d)** Full overwash close-up animation

Figure 3-8: CFD illustration of partial overwash and full overwash

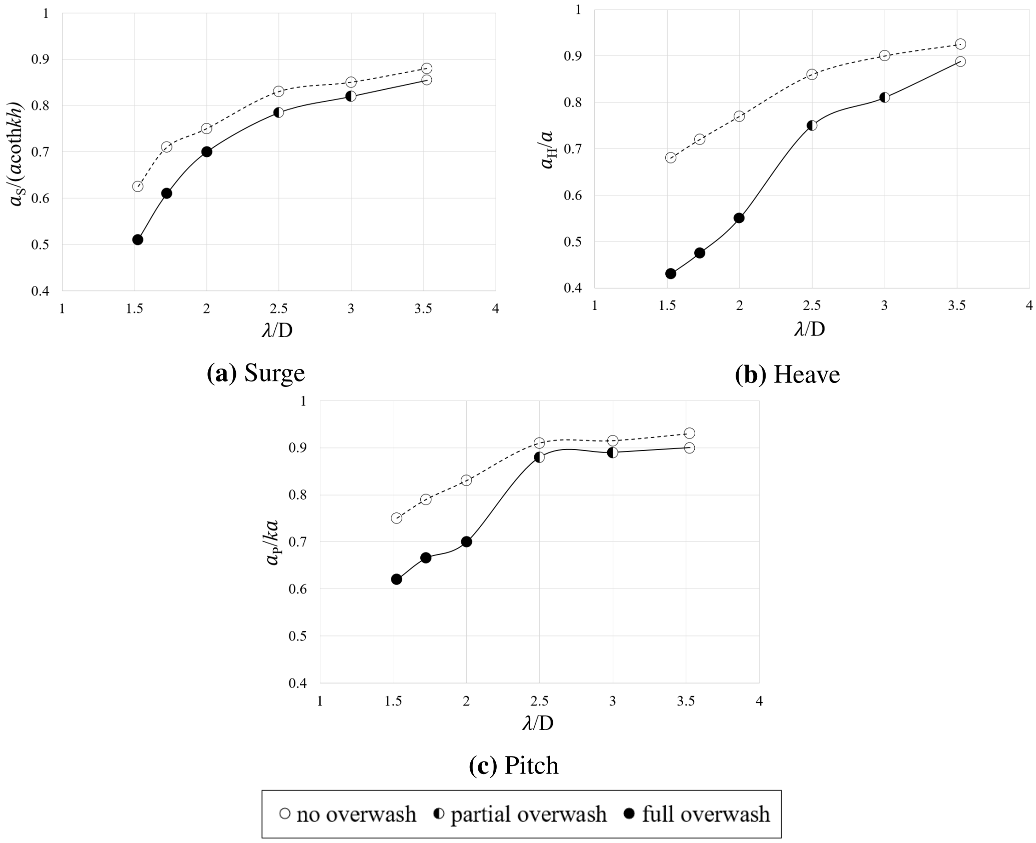

(a) Surge

(b) Heave

(c) Pitch

Figure 3-9: RAO comparisons between Disk B (dashed line) and Disk NB (solid line), as a function of non-dimensional wavelength, alongside the type of overwash

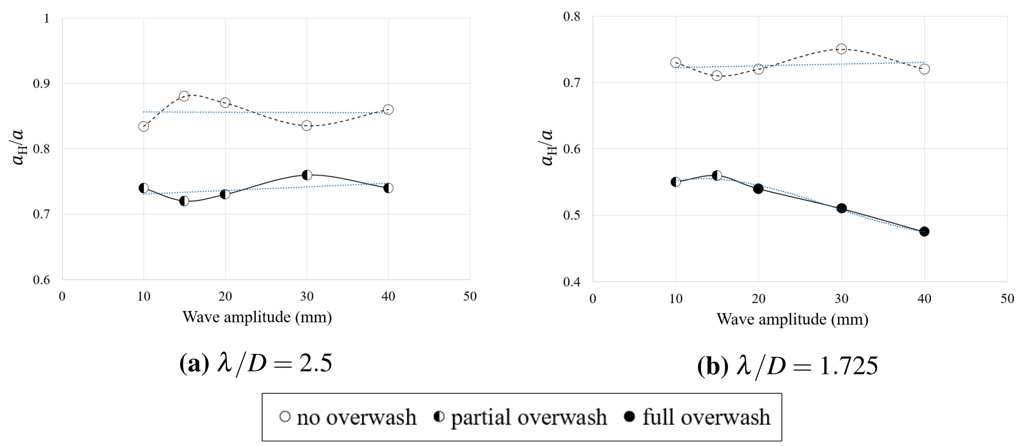

(a) $\lambda/D = 2.5$

(b) $\lambda/D = 1.725$

Figure 3-10: Heave RAO of Disk B (dashed line) and Disk NB (solid line), as a function of wave amplitude, alongside the type of overwash. Trend lines (blue) are also included

3.2.4 Scattering

The disks were observed to reveal varying wave-ice interactions with the incident wavelength changed. When a disk is subjected to long waves, it hardly influences the wave transmission. By contrast, in short waves, a disk can scatter the incoming waves, which generates directional-spreading waves surrounding the disk and influences the transmitted waves. Examples are shown in Figure 3-11, where Disk B is presented, in order to eliminate the distraction of overwash. In a long-wave condition, wave scattering is not obvious, and the waves are nearly intact after passing through the disk, as shown in Figure 3-11 (a). At a shorter wavelength, wave scattering becomes visible, while the waves can still transit with the incident amplitude, except the part right behind the disk is distorted, as shown in Figure 3-11 (b). For even shorter waves, a stronger scattering can be observed, and the transited waves are significantly attenuated, as shown in Figure 3-11 (c).

The disk motions are related to the scattering phenomenon. As shown in Figure 3-7, in the long-wave regime ($\lambda/D > 3$), wave scattering is negligible and the RAOs are close to one, which means the disk approximately moves at the same amplitude of the incident waves, agreeing with the fact that the wave transmission is unaffected. In the short-wave regime ($\lambda/D < 3$), the RAOs start to decrease rapidly with the scattering becomes stronger, since the scattering can attenuate the incident waves so that the disk motions cannot be induced at the original wave amplitude.

Although both scattering and overwash have been found as sources to disturb the incident wave and can reduce the disk RAOs, they reveal different relationships with the incident wave amplitude. As shown in Figure 3-10, for Disk B, where only scattering occurs, the RAO is insensitive with a changed incident wave amplitude, which suggests a linear effect of scattering on the disk motions. However, for Disk NB, overwash has shown obvious nonlinearity on the disk motions. This explains why the linear potential-flow/thin-plate model can predict the RAOs accurately in a scattering condition as long as there is no overwash.

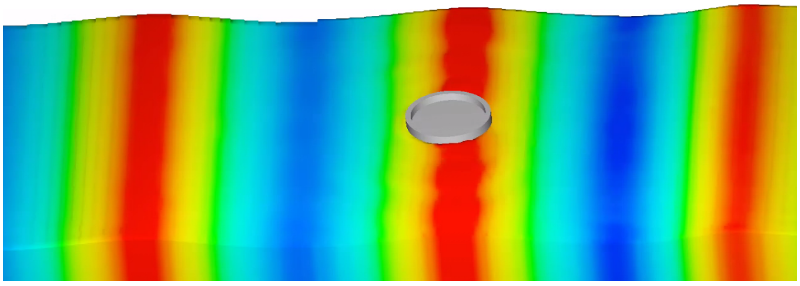

(a) $\lambda/D = 3.525$

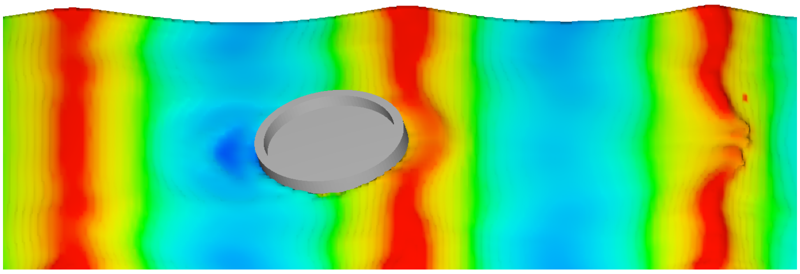

(b) $\lambda/D = 2$

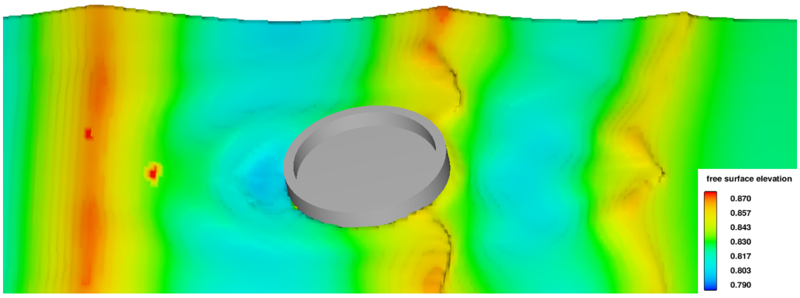

(c) $\lambda/D = 1.525$

Figure 3-11: The interaction of Disk B with waves, at different wavelengths

3.3 Conclusions

A CFD model has been presented to model the interaction of regular waves with an ice floe. The ice floe was treated as a floating rigid disk to represent the pancake-ice scenario, and it was subjected to waves of large wavelength and small amplitude, according to the common environment in the MIZ. A series of simulations were conducted to investigate the behaviour of the ice floe in different wave conditions, and the wave-induced surge, heave and pitch motions of an ice floe were presented as RAOs to analyse their relationship with incident waves. The computational results were compared with the corresponding experimental data, showing the proposed approach is capable of simulating the wave-ice interaction including overwash, to which previous analytical models have been reported to contain inaccuracy.

Two specific behaviours with the wave-ice interaction were displayed within the simulations, namely overwash and scattering. Both tend to happen in a short-wave condition and were found to be significant sources to cause wave dissipation and reduce the ice floe motions. The scattering and ice floe motions were found to follow a linear relationship that is not affected by a changed wave amplitude, but such a relationship becomes nonlinear when overwash occurs, where a larger wave amplitude can increase the water depth on top of an ice floe, resulting in extra load to suppress the motions.

In this chapter, a valid CFD approach has been developed that can provide high-fidelity simulations for wave interactions with a floating ice floe, where the floe is assumed as rigid based on its relatively small dimension. The next step is to develop a computational approach that can account for the elastic deformation of sea ice in waves, thus covering the modelling of relatively large ice floes/sheets - this will be presented in the next chapter.

Chapter 4

Wave interaction with an elastic ice sheet

The wave response of a large ice sheet is dominated by an elastic deformation other than rigid body motions. This chapter reports work on simulating the hydroelasticity of sea ice in regular waves, as depicted in Figure 4-1. Particularly, a novel FSI solver is developed to enable full coupling between the wave motion and ice deformation. Based on this new solver, the practicalities to simulate the hydroelastic wave-ice interaction is presented, alongside a series of validation and extended analyses on the wave transmission & reflection, overwash and ice deformation.

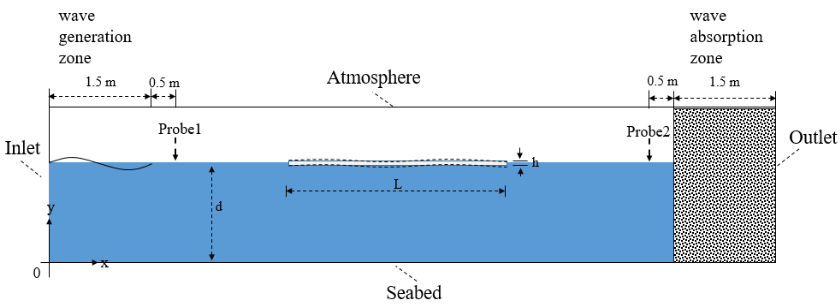

Figure 4-1: Schematic of the case: a thin ice sheet is floating on the water surface and subjected to incoming waves, with its elastic deformation enabled

A version of this chapter has been published as: Huang, L., Ren, K., Li, M., Tuković, Ž., Cardiff, P. and Thomas, G., 2019. Fluid-structure interaction of a large ice sheet in waves. *Ocean Engineering*, 182, pp.102-111.

4.1 Development of a new hydroelastic solver

To simulate the hydroelastic wave-ice interaction, CFD needs to be incorporated with an additional set of Computational Structural Mechanics (CSM) solution to account for the wave-induced ice deformations, achieving a simulation of Fluid-Structural Interaction (FSI). In order to model the present wave-ice interaction problem, first, it is essential to model the FSI with two-way coupling, as the interest is to predict the changed wavefield in the presence of deforming ice. On top of a two-way mechanism, the coupling procedure needs to go through sufficient iterations to satisfy the dynamic and kinetic conditions, i.e. fully coupling the waves and the deforming structure, so that the predicted wavefield can be enough accurate for analyses.

Commercial software is not sufficiently flexible to manage the data exchange between the CFD part and the CSM part, which limits the coupling scheme. Because of this difficulty, most contemporary FSI work is one-way coupling, e.g. [130, 131] or weakly two-way coupling, e.g. [132, 133]. These coupling schemes do not meet the requirement of the hydroelastic wave-ice interaction that should be fully two-way coupling. In addition, nonlinearly deforming fluid and solid meshes geared together are easy to cause the simulation to crash, for which, using opensource code enables full management of an under-relaxation algorithm to secure the simulation's stability.

In such a context, this work developed a new solver to simulate the hydroelastic wave-ice interaction. The new solver was built upon the opensource CFD framework, OpenFOAM, as it gave the full flexibility to modify solvers and manage simulations. Tukovic et al. [73] published an FSI code based on OpenFOAM, in which, they apply a partitioned algorithm that solves the fluid and solid mechanism separately and links them together via the fluid-solid interface, equipping the capability to build two-way FSI simulations. However, the code of Tukovic et al. [73] is only capable of modelling single-phase flows, which means it cannot be used to simulate some ocean-related cases containing multiphase flows (water and air), as in the current problem. Therefore, this work extended the code of Tukovic et al. to incorporate with the VOF method to simulate multiphase FSI problems; subsequently, the code was further added with wave modelling abilities to enable the simulation of wave-induced FSI problems. Figure 4-2 illustrates the development route of the solver. The new code and its programming report has been made publicly accessible[1]. With the new solver, the simulation of the hydroelastic wave-ice interaction became possible, and its realisation is presented as follows.

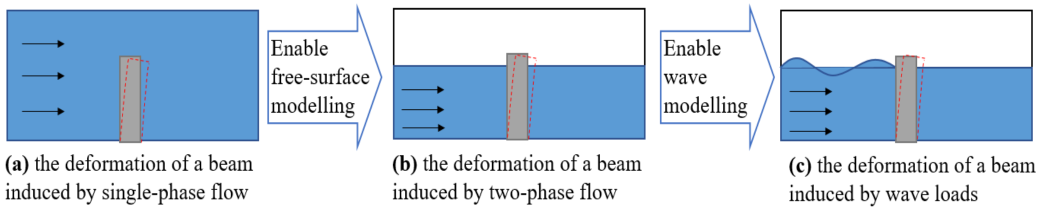

Figure 4-2: Development route of the hydroelastic solver

4.2 Computational modelling

In contrast to the traditional CFD approach that only solves governing equations for the fluid domain, an FSI simulation requires the solutions of both the fluid and solid domains, alongside a coupling scheme to link the solutions together. To achieve this, the computational domain is divided into two parts, namely the fluid sub-domain and the solid sub-domain. A numerical wave tank is established in the fluid sub-domain to model desirable wave fields, and the solid sub-domain is modelled as a thin ice sheet floating on the water surface.

4.2.1 Boundary conditions

A two-dimensional rectangular computational domain was assumed, defined by the Cartesian xy coordinate system, as shown in Figure 4-1. The x-axis is parallel to the undisturbed water surface, and the y-axis is positive upwards. The computational

[1] Huang, L., 2018. An opensource solver for wave-induced FSI problems. *In Proceedings of CFD with Opensource Software*, at: Gothenburg, Sweden.

domain (12 m long and 1.5 m high) is filled with fresh water to a depth of d with air filling the remainder of the fluid sub-domain. At the top boundary of the domain, a fixed pressure boundary condition is applied to represent atmospheric conditions. The bottom boundary is defined as a no-slip wall to account for the presence of the seabed. Periodic regular waves were generated at the inlet boundary propagating in the positive x-direction, and a wave absorption zone was placed by the outlet boundary at the right of the domain to minimise reflection of waves (see more details in Section 2.1.4). Two probes were positioned at upstream and downstream locations to record the time-varying free surface elevation. The solid sub-domain represents an ice sheet floating on the water surface according to its buoyancy-gravity equilibrium position. The length and thickness of ice are respectively denoted as L and h. The ice is fully flexible except not allowed to drift/surge with the wave.

4.2.2 Discretisation

To perform computations, the computational mesh was also divided into two parts, namely a fluid mesh for the fluid sub-domain and a solid mesh for the solid sub-domain, as shown in Figure 4-3. They are connected by placing their interface boundaries at the same location, where the fluid and solid interface meshes need not be conformal. The fluid mesh is graded towards the free surface area, while the solid mesh density is uniform. The cell numbers of both meshes were determined by sensitivity tests, as presented in Section 4.3.1. The size of each timestep was set to be 0.0005 second, following the rule that Courant number less than one (Equation 3.1).

The fluid mesh was built to obtain CFD solutions, e.g. pressure/velocity fields, through solving the Navier-Stokes equations together with the VOF method. The solid mesh was built to obtain CSM solutions, i.e. the ice deformation, which is governed by the conservation of momentum, where the stress is solved according to the nonlinear St. Venant Kirchhoff hyperelastic law. The mathematical formulae of the CFD and CSM equations are given in Section 2.1.1 and 2.2.2, respectively. Both the CFD and CSM computations were performed using the FVM method [121].

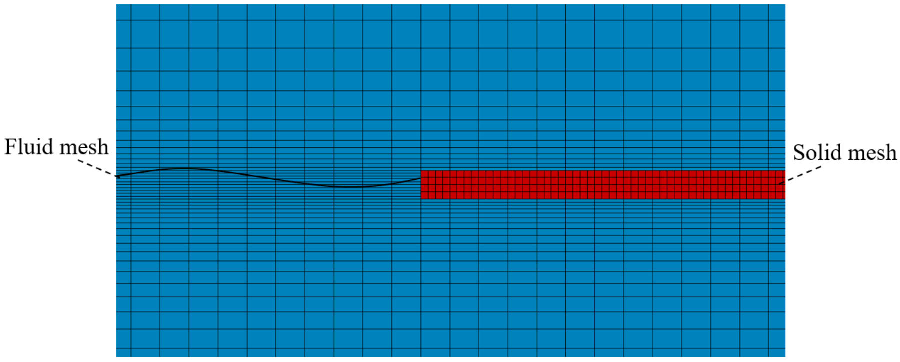

Figure 4-3: Mesh layout of the model: the fluid mesh is graded towards the free surface area, while the solid mesh is uniform

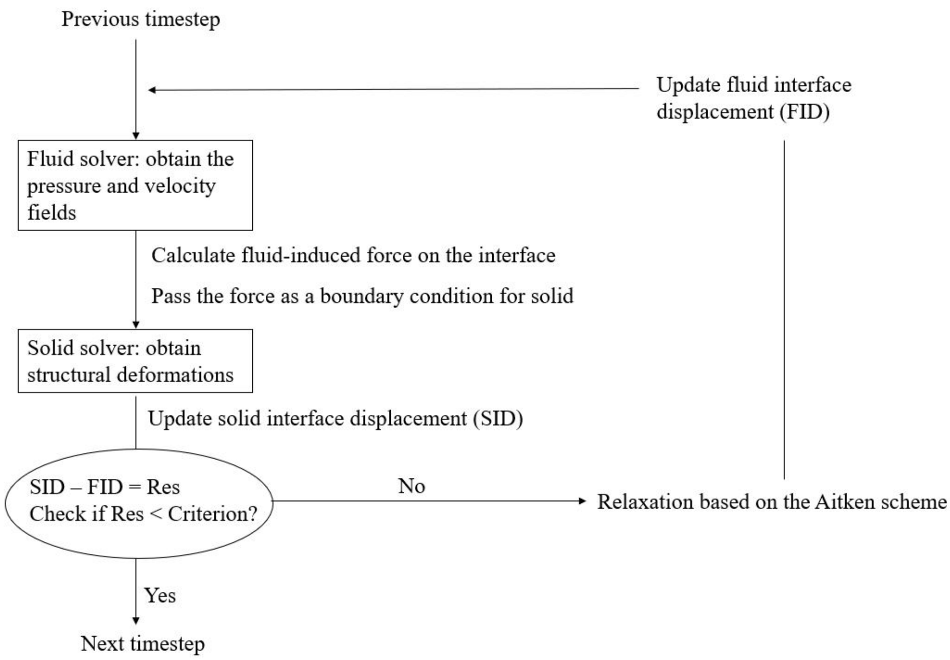

Figure 4-4: Flowchart of the FSI scheme

4.2.3 Fluid-structure interaction

The coupling between the CFD solution and the CSM solution was achieved through a partitioned scheme [118], where the fluid and structural equations are solved separately, and the kinematic and dynamic conditions are matched at the fluid-solid interface. The kinematic condition states that the velocity and displacement are continuous across the interface as expressed in Equations 4.1 and 4.2, and the dynamic condition states that forces are in equilibrium at the interface as expressed in Equation 4.3.

$$\mathbf{v}_{fluid} = \mathbf{v}_{solid} \tag{4.1}$$

$$\mathbf{u}_{fluid} = \mathbf{u}_{solid} \tag{4.2}$$

$$\mathbf{n} \cdot \mathbf{F}_{fluid} = \mathbf{n} \cdot \mathbf{F}_{solid} \tag{4.3}$$

Following the partitioned approach, a two-way fully coupling procedure is achieved in this work. First, the pressure and velocity fields are solved in the fluid sub-domain through CFD, giving fluid force on the interface. The fluid force field on the interface provides a boundary force for the solid sub-domain, where Equation 4.3 is satisfied. Then, the deformation of the solid body is solved through CSM. The deformation induces displacements of all the solid cells, and the derivative of the displacement field of the interface gives a velocity boundary field, which is passed back to the fluid sub-domain, where Equation 4.1 is satisfied. For each time step, iterations are performed until Equation 4.2 is satisfied. The iteration procedure is illustrated in Figure 4-4 and described as follows:

- At the beginning of every time step, the displacement of the solid sub-domain is updated using the results of the previous time step. Then, the Aitken coupling scheme is employed for improving the convergence speed during the coupling procedure, which introduces an Aitken Relaxation Factor (*ARF*), as defined in Equation 4.4.

$$ARF_{i+1} = ARF_i \times [1 - \frac{\sum(Res \cdot \Delta Res)}{\sum(\Delta Res \cdot \Delta Res)}] \tag{4.4}$$

  where i denotes the solution of the ith iteration. Thus the *ARF* is updated according to the current residual (*Res*), which is the difference between the structural interface displacement (*SID*) and the fluid interface displacement (*FID*), namely

$Res = SID - FID$.

- Then, the fluid mesh is adjusted with the updated ARF value, as in Equation 4.5.

$$FluidMesh_{i+1} = FluidMesh_i + ARF_{i+1} \times Res \tag{4.5}$$

- The FID is extracted from the adjusted fluid mesh. Then the derivative of FID is computed to obtain the velocity of the fluid interface, and the mesh motion of the rest of the fluid mesh is obtained according to this interface velocity.

- Using the updated mesh, the new velocity and pressure fields within the fluid sub-domain are calculated using the fluid solver.

- The velocity and pressure fields are used to calculate the fluid force on the interface, and then the force field on the interface is transferred from the fluid domain to the solid domain.

- Having the fluid force on the interface, the induced solid deformation is calculated by the structural solver, recorded as the displacement of all cells in the solid sub-domain.

- The SID is extracted from the structural displacement and then compared with the FID to update Res. The solver enters next timestep when Res is smaller than the prescribed residual criterion.

In this study, the Res criterion was set to be less than 1×10^{-4} meter, which was achieved by an average of 40 iterations per timestep.

4.3 Results and discussion

In this section, validation is presented to show the rationality and accuracy of the proposed approach, following four steps: (a) ensure target wave fields can be generated; (b) ensure the wave-induced ice deformation can be accurately calculated; (c) without overwash, correctly predict the influence of the ice sheet on wave transmission and reflection; (d) including overwash, correctly simulate the wave-ice interaction. Once the numerical approach has been validated, extended investigations are presented to discuss the role of overwash and ice deformation.

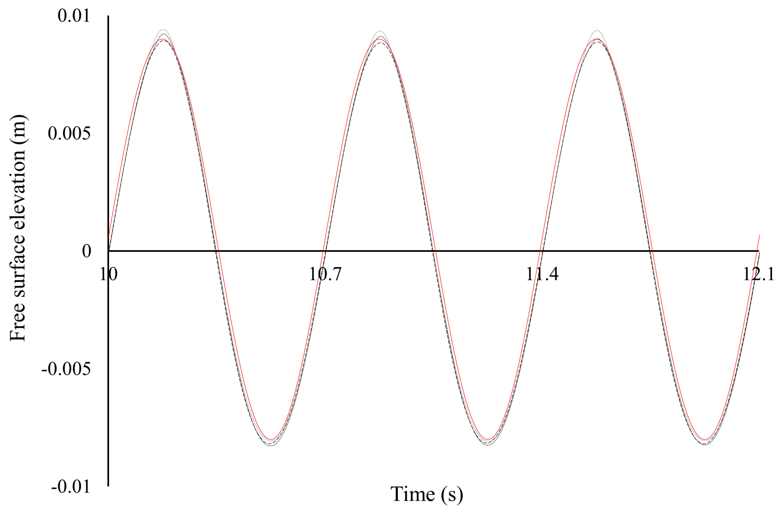

(a) Probe 1

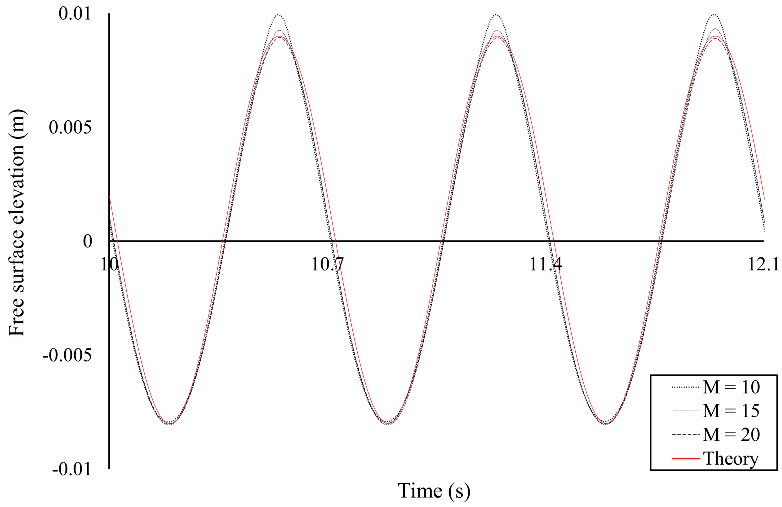

(b) Probe 2

Figure 4-5: Generated waves with different cell numbers per wave height. The target waves are of $\delta = 0.7$ s and $H = 0.017$ m

4.3.1 Mesh sensitivity tests

The FSI model was verified through two sensitivity tests for the fluid mesh and solid mesh respectively. Both aim to achieve accurate solutions with as few cells as possible, so as to minimise the computational costs. The first test was conducted to ensure the target wave field can be obtained without the presence of the ice sheet.

For waves with large wavelengths and small amplitudes waves that are of interest, the wave field can be sensitive to the vertical mesh density at the free surface area. Therefore, the fluid cell number per wave height (M) was varied to test this influence. For the mesh density in the wavelength direction, 100 cells per wavelength was used for all simulations, with which mesh-independent results were produced. To obtain the wave field, the ice sheet was taken away and the free surface elevation was recorded using the two probes illustrated in Figure 4-1. With different M values, the recorded free surface elevation is presented in Figure 4-5, alongside the target value. It is shown that the target wave field can be obtained at both upstream and downstream locations of the ice sheet when M $\geq$ 15, which means a high quality of wave generation and propagation throughout the computational domain. Therefore, this study chose M = 15 for the fluid mesh density.

The second test was conducted to select an appropriate mesh density to capture the elastic deformation of the ice sheet. The solid mesh density was globally scaled, resulting in four meshes consisting of 200, 400, 800 and 1200 cells respectively. With the four meshes, the wave-induced deformation was measured at different locations of the ice sheet, and the measured vibration amplitudes are presented in Figure 4-6, alongside a comparison with the experimental data of Sree et al. [20]. The relative deviations between computational and experimental results are shown in Table 4-2. The model predictions generally agree with the experimental results. Deviations between model and experimental results are small when the solid cell number is larger than 400, so the mesh set of 400 cells was selected for further simulations, corresponding to 100 cells per ice length and 4 cells per ice thickness.

4.3.2 Validation

Validation of the model includes two parts. The computational results were first compared with the experimental data of Nelli et al. [21] to assess the accuracy of the model to predict wave reflection and transmission against the ice sheet. In this part, edge barriers were attached to the ice sheet to avoid wave overwashing, as shown in Figure 4-7a. In the second part, the edge barriers were removed to enable

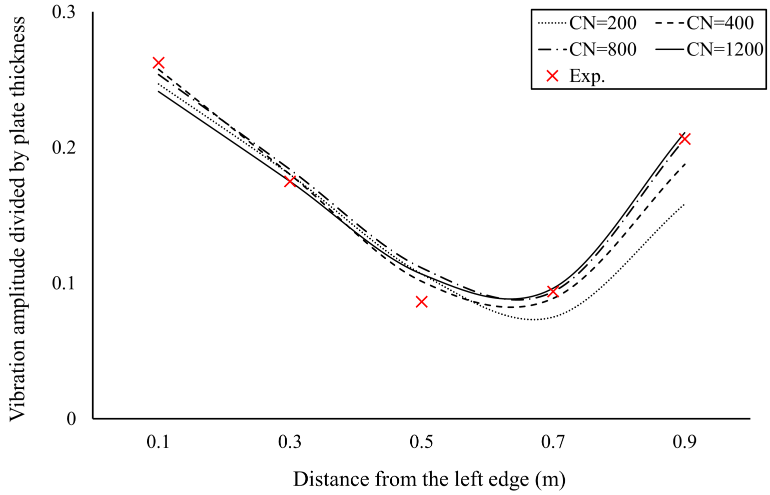

Figure 4-6: Vibration amplitude at different locations of the ice sheet, obtained with a range of solid cell number (CN). Experimental data of Sree et al. [20] are also included. The plate length is 1 m in total and the x-axis shows the measured distance from its left edge. Applied wave and ice conditions are shown in Table 4-1: Case 19.

overwash as shown in Figure 4-7b, and the mean depth of the overwash water was recorded and compared with the experimental data of Skene et al. [22].

(a) Without overwash

(b) With overwash

Figure 4-7: Simulation examples of the wave interaction with a large floating ice sheet

Table 4-1: Parameters of the Simulation Cases

Case	Wave condition	Ice condition	Water Depth
1	δ = 0.8 s, λ = 1 m, H = 0.025 m (ka = 0.08)	L = 1 m, h = 0.01 m, $\rho_{ice} = 905\ kg/m^3$, E = 1.6 GPa, ν = 0.4, with & without edge barriers.	d = 0.9 m
2	δ = 0.8 s, λ = 1 m, H = 0.032 m (ka = 0.10)		
3	δ = 0.8 s, λ = 1 m, H = 0.038 m (ka = 0.12)		
4	δ = 0.9 s, λ = 1.26 m, H = 0.032 m (ka = 0.08)		
5	δ = 0.9 s, λ = 1.26 m, H = 0.040 m (ka = 0.10)		
6	δ = 0.9 s, λ = 1.26 m, H = 0.048 m (ka = 0.12)		
7	δ = 1.0 s, λ = 1.56 m, H = 0.039 m (ka = 0.08)		
8	δ = 1.0 s, λ = 1.56 m, H = 0.049 m (ka = 0.10)		
9	δ = 1.0 s, λ = 1.56 m, H = 0.059 m (ka = 0.12)		
10	δ = 0.6 s, λ = 0.56 m, H = 0.007 m (ka = 0.04)	L = 1 m, h = 0.02 m, $\rho_{ice} = 905\ kg/m^3$, E = 1.6 GPa, ν = 0.4, without edge barriers.	d = 0.5 m
11	δ = 0.6 s, λ = 0.56 m, H = 0.014 m (ka = 0.08)		
12	δ = 0.6 s, λ = 0.56 m, H = 0.018 m (ka = 0.10)		
13	δ = 0.8 s, λ = 1 m, H = 0.013 m (ka = 0.04)		
14	δ = 0.8 s, λ = 1 m, H = 0.026 m (ka = 0.08)		
15	δ = 0.8 s, λ = 1 m, H = 0.032 m (ka = 0.10)		
16	δ = 1.0 s, λ = 1.51 m, H = 0.019 m (ka = 0.04)		
17	δ = 1.0 s, λ = 1.51 m, H = 0.038 m (ka = 0.08)		
18	δ = 1.0 s, λ = 1.51 m, H = 0.048 m (ka = 0.10)		
19	δ = 0.7 s, λ = 0.755 m H = 0.017 m (ka = 0.07)	L = 1 m, h = 0.01 m, $\rho_{ice} = 910\ kg/m^3$, E = 870 MPa, ν = 0.3, with edge barriers.	d = 0.3 m

Table 4-2: Relative Deviation of Ice Deformation with Different Solid Mesh Densities

	Point A	Point B	Point C	Point D	Point E
CN = 1200	-7.0%	+0.1%	+24.4%	+2.6%	+2.2%
CN = 800	-3.3%	+5.0%	+26.9%	+0.1%	+0.1%
CN = 400	-1.9%	+2.8	+21.6%	-5.0%	-9.0%
CN = 200	-6.0%	+2.8%	+31.4%	-20.0%	-23.0%

In accordance with the experiments of Nelli et al. [21], simulations were carried out with a range of wave conditions, from short to long and from gently-sloping to storm-like, listed in Table 4-1 as Cases 1-9. Wave transmission and reflection are denoted as the wave energy measured by the two probes, for which both probes

Table 4-3: Relative Deviations of R & T and Mean Overwash Depth

	R	T		overwash depth
Case 1	+2.3%	+2.4%	Case 10	+0.1%
Case 2	-9.1%	-1.8%	Case 11	-17.2%
Case 3	+13.3%	-5.1%	Case 12	+36.7%
Case 4	+8.0%	-3.7%	Case 13	-3.0%
Case 5	+22.5%	+0.6%	Case 14	+11.4%
Case 6	-5.4%	-0.2%	Case 15	+44.1%
Case 7	-15.1%	+1.7%	Case 16	+23.0%
Case 8	+11.4%	+5.6%	Case 17	-7.7%
Case 9	-25.6%	+8.1%	Case 18	+77.8%

were placed far enough from the ice sheet to avoid the disturbance from breaking waves. To process data, the free surface elevation measured by both probes was analysed by a Fast Fourier Transform to obtain the wave energy spectrum, and the wave energy was the integration of the energy spectrum over the frequency domain:

$$\Psi = \frac{1}{2}\int_0^{\infty} \hat{a}^2 df \tag{4.6}$$

where $\hat{a}(f)$ is the wave amplitude component at each frequency f. The wave energy at the upstream/downstream probe location was recorded as Ψ_{front} and Ψ_{rear}, where Ψ_{rear} denotes the transmitted waves while Ψ_{front} is a superposition of the ice-reflected waves and the incident waves. Thus, the reflection (R) and transmission (T) coefficients were calculated based on their ratio to the incident wave energy $\Psi_{incident}$:

$$R = \frac{\left|\Psi_{front} - \Psi_{incident}\right|}{\Psi_{incident}} \tag{4.7}$$

$$T = \frac{\left|\Psi_{rear}\right|}{\Psi_{incident}} \tag{4.8}$$

The comparison between computational and experimental results is shown in Figure 4-8 and Table 4-3, where good agreement can be seen for all the examined wavelength and wave height conditions. With increasing wavelength, T increases and R decreases, which means a better transmission appears with longer incident waves. Noting that overwash was avoided at this stage, R and T are insensitive to changes in the wave height, agreeing with the assumption of the linear theory [68]. Moreover, R + T approximately equals to one in these cases without overwash, which means energy dissipation is negligible in such a situation.

A further validation was conducted to assess the capability of the model to simulate overwash. According to the experiments of Skene et al. [22], the depth of overwash water was measured at the middle of the ice surface, using a set of wave conditions listed in Table 4-1 as Cases 10-18. The comparison between computational and experimental mean water depth is shown in Figure 4-9 and Table 4-3. It can be seen that overwash depth from the model reveals a consistent trend with the experiments: it increases with increasing wave height and wavelength. In this case, overwash increases with longer waves ($1 < \lambda/L < 1.56$), which is opposite to the trend observed in the interaction of waves with a small circular ice floe, where overwash was found to decrease with an increased wavelength ($\lambda/D \geq 1.5$), as discussed in Section 3.2.3. This difference indicates that the extent of overwash is also dependant on the dimension of ice, relative to the dominating wavelength; overwash appears to be strongest when the wavelength is around 1.5 times of the ice dimension, while either shorter or longer waves tend to induce smaller overwash. A notable deviation exists for the case of the largest wave height, i.e. Case 18, where the model overpredicts the overwash depth. This can be attributed to the turbulence occurring with such waves of very large height, as observed in the experiments of Skene et al. [22]. Turbulence is a source of energy dissipation that can lead to a weaker overwash [56], thus future work should consider including an appropriate turbulence model to predict the complex overwash flow occurring during storm-like conditions.

4.3.3 Overwash

To investigate the influence of overwash on R and T. Cases 1-9 were simulated again but this time the edge barriers were taken away, thus overwash was enabled for the same wave conditions. The comparison was made between the results with and without overwash, as shown in Figure 4-10. It can be seen that both the R and T with overwash are smaller than those without overwash. For R, the results without overwash are slightly higher than these with overwash. On one hand, the edge barriers provide a better reflection thus giving a higher R for the cases without overwash; on the other hand, wave breaking happens at the ice edge without barriers, which causes energy dissipation and results in a lower R for the cases with overwash. For T, the results are shown to be significantly reduced by overwash. The difference is most pronounced when $\lambda/L = 1.26$, while it is less obvious when $\lambda/L = 1$ and $\lambda/L = 1.56$; this indicates the reduction effect of overwash on transmission is not positively or negatively correlated to the non-dimensional ice sheet length.

With overwash, the ice sheet splits the incoming waves into the overwash water on top and hydroelastic-effect waves underneath. After passing over the ice sheet, the overwash water cannot reform waves so is not able to effectively transmit downstream. Therefore, this part of the incident waves is dissipated from transmission and reflection, resulting in $R + T < 1$. Experimental work reached the consensus that this part of energy brings about inaccuracies in current theoretical models where overwash is ignored [71, 21], which is illustrated in Figure 4-10 as the analytical solutions are similar to the computational results when overwash was avoided. Since the overwash water depth links with the incident wave height, the energy dissipation increases with increasing wave height. This does not follow the linear theory where a changed wave height is uninfluential. Thus, compared with linear analytical solutions, the present model proves to be a more realistic approach for modelling sea ice hydroelasticity including overwash.

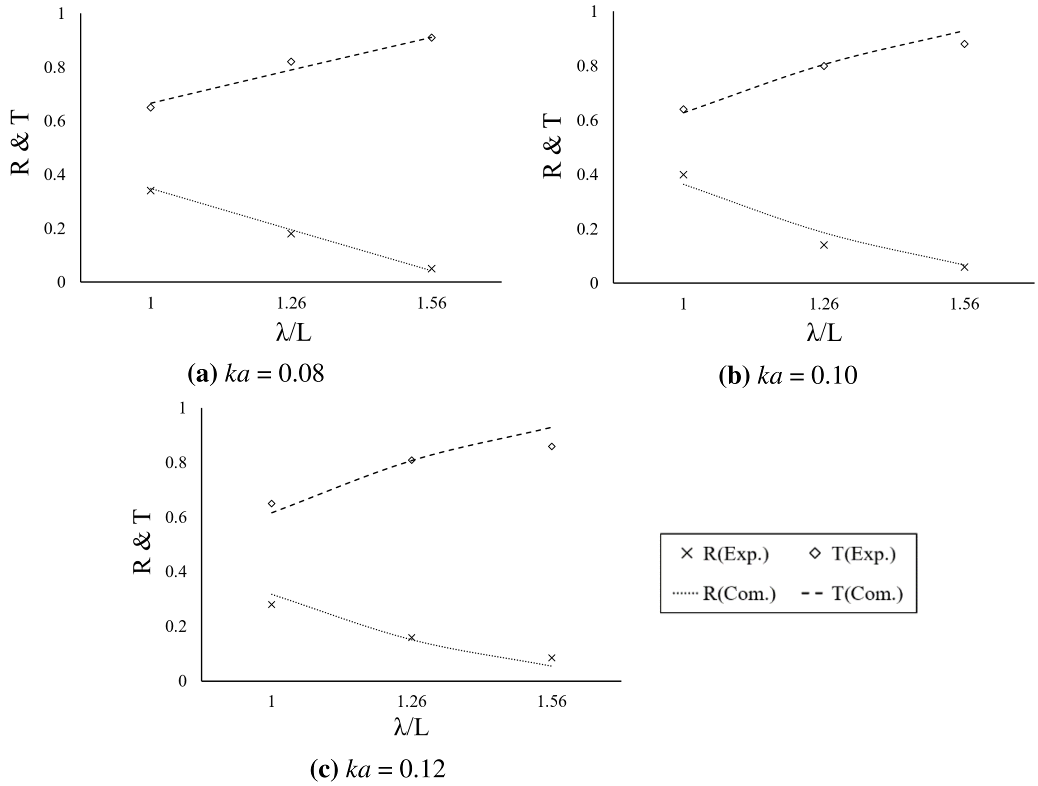

Figure 4-8: Computational and experimental R & T [21], obtained when overwash was avoided

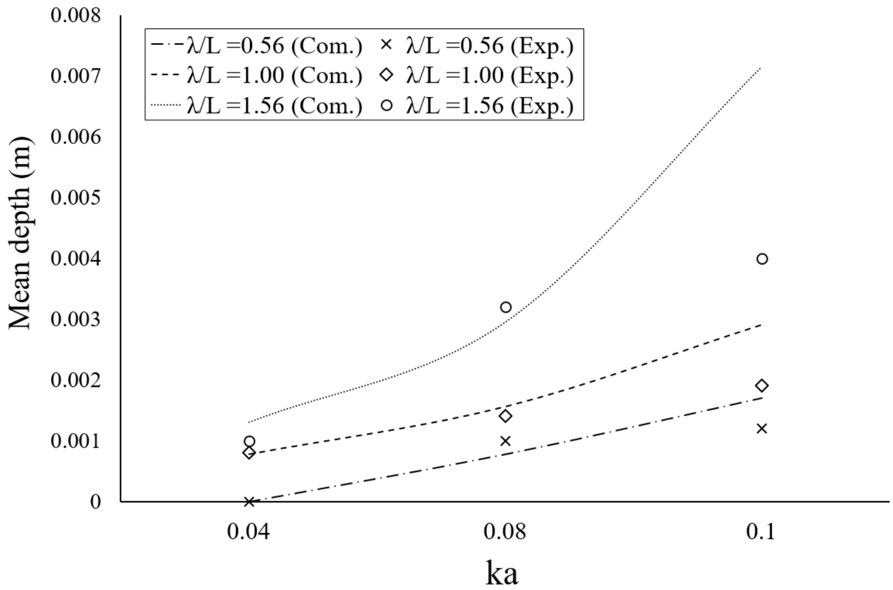

Figure 4-9: Computational and experimental [22] mean overwash depth

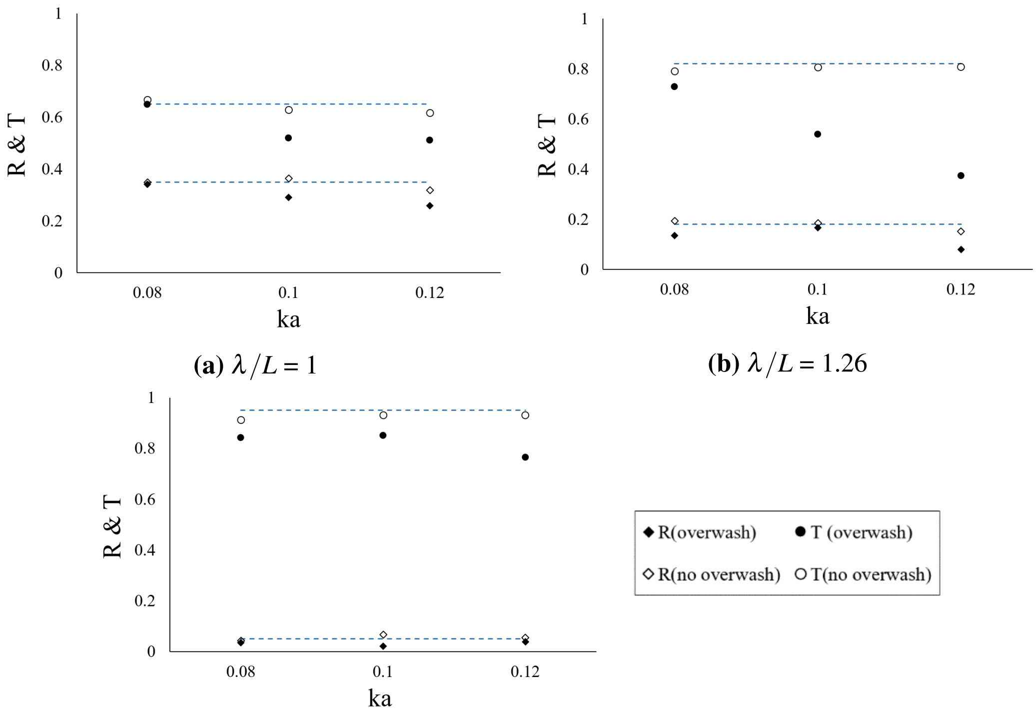

(a) $\lambda/L = 1$

(b) $\lambda/L = 1.26$

(c) $\lambda/L = 1.56$

Figure 4-10: R & T with and without overwash; dashed lines show the analytical solutions of Nelli et al. [21]

4.3.4 Ice deformation

The Young's modulus of floe model was varied to study the influence of ice elasticity on the wave-ice interaction. The E values were selected according to a handful of experimental measurements. As Skene et al. [22] introduced, the E value close to a real sea ice floe is similar to that of a PVC material used by them, E_1 = 500 MPa. Apart from this, considering the highly regional and annual variance of sea ice, a range of E values are also tested: E_2 = 870 MPa, a PP material used by Sree et al. [20]; E_3 = 1.6 GPa, another PP material used by Skene et al. [22]; E_4 = 4 GPa, fresh-water ice used by Dolatshah et al. [59], which is semi-rigid. Noting that these E values were measured on materials applied in model scale, they should be scaled when considered in full scale. The wave and ice dimensions of Case 4 in Table 4-1 were selected to carry out the tests, without edge barriers. This set of wave-ice dimensions is selected because notable overwash was observed, thus the tests can be as close to a realistic situation as possible.

(a) E = 4 GPa

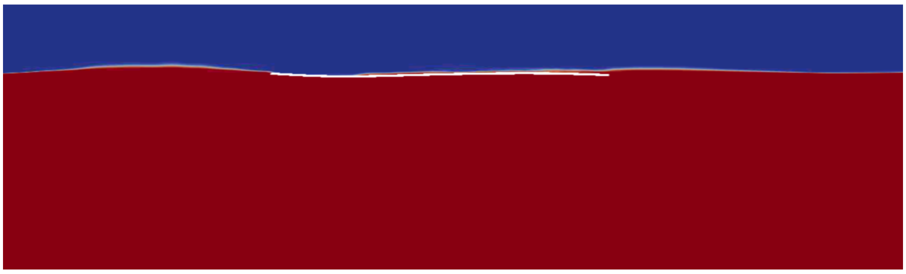

(b) E = 500 MPa

Figure 4-11: Comparison of simulations between wave interactions with semi-rigid and elastic ice.

Simulations were conducted using different E values and show evident differences in the results. Figure 4-11 provides a qualitative comparison between the wave interactions with semi-rigid and elastic ice. When the ice is semi-rigid, it mostly conducts a pitch motion induced by the incident waves; by contrast, when the ice is elastic, it tends to deform into the wave shape, fluctuating along with the surface wave. The latter agrees with the observation of Meylan et al. [57]. The R & T and mean overwash depth obtained with various E are listed in Table 4-4. It shows a clear trend that increasing E can produce lower T and higher R. Here, T is the most significant parameter for polar science, as it denotes how much of the incident wave energy can pass through the floe; it can then derive the attenuation of ocean waves in a multiple floes environment, determining how far the waves can propagate as well as potential additional shrinkage of continuous ice coverage broken by waves. The results show the waves will transmit better when the ice is more elastic; when a realistic sea ice elasticity is considered, it passes about 5% more of the incident wave energy than that when the ice is assumed as semi-rigid. This can be attributed to the behaviour that the elastic ice floe complies with the surface waves, as present in Figure 4-11b, thus the wave feels less obstacle. R is slighter increased with an increased E, showing a more rigid floe will induce more reflection. The increase of R is much less than the decrease of T, so there is more energy dissipated with an increased E. In addition, the overwash depth is found to increase with a more rigid ice; the change in overwash depth is very small (around 0.1 mm, 1% of the ice thickness) compared with the ice scale, thus the additional energy loss is unlikely due to overwash. It is thereby inferred that the additional energy dissipation is due to increased vortical flows induced by a more rigid plate hitting the surrounding water.

Table 4-4: Variation of R, T and Mean Overwash Depth with Different E

E	500 MPa	870 MPa	1.6 GPa	4 GPa
T	0.821	0.815	0.802	0.778
R	0.097	0.106	0.109	0.112
Overwash depth (mm)	4.52	4.57	4.62	4.65

4.4 Conclusions

A multiphase FSI approach has been developed based upon the work of Tukovic et al. [118], which provided an all-in-one hydroelastic solver under the framework of OpenFOAM. Based on the new solver, full coupling has been achieved between the solutions of wave field and ice deformation, and a complete model has been presented simulating the hydroelasticity of sea ice in waves.

Following validation against experiments, the model showed the ability to provide accurate prediction for the case, including wave transmission & reflection, ice deformation, and overwash. In particular, it was demonstrated that overwash can dissipate the wave propagation significantly and its exclusion is the reason for the inaccuracies in contemporary analytical models. This signifies the potential of applying the present new method to enhance relevant wave-ice modelling. The developed computational tool can be used to further investigate wave-ice hydroelastic interactions considering more wave conditions, ice dimensions and ice rhologies. It can also be applied to simulate the behaviour other deformable marine structures in waves.

The sea ice material in this work is assumed to be elastic, while the properties of real sea ice are more complex. Sea ice has been found to present viscoelasticity (strain rate dependent on loading time) and can only be simplified as elastic for short loading events; the actual strain rate of sea ice tends to decrease with a continuous wave load [134]. Furthermore, the viscous and elastic parameters of the sea ice material property have been found to vary significantly for ice samples collected from different regions [58]. Whilst most contemporary modelling works including the present one still consider sea ice as elastic, the proposed FSI solver allows a switch of the CSM solution from elastic to viscoelastic, thus would be able to study the viscoelastic ice behaviour in waves; this is suggested to be worthwhile future research. In addition, sea ice has a maximum stress limit for fracture [135]. It would be of interest to analyse the CSM solution within different ice sheets subjected to different wave conditions, and compare the maximum stress with the ice fracture limit to investigate whether a piece of ice would break up in a given wave condition.

In the next chapter, a computational model will be built to simulate a ship advancing between two ice sheets that are similar to those studied in this chapter, in which, the ship performance is expected to be influenced by the ice-induced reflection of the vessel-generated wave. As an analysis in this chapter has found that changing the ice elasticity from semi-rigid to realistically-elastic has little influence on the wave reflection, the model in the next chapter will consider the ice sheets as rigid to study the ship performance in the channel, which can significantly save computational costs.

Chapter 5

Ship operating in an open-water ice channel

This chapter presents work developing a computational approach to simulate a ship operating in an open-water ice channel and analyse the associated ship-wave-ice interaction. The work demonstrates why the ship resistance is changed by the presence of ice sheets on the sides, and then it ascertains the relationship of the resistance change with the ship speed, the channel width, and the ice thickness.

5.1 Computational modelling

5.1.1 Hull model

A modern container ship model, KRISO Container Ship (KCS), was adopted as the hull model for this study, since such open-water cargo vessels are expected to be the primary vessel type to operate in the future Arctic. The length of KCS is designed to be 230 m at full scale, while this hull does not have a full-scale ship existing in real life. Nonetheless, KCS is a container ship model that has been widely applied in computational simulations and model tests, and its geometry with appendages is

A version of this chapter has been published as: Huang, L., Li, M., Romu, T., Dolatshah, A. and Thomas, G. 2020. Simulation of a ship operating in an open-water ice channel. *Ships and Offshore Structures*, pp.1-10.

openly accessible [136]. A scaled model by a ratio of 1:52.667 is commonly used in relevant studies, e.g. [23]; therefore, this study applies the same model-scale KCS hull to enable easy comparisons by other researchers.

Table 5-1: Main Dimensions of the KCS Hull

	Model scale	**Full scale**
Length between perpendiculars (L_{pp})	4.367 m	230.0 m
Beam at waterline (B)	0.611 m	32.2 m
Draught at midship (T_M)	0.205 m	10.8 m
Trim angle	0.0	0.0
Block coefficient	0.651	0.651
Wetted surface	3.397 m^2	9424.0 m^2

5.1.2 Boundary conditions

A three-dimensional computational domain was established using the STAR-CCM+ software, as illustrated in Figure 5-1. It is defined by the earth-fixed Cartesian coordinate system $O-xyz$; the (x,y) plane is parallel to the horizon, and the z-axis is positive upwards. The lower part of the domain is filled with water and the remainder is filled with air. The model-scale KCS hull is fixed across the waterline according to its design draught. On each side of the ship, an ice sheet is placed at a distance ($2/W$, where W denotes the channel width) from the ship central line, with 90% of ice thickness (h) immersed in water (assuming ice density equals to 900 kg/m^3). The water was initialised as flowing with a uniform velocity (U_{water}) against the bow of the hull, and a constant velocity condition is applied to the inlet boundary to maintain a stable water flow entering the domain. The same initial and boundary velocity was also applied to the ice surfaces. Thus, a relative velocity exists between the ship and water/ice, where U_{water} indicates the advancing speed of the ship in an ice channel with calm water (U). The ship speed can be converted to Froude number $Fr = U/\sqrt{g \times L_{pp}}$. The ship surface is defined as a non-slip wall, and a hydrostatic pressure condition is applied to the outlet, with the zero-gradient condition applied to other boundaries. The water depth was set to be twice of the ship length to eliminate any seabed effect.

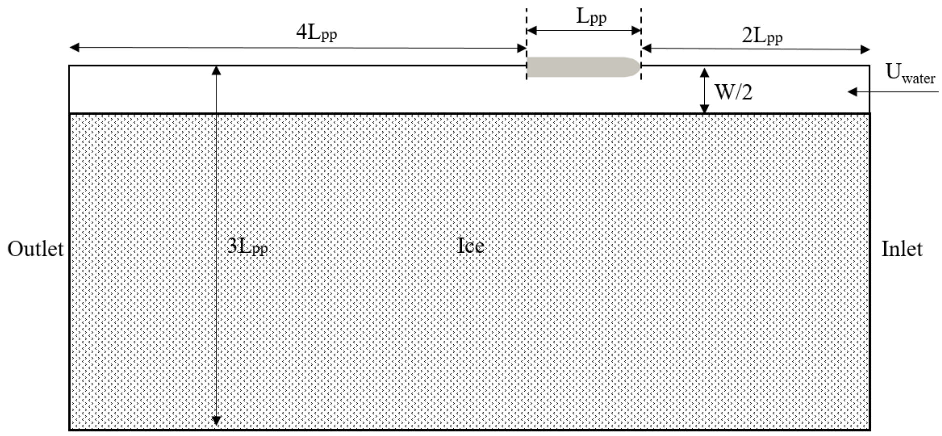

(a) Plan view

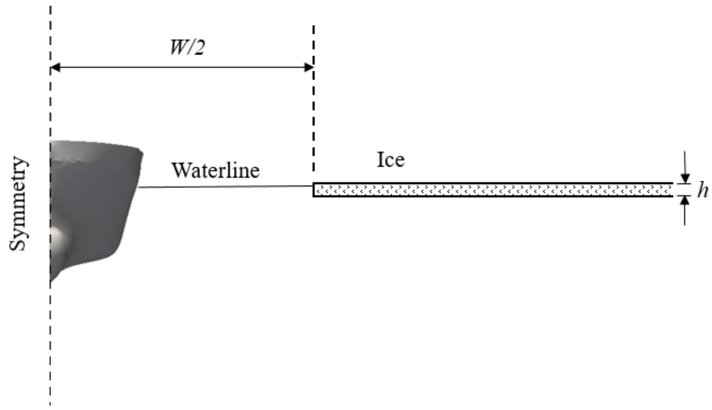

(b) Section view

Figure 5-1: Sketch of the computational domain with dimensions (only one ice sheet is shown)

5.1.3 Discretisation

The fluid solutions were obtained by solving the RANS equations together with the VOF method, as introduced in Section 2.1.2 and 2.1.3, and the SST $k-\omega$ model

[137] was adopted to account for turbulent effects. The SST $k-\omega$ has been demonstrated to be a robust turbulence modelling strategy due to its capability to model adverse pressure gradients and flow separation [137]. An adverse pressure gradient means the static pressure increases in the direction of the flow, which can happen when a water flow encounters a hull, especially around the stern region [138].

For solving the equations based on the FVM discretisation [121], the computational domain was divided into a mesh consisting of hexahedral cells, and local mesh refinements were applied at the free-surface area and around the ship and ice sheets, as shown in Figure 5-2, resulting in a cell number of around 10.8 million. Five layers of cells are applied at the ship and ice surfaces so that the boundary layer can be properly solved. The size of timestep was determined at 0.01 second in this study, according to Courant number less than one (Equation 3.1). Both the mesh and timestep resolutions were justified through verification studies presented in the next section.

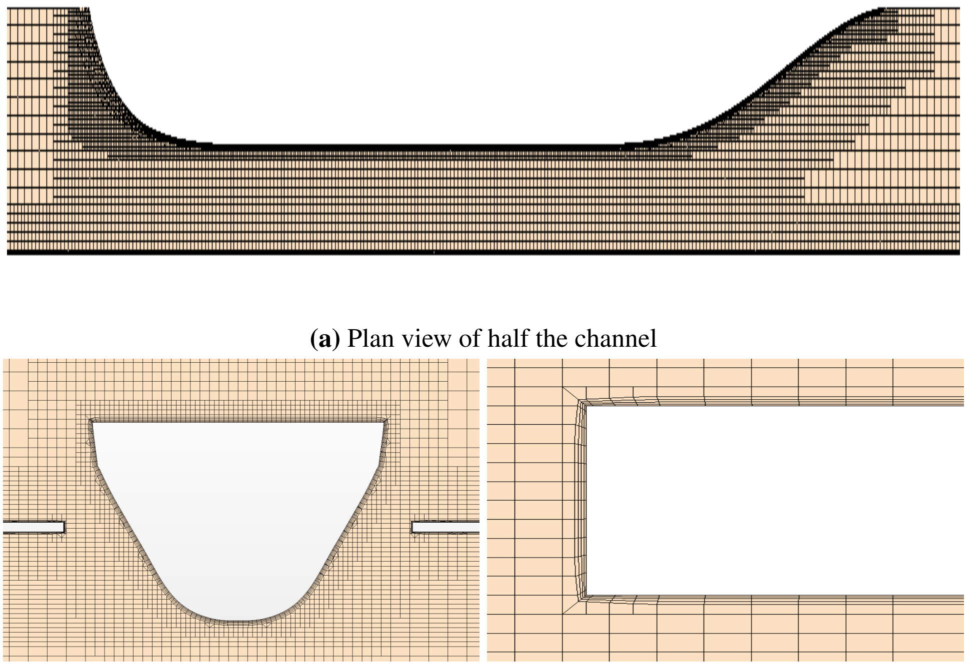

(a) Plan view of half the channel

(b) Section view **(c)** Close-up section view at the ice edge

Figure 5-2: Mesh layout of the model

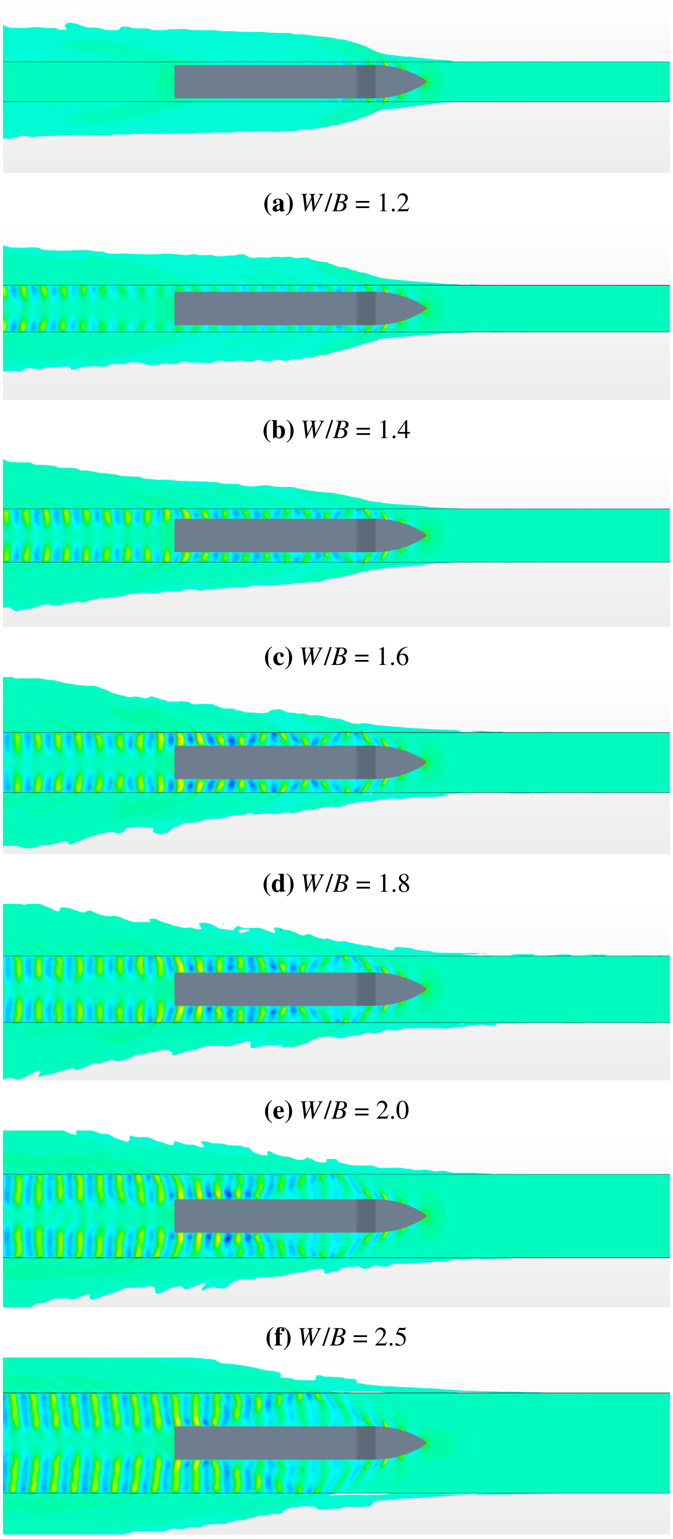

(a) $W/B = 1.2$

(b) $W/B = 1.4$

(c) $W/B = 1.6$

(d) $W/B = 1.8$

(e) $W/B = 2.0$

(f) $W/B = 2.5$

(g) $W/B = 3$

Figure 5-3: Wave patterns in ice channels of different channel widths, obtained when $Fr = 0.12$ and $h/T_M = 0.1$

5.2 Results and discussion

When a ship is advancing in an open-water ice channel, it generates waves which can be reflected due to the presence of ice, as shown in Figure 5-3; when the channel width, relative to the ship beam (W/B), changes, the wave pattern evolves accordingly. In addition, certain wake is observed flowing on top of the ice, known as overwash. The changed flow leads to different ship hydrodynamics compared to the open-water case. It can be seen that when $W/B > 2.5$, the channel barely influences the wave pattern; when $W/B < 2.5$, varying the channel width presented different wave patterns and the ship resistance also changed by different degree. When the channel has little influence on the wave pattern, the computational ship resistance agrees well with the corresponding experimental data of open-water resistance, as presented in Figure 5-4. Additional hydrodynamic details of the KCS hull is demonstrated in Figure 5-5.

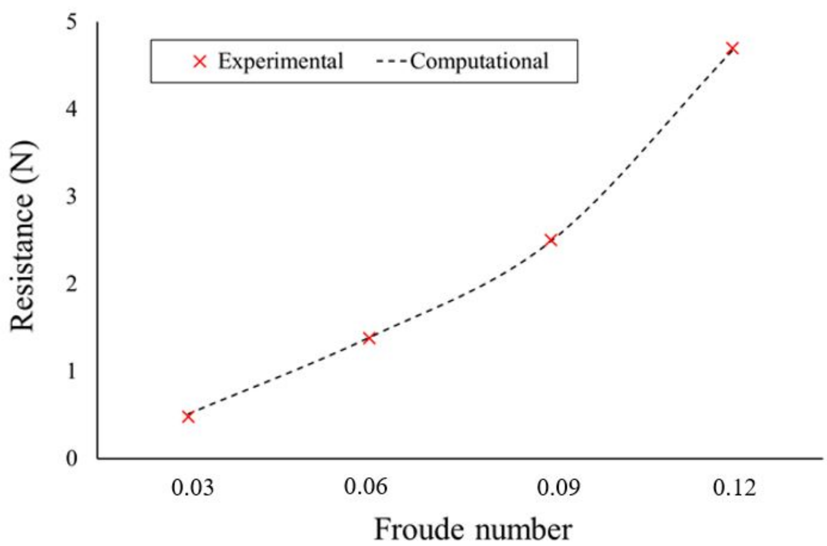

Figure 5-4: Computational resistance of the model-scale KCS in an ice channel of $W/B > 2.5$, compared with experimental resistance of the model-scale KCS in open water [23]

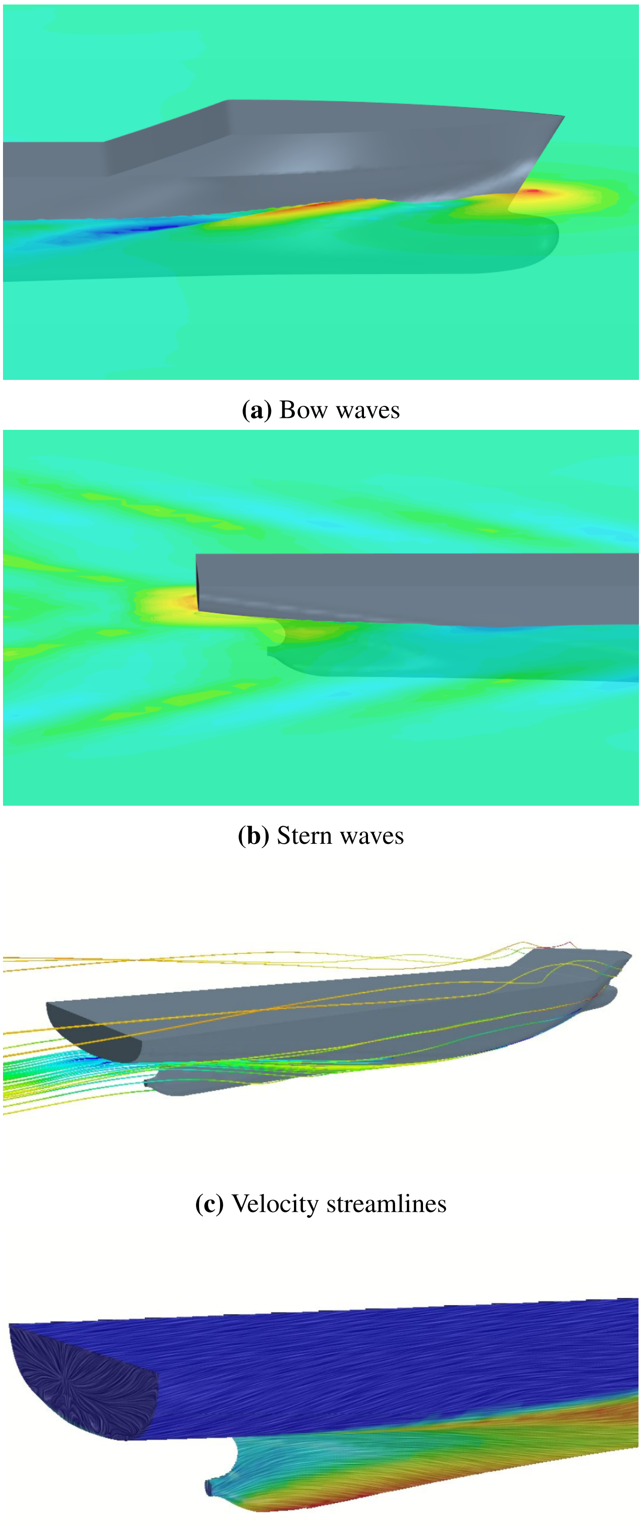

(a) Bow waves

(b) Stern waves

(c) Velocity streamlines

(d) Skin friction lines

Figure 5-5: CFD illustration of the KCS hydrodyanmcis ($Fr = 0.18$)

5.2.1 Verification

There is a lack of experimental data for the exact ice channel scenario, therefore extensive verification was conducted to justify the proposed approach and select suitable discretisation resolutions that provide convergent solutions for the wave pattern as well as the ship resistance. Numerical verifications in hydrodynamics usually only examine integral quantities (e.g. ship resistance), while Phillips and Roy [139] proposed a procedure of verifying local quantities (e.g. free surface elevation). This inspired the present work to include a verification study on the free surface between the ice sheets, since the ice-affected wake is a key feature of the present problem and governs the associated hydrodynamics. According to the standard verification procedure of ITTC [140], a representative case is first adopted, and then simulations are performed for the same case with different levels of temporal and spatial discretisation. The representative case selected in the current work is: $W/B = 1.2$, $h/T_M = 0.1$, and $Fr = 0.03$. This case is for the slowest speed examined, combined with a channel whose width and ice thickness are able to produce significant wave reflections. The representative case is found to be the most challenging in the present study; in other words, this case requires the highest numerical accuracy so its verification can be reasonably adapted to other simulation conditions.

Based on the representative case, the timestep and mesh sizes were systematically varied, resulting in four sets of resolutions for temporal and spatial respectively, listed in Table 5-2 as Tests 1-7, alongside their corresponding resistance results. With different timestep sizes, the resistance is shown to be insensitive despite the simulation gets divergent when the timestep size is increased to 0.028 s. On the other hand, the resistance shows a monotonic convergence [141] with the tested mesh densities; it gradually approaches a certain value and the variance is not significant when the cell number is larger than 10.8 Million.

Another verification was performed for the free surface in the channel. Figure 5-6 presents the obtained free surface of the tests in Table 5-2. Comparing Figure 5-6a, 5-6b and 5-6c it is worth noting that the larger timestep sizes (Test 2 and 3) produce oscillating free surfaces even in front of the ship, which is unrealistic and suggests the boundary conditions cannot be precisely implemented with the applied resolutions. However, the resistance values of Test 1-3 are similar, as reported in Table 5-2. This confirms the importance of verifying free surface; even if integral quantities (resistance) achieve convergent, localised divergences can still exist. In this channel case, it is particularly related to the demanding requirement of solving the small clearance between the ship and ice. Figure 5-6a, 5-6d and 5-6e reveal the mesh convergence aligned with the resistance results, and Figure 5-6f shows inferior free surfaces due to the bad mesh quality. Based on the sensitivity studies on both resistance and free surface, the resolution of Test 1 is selected to perform further simulations.

Table 5-2: Ship Resistance with Different Discretisation Resolutions

Test number	Timestep size (s)	Cell number	Resistance (N)
1	0.01	10.8 Million	0.514
2	0.014	10.8 Million	0.512
3	0.02	10.8 Million	0.505
4	0.028	10.8 Million	divergent
5	0.01	14.9 Million	0.524
6	0.01	7.6 Million	0.485
7	0.01	5.4 Million	0.414

5.2.2 Analyses on the ship resistance with ice

A series of simulations were conducted to predict the ship resistance in an open-water ice channel and determine how it is influenced by ship speed, channel width and ice thickness. Figure 5-7 presents the ship resistance in channel ($R_{channel}$) for different ship speeds and channel widths, which is compared with corresponding open water resistance measured at same speed without any ice (R_{ow}) to distinguish the channel effect, including two subfigures respectively showing the absolute

(a) Test 1

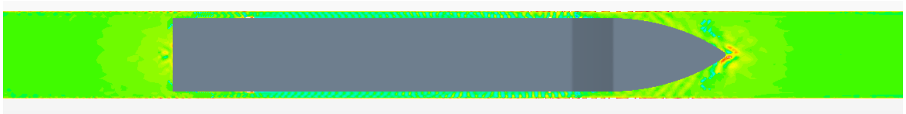

(b) Test 2

(c) Test 3

(d) Test 5

(e) Test 6

(f) Test 7

Figure 5-6: Free surface obtained with different discretisation resolutions

change ($R_{channel} - R_{ow}$) and relative change ($R_{channel}/R_{ow}$). Overall, the resistance increases with a decreased channel width. In accordance with the changing of wave pattern, the presence of the channel influences the ship resistance when $W/B < 2.5$, which is in line with practice as an icebreaker normally cannot create a channel wider than this range. On the other hand, this limit is much lower than that of a canal case [142, 143], as the ice is of limited thickness and the water is not shallow.

Figure 5-7a shows the absolute resistance increment is greater for a larger ship speed, which is line with a greater wave reflection occurring with a higher ship speed. In contrast, Figure 5-7b illustrates that the relative resistance increment is larger for the low-velocity condition (Fr = 0.03), indicating the channel effect is more influential when the ship is operating slowly, which was also observed in the experiments of Leiviska et al. [100] and Heinonen [101]. It means that, with increasing ship speed, the channel-added resistance increases more slowly than the basic open-water resistance, thus the relative change becomes smaller. This characteristic can be important, since ships usually operate slowly in such ice channels. The relative resistance increment is observed to be up to 15%. This limit is likely to increase with a slower ship, but the operation would be too slow to be of interest.

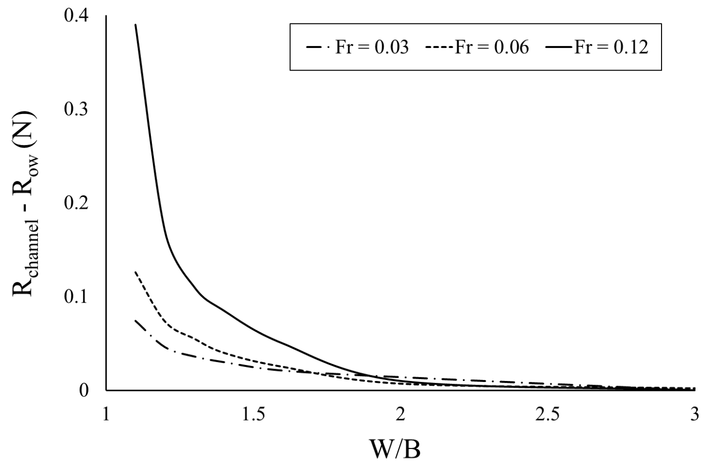

(a) Absolute difference

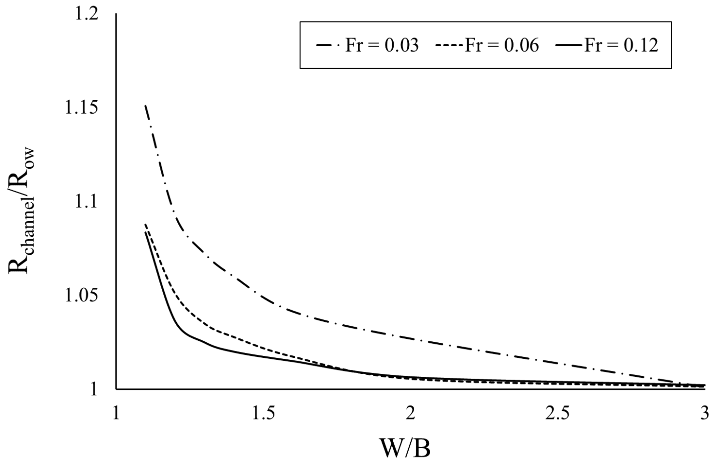

(b) Relative difference

Figure 5-7: Ship resistance in ice channels of different widths, in comparison with the simulation without ice, obtained when $h/T_M = 0.5$

To analyse the reason for the resistance changes, pressure and shear components of the resistance are shown in Table 5-3. It shows that the resistance change is mainly attributed to the pressure component. Such significant increases of pressure resistance correlate with the evidently changed wave patterns, as presented in Figure

5-3. In contrast, the shear component slightly increases only when the channel is very narrow ($W/B < 1.3$), which is because the water speed increases when the channel space is sufficiently small, thus increasing the friction associated with the boundary layer effect. Although the pressure component can have a significant increment, the overall resistance increases by a smaller extent, which is because the pressure component occupies a relatively small proportion in the total resistance.

Table 5-3: Ship Resistance in Ice Channels of Different Widths (W/B), alongside Breakdown into Pressure and Shear Components and Increased Percentage Compared with in Open-water, Obtained when $Fr = 0.03$ and $h/T_M = 0.5$

W/B	Total resistance	Pressure component	Shear component
1.1	0.557 (+15%)	0.149 (+46%)	0.408 (+8%)
1.2	0.529 (+9%)	0.141 (+38%)	0.388 (+2%)
1.3	0.519 (+7%)	0.136 (+33%)	0.383 (+1%)
1.4	0.513 (+6%)	0.132 (+29%)	0.381 (+0%)
1.6	0.504 (+4%)	0.123 (+20%)	0.381 (+0%)
1.8	0.499 (+3%)	0.118 (+15%)	0.381 (+0%)
2	0.497 (+2%)	0.116 (+12%)	0.381 (+0%)
2.5	0.483 (+0%)	0.102 (+0%)	0.381 (+0%)
3	0.483 (+0%)	0.102 (+0%)	0.381 (+0%)

The influence of ice thickness on $R_{channel}$ was studied by varying h while keeping the other parameters constant. Figure 5-8 shows $R_{channel}/R_{ow}$ with different ice thicknesses non-dimensionalised by the ship draught (h/T_M). It can be seen that as the ice thickness increases, so the ship resistance increases. This is due to the larger submerge of thicker ice reflecting deeper into the wave; also, as the ice thickness increases, there is less overwashing radiation so more surface waves are reflected, as shown in Figure 5-9. The results are almost the same when $h/T_M > 0.15$, suggesting that the ship-generated wave is sufficiently reflected in this range, so further increasing h does not make a difference. Whereas $R_{channel}/R_{ow}$ is close to unity when $h/T_M < 0.05$, which means that in this range the ice is too thin to influence the ship resistance. Within the range of $0.05 < h/T_M < 0.15$, the resistance increases with increasing ice thickness. In practice, the ice thickness of ice channels in Baltic

Sea is usually between 0.6 $\sim$ 1 meter [144], corresponding to $h/T_M = 0.06 \sim 0.1$ in this study, and yet in the Arctic the ice is usually thicker; therefore, in a real ice channel the ice will likely be thick enough to induce effective wave reflections and alter the ship resistance, and this lays in a range where the channel effect positively correlates with ice thickness.

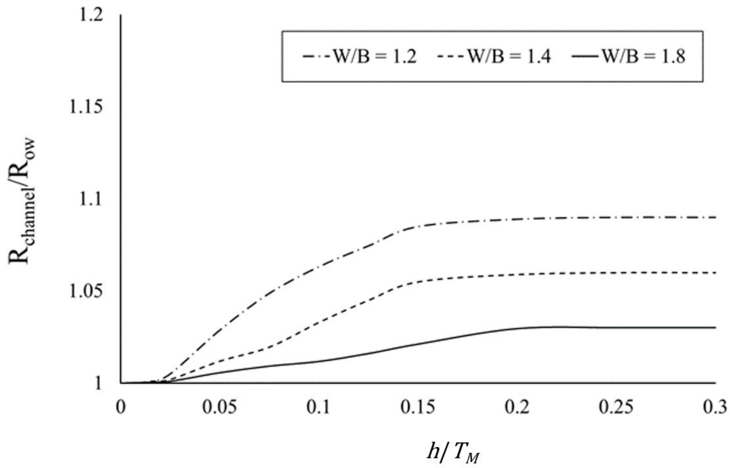

Figure 5-8: Ship resistance in ice channels of different ice thicknesses, in comparison with the simulation without ice, obtained when $Fr = 0.03$

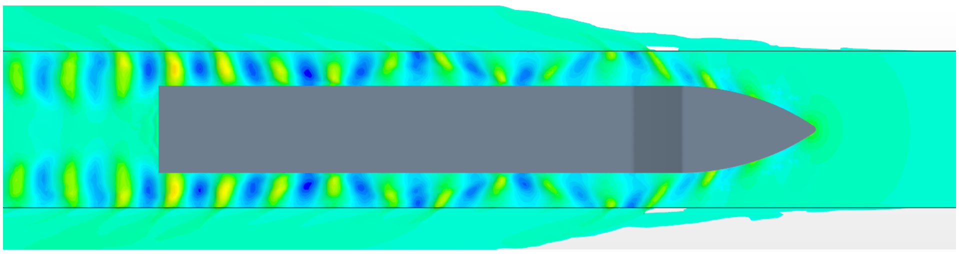

(a) $h/T = 0.1$; ice is relatively thin and overwash happens

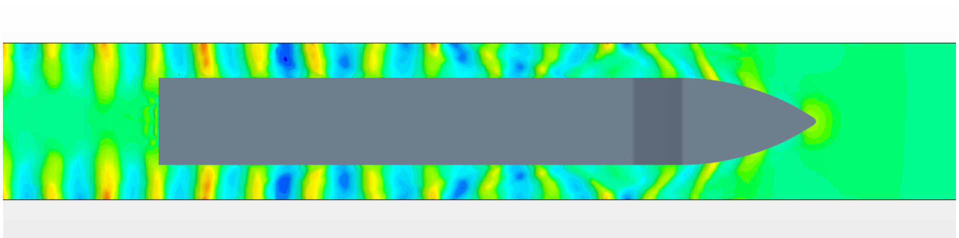

(b) $h/T = 0.3$; thick ice prevents overwash and wave reflection is stronger than that in the above panel

Figure 5-9: Wave patterns in ice channels of different ice thicknesses, obtained when $Fr = 0.12$ and $W/B = 1.8$

5.3 Conclusions

In this chapter, a CFD method has been applied to model the advancement of a ship in an open-water ice channel. With the flexibility of the simulation approach, environmental and operational parameters such as ice dimensions were subtly varied to investigate their influences on the ship-wave-ice interaction. The strong visualising capability of CFD allows the breakdown of ship resistance into pressure and shear component, as well as showing the corresponding change in wave pattern. These have allowed the acquirement of novel insights into the problem.

Based on a series of simulations, an open-water ice channel has shown to increase the ship resistance, and the increment is mainly attributed in the pressure component, caused by changes of wave pattern due to the presence of the ice sheets. For the investigated container ship form, the channel can increase the ship's resistance by up to 15% of that in a pure open-water condition. The channel effect was found evident when its width is less than 2.5 times the ship beam and the ice thickness is larger than 5% of the ship draught; both the effective ranges are aligned to a practical ice channel, which indicates that the channel effect is influential for such ship operations in real life.

Ice channels are created to help commercial ships navigate through level ice, while the melting of Arctic sea ice has already presented a widespread transformation of level ice into ice floe fields, which is directly navigable for commercial ships without icebreaking capabilities. In the next chapter, a computational model will be built to simulate the operation of a ship in such ice floe fields and provide insights into that emerging scenario.

Chapter 6

Ship operating in floating ice floes

In this chapter, a computational approach is established combining CFD with the Discrete Element Method (DEM) to replicate the ship operation in floating ice floes and assess the ice-added resistance. In addition, two algorithms are developed to implement the model with natural ice-floe fields, which successfully equips the CFD-DEM simulation with realistic floe size and location distributions. Based on the developed approach, vast simulations are performed to investigate how the resistance is influenced by ship speed, ship beam, ice concentration, ice thickness and floe diameter.

6.1 Computational modelling

In order to simulate a ship advancing in floating ice floes, this work followed three steps to build a computational model: (a) CFD, a standard model of ship advancement in open water, where fluid solutions are obtained, including the wake and water resistance of a ship. (b) DEM, for modelling ice floes and their collisions with the ship and nearby floes; those floes obtain fluid force from the CFD solution so that the ship-wave-ice coupling is achieved. (c) floe-distribution algorithms, by which natural ice-floe fields are generated and implemented into the CFD+DEM

A version of this chapter has been published as: Huang, L., Tuhkuri, J., Igrec, B., Li, M., Stagonas, D., Toffoli, A., Cardiff, P. and Thomas, G., 2020. Ship resistance when operating in floating ice floes: a combined CFD&DEM approach. *Marine Structures*, 74, 102817.

model. Steps (a) and (b) were performed based upon the STAR-CCM+ software, and Step (c) was realised using MATLAB scripts.

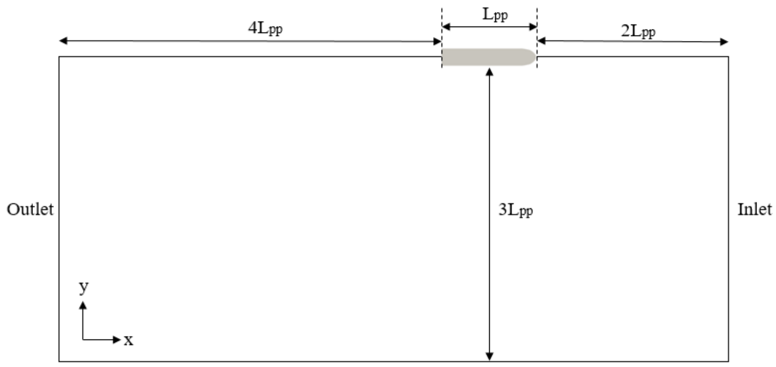

(a) Plan view: only half of the domain is shown but no symmetry plane condition is applied

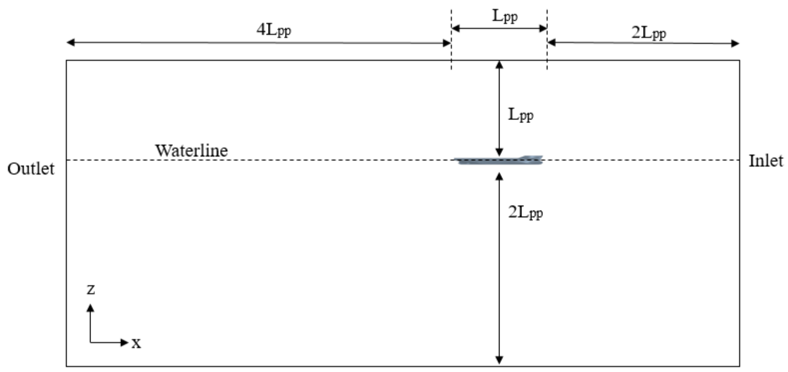

(b) Profile view

Figure 6-1: Illustration of the computational domain with dimensions

6.1.1 Ship flow

An open-ocean fluid domain was built with the recommended domain size and boundary conditions, as shown in Figure 6-1. The computational domain is three-dimensional, defined by the earth-fixed Cartesian coordinate system $O-xyz$. The (x,y) plane is parallel to the horizon, and the z-axis is positive upwards. Following the guidelines of the International Towing Tank Conference (ITTC) [138], the domain size is sufficiently large to avoid the ship-generated waves being reflected from the boundaries. The lower part of the domain is filled with water and the remainder is filled with air. The model-scale KCS hull, as introduced in Section 5.1.1, is fixed at the free surface according to its design draught and the hull surface is modelled as a no-slip wall. The water was initialised as flowing with a constant velocity (U_{water}) against the bow of the hull, and a constant velocity condition was applied to the inlet boundary to maintain a stable water flow entering the domain. Thus, a relative velocity exists between the ship and water, where U_{water} indicates the advancing speed of the ship in calm water. A hydrostatic pressure condition is applied to the outlet, and the zero-gradient condition is applied to other boundaries.

The fluid domain is governed by the RANS equations together with the VOF method, as introduced in Section 2.1.2 and 2.1.3, and the SST $k-\omega$ model [145] is adopted to account for turbulent effects. The fluid solutions are solved by the FVM method [121]. Figure 6-2 displays the mesh layout generated for solving the open-water ship flow, in which high resolutions are applied to the regions where ship-wave-ice interactions are expected to happen. The mesh density around the hull uses the optimised density verified in Chapter 5, which achieved the accurate prediction of open-water resistance with minimal cells; this results in a total cell number of around three million for the open-ocean ship flow domain.

6.1.2 Discrete ice floes

Importing the ice floes is achieved by a novel array-injection method. The simulation first runs for a certain time without sea ice to allow the fluid domain to achieve a steady-state, i.e. when the ship wake has become stable. Subsequently, an array of ice floes is injected into the computational domain near the inlet boundary, as portrayed in Figure 6-3a. The ice floes are initialised to have the same velocity as the water flow ($U_{ice} = U_{water}$), and one ice floe array is injected to the same region every $t_{inject} = L_{array}/U_{ice}$, so that the next ice floe array can just follow the former one, as shown in Figure 6-3b. Thus, the injection of ice floes does not influence the stability of solutions around the ship, and the ship can keep advancing in a continuous ice-floe zone, as desired, shown in Figure 6-4. With this method, an ice-floe route of unlimited length can be achieved without the need for a very long domain, which significantly saves computational costs.

The ice floes are modelled as DEM elements in the Lagrangian framework moving

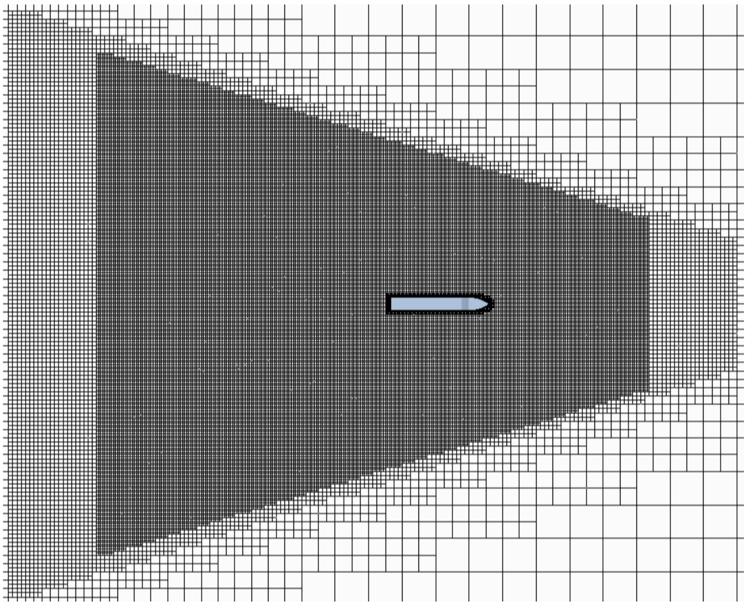

(a) Plan view

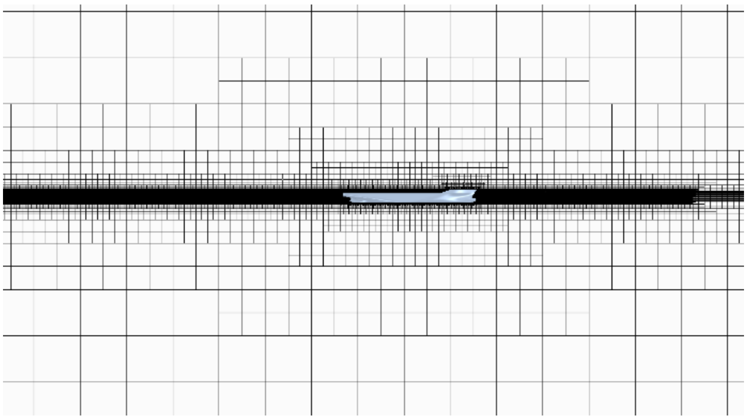

(b) Profile view

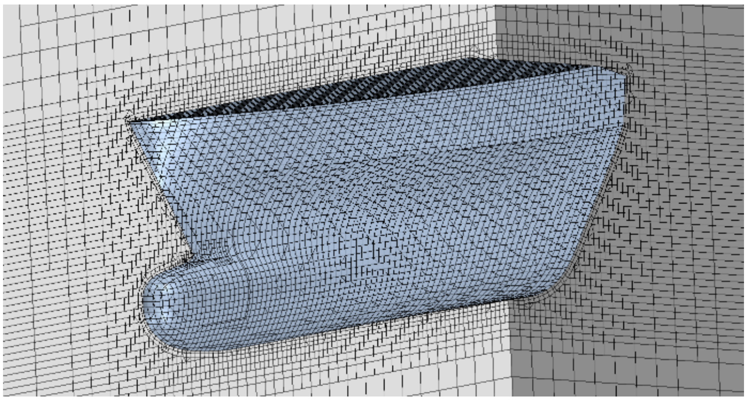

(c) Isometric view of bow region

Figure 6-2: Mesh layout of the model, in which local refinements are applied at the Kelvin-wave region, the free surface region and around the hull geometry

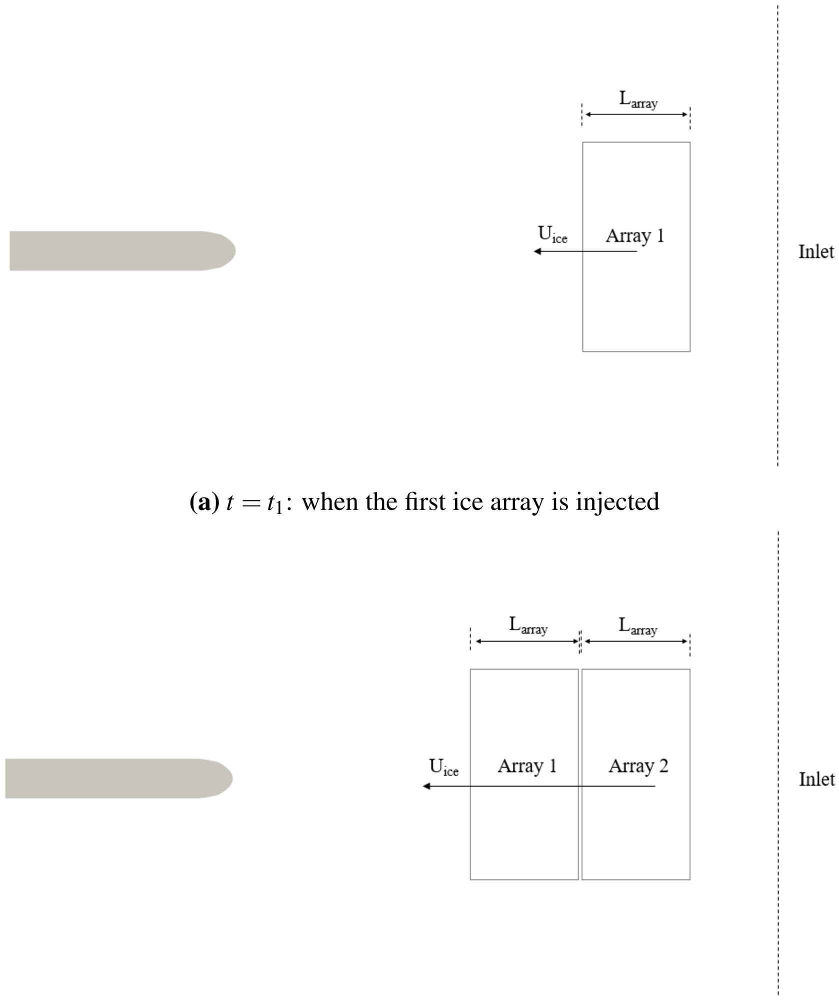

(a) $t = t_1$: when the first ice array is injected

(b) $t = t_1 + t_{inject}$: when the second ice array is injected

Figure 6-3: Illustration of how ice floes are imported

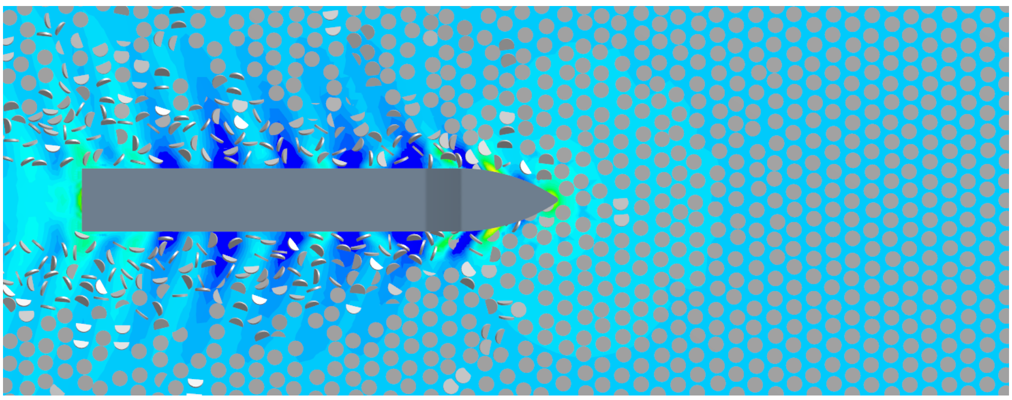

Figure 6-4: Simulation view of a ship advancing in a regular ice floe field

in the Eulerian CFD domain [146]. Each ice floe is modelled as a rigid thin disk, as in the present problem floes are supposedly pushed away by the ship rather than deformed or fractured, as demonstrated by Polojärvi et al. [147]. The density of ice is set at $\rho_{ice} = 900kg/m^3$, while ice diameter D and thickness h are variable. The movement of an ice floe can be considered as the combination of translation and rotation, which was solved with the rigid-body motion equations in the body-fixed system based on the mass centre of the floe, as expressed in Equation 2.18 and 2.19.

The total force and torque of each floe is governed by the gravity, the hydraulic load from the surrounding fluid $\mathbf{F_h}$ (Equation 2.17), and the contact force from ship-ice contact and ice-ice contact $\mathbf{F_c}$ (Equation 2.26 and 2.27). Thereinto, $\mathbf{F_h}$ of each DEM ice floe is obtained by projecting the floe into the fluid mesh, so that the cells around the disk structure are partially blocked by the disk volume and fluid solutions are interpolated on the disk surface, i.e. the fluid solution is integrated over the surface of each ice floe to contribute the total force and torque. Therefore, the cells around the free-surface area should be small enough to capture the floe geometry; based on the verification in Chapter 3 on the mesh density around a circular ice floe, at least 4 cells per ice thickness is applied in this model. The timestep size used in CFD is 0.01 second so that the Courant number is less than one (Equation 3.1), while each CFD timestep is split into 1000 DEM sub-timesteps so that the collisions can be sufficiently solved, which shows DEM dominates the time requested for the CFD+DEM computation.

The CFD+DEM is a one-way coupling mechanism, i.e. the ice movement does not provide feedback to the fluid domain thus the wave radiation is not influenced by floes. Two-way coupling is not chosen here since it would induce much higher computational costs. Also, the wave radiation mainly influences the floes moving away from the ship, so it is deemed to have little influence on the ship performance, as far as the ice concentration is not high enough to produce a considerable wave reflection. The validation in Section 6.2.1 shows the one-way mechanism can accurately predict the resistance when ice concentration is up to 70%. In addition, Mucha [148] and Luo et al. [98] compared one-way and two-way CFD+DEM simulations for ship, wave and brash ice interactions; both studies reported that using either of the coupling schemes does not make a notable difference on the predicted ship resistance.

6.1.3 Floe-distribution algorithms

The ice-floe array initialises floes to be of uniform size and equidistant to each other, as shown in Figure 6-4, which is not a realistic condition and imposes artificial attributes into the ice load. For example, such setup makes ship-ice contacts always occur at the same locations on the hull, which influences the structural loads and the resistance of the ship. This defect motivates the development of appropriate algorithms to import ice floe fields into computational models, so that the floe size and location in simulations can follow natural conditions observed in polar regions.

There are two principal features for a natural ice floe field: (a) ice floes are a mixture of different sizes, and (b) the location of each ice floe should be randomly distributed. In a sufficiently large region, the floe sizes have been observed to distribute following a log-normal function [110]. As shown in Figure 6-5, the majority of floes tend to have a size close to a medium value; the proportion for larger floes decreases with increased size, and proportion for smaller floes decreases with decreased size. Such a curve is referred to as the curve of Floe-Size-Distribution (FSD). The FSD curve can have regional and seasonal variations, which can be obtained from field and aerial measurements [110, 149].

In this work, two complementary algorithms have been developed to generate natural ice-floe fields that can be implemented into computational models. For both the models, an FSD curve is required as the governing input. Other inputs include the length and width of the model's computational domain, the shape of the floes, and the ice concentration (C), defined as the ice-covered area divided by the total sea-surface area, i.e. area of the domain. For the size of a domain used to study an environmental or engineering problem in ice floe fields, the ice thickness of all floes is not expected to have a significant variation, so the thickness of all floes in one simulation is assumed to be constant; even so, ice thickness can also be set as a

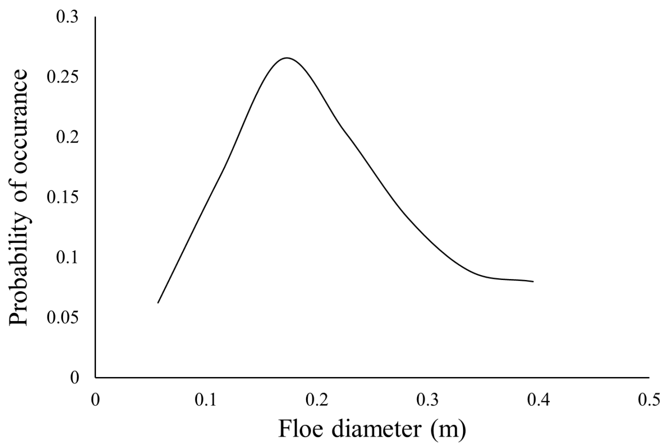

Figure 6-5: FSD measured by Colbourne [24]: ice floes in a sufficiently large region are of a mixture of different sizes and the size against possibility function follows a log-normal form

desired function, if required. The complete condition of generating an ice floe field is that no overlapping occurs between any floes. Upon completion, the output is a matrix listing the x-y coordinates of every ice piece and the corresponding floe size, while z coordinates are aligned to the buoyancy-gravity equilibration of each floe.

Based on the inputs, Algorithm (I) first calculates the number of ice floes and marks them from 1 to n_p, and then it randomly injects all ice floes inside the domain and their initial locations are stored in a location matrix. Subsequently, the algorithm proceeds by considering every piece separately, starting from $i = 1$ to $i = n_p$. The algorithm first checks if overlapping occurs (with other ice pieces and with the boundary of the domain). Where an overlapping occurs, the vicinity of the ice piece is searched to see whether there is a sufficient space for it to move over (horizontal direction vector revolves 360 degrees and searches the space in the vicinity of the original position). If there is sufficient space in the vicinity, the ice floe will be moved there, and the location matrix is updated. If there is insufficient space in the vicinity, the ice piece is then randomly reallocated to another position. The process iterates until all ice pieces are settled and no constraints are violated, depicted in Figure 6-6.

Algorithm (II) is based upon genetic algorithm based upon the Darwin's principle:

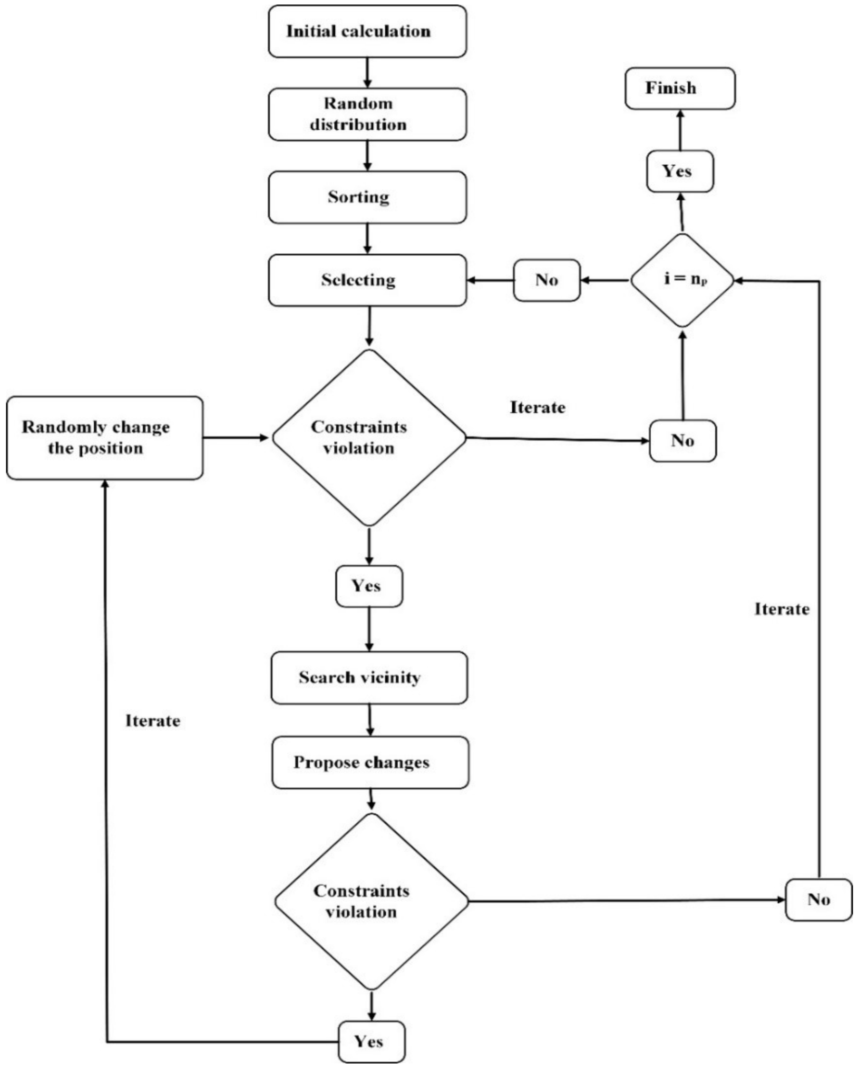

Figure 6-6: Flowchart of Algorithm (I)

the survival of fittest individuals [150]. This algorithm defines a penalty factor to indicate the overlapping between ice floes, where a higher penalty value corresponds to a higher overlapping area, i.e. a targeting penalty factor of zero means no overlapping at all. In other words, the target penalty factor can be set to be larger than zero when certain ice overlapping is allowed, which is suitable for modelling ice herding and rafting [48, 47]. The algorithm starts by producing a certain number (M_0) of parent solutions, corresponding to (M_0) penalty factors. Subsequently, the algorithm selects a small number of solutions (M_1) with the lowest penalty factors, which will be used as parents to produce child distributions. This process mixes and matches the best parts from the (M_1) solutions, yielding the same overall amount of

(M_0) solutions for the next generation. Namely, only fittest individuals survive in each generation, while the rest of them are discarded by the algorithm. Thus, the average of selected solutions is better than the previous ones, leading to a higher probability to get better child solutions. In particular, (M_2) best solutions, known as elite individuals, automatically survive to the next generation without a change; meanwhile, the rest of the solutions ((M_1) – (M_2)) mixes and matches to get ((M_0) – (M_2)) new distributions, which are combined with the elite individuals to form the next parents. This additional step of elite individuals can efficiently speed up the algorithm. The above process is iterated from generation to generation until a solution is found that achieves the targeting penalty factor, as illustrated in Figure 6-7. In this study, M_0 = 2000, M_1 = 1000 and M_2 = 100.

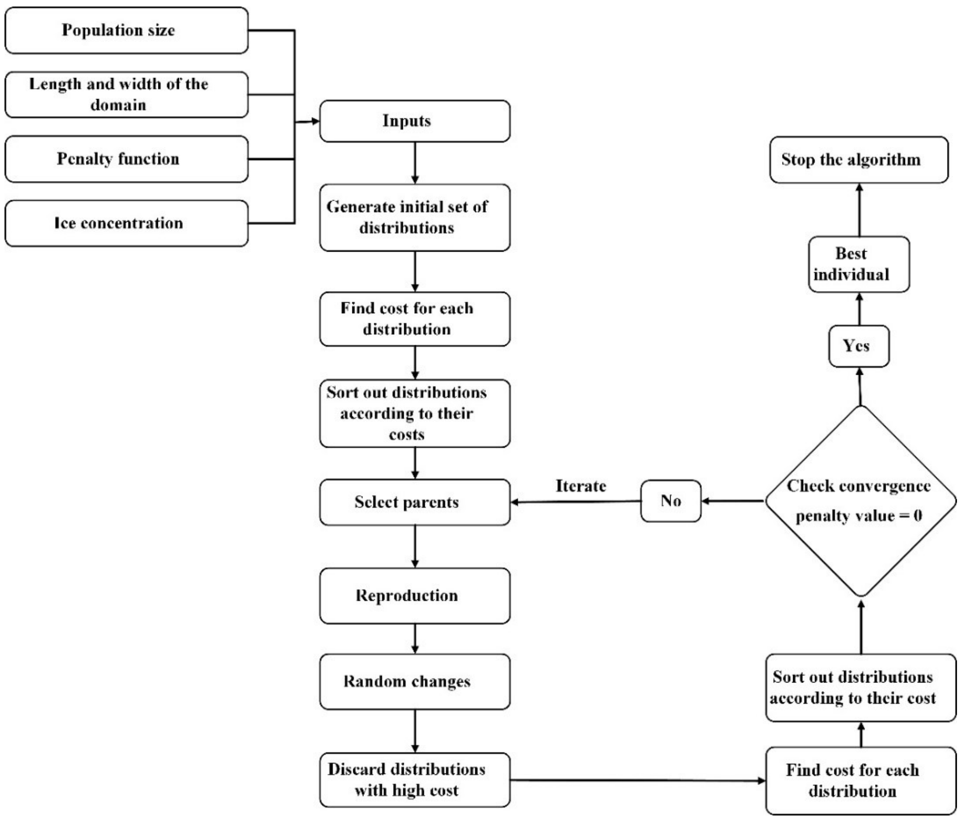

Figure 6-7: Flowchart of Algorithm (II)

Figure 6-8 shows two samples of floe distributions obtained by Algorithm (I) and (II) respectively, in which the targeted FSD and C are exactly achieved. In these samples, the shape of ice floes was set to be circular to model the pancake ice condition. However, both the algorithms are capable of modelling other ice shapes, as far as the shape can be mathematically defined. Comparing the two algorithms, they have no difference in terms of accuracy, as the overlapping constraint is explicitly prescribed. Nonetheless, Algorithm (I) is preferable to be used for a relatively low target C, because a relatively low C means there is abundant open-water area in the domain and thus it is easy for Algorithm (I) to settle all floes into desirable space. Therefore, Algorithm (I) gets slow when producing ice floe fields of a high C. By contrast, the speed of Algorithm (II) is not dictated by C, as it is a mix-and-match approach. Following tests, Algorithm (I) is faster than Algorithm (II) when C is up to 60%. Thus, it is recommended to use Algorithm (I) when C is up to 60% and to use Algorithm (II) when C is larger than 60%.

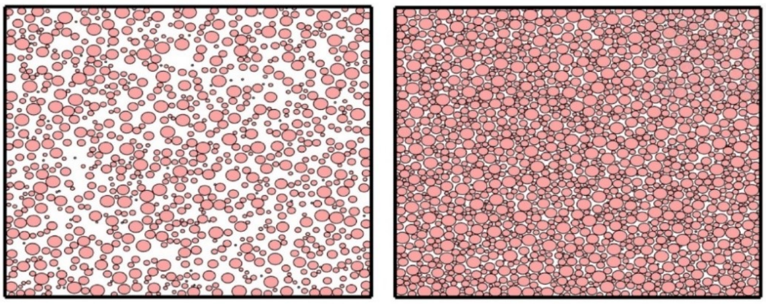

Figure 6-8: Ice-floe fields obtained by Algorithm (I), C = 40% (left side); and by Algorithm (II), C = 70% (right side)

For a specific FSD and C condition, the algorithms can generate the corresponding ice-floe field for a ship to enter, which is used to replace a regular array as in Figure 6-4. Updated simulations are shown in Figure 6-9, in which the artificial regularity of ice load has been avoided. Up till this point, the computational modelling for the present work is completed. Noting that the introduced FSD algorithms are not only compatible with current work, they are also useful for other computational models involving ice floes[1].

[1]The floe-distribution algorithms have been further developed and written up into a paper for introducing and releasing the code: Huang, L., Igrec, B., and Thomas, G. New tools to generate natural ice floe fields for computational models. *Under Review*.

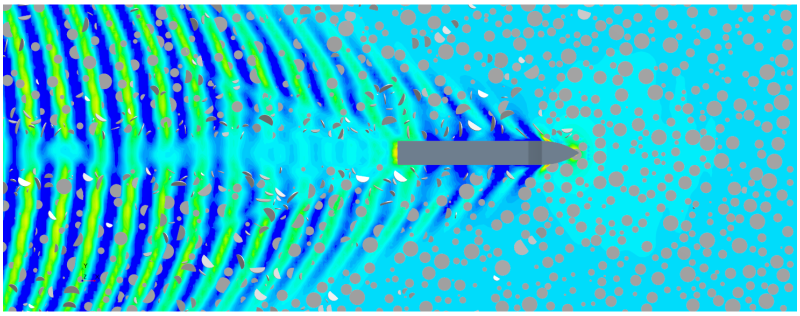

(a) Ice concentration = 30%

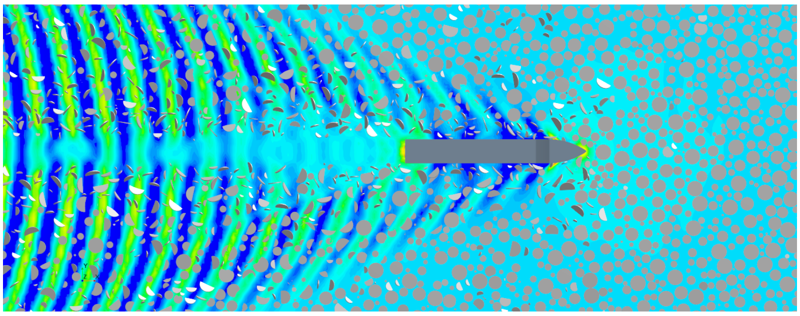

(b) Ice concentration = 50%

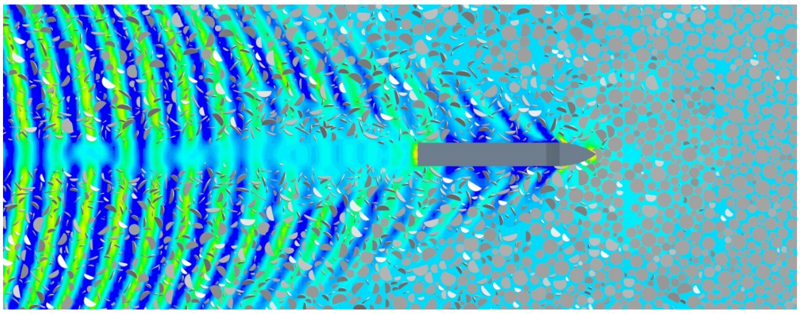

(c) Ice concentration = 70%

Figure 6-9: Simulation view of a ship advancing in floating ice floes, with natural floe fields implemented

6.2 Results and discussion

The predicted steady-state simulations are shown in Figure 6-9: when a ship is advancing in ice floes, ship-ice collisions occur at the bow area and the floes are pushed aside and rotate within the wake; in some cases, floes can slide along the ship before being pushed away. This work focuses on the ship resistance, namely the force born by the ship in its advancement direction, since this determines the power required for such shipping. The total resistance of the ship consists of an ice resistance R_{ice} induced by the floes and a water resistance R_{water} similar to an open-ocean case ($R_{total} = R_{ice} + R_{water}$). R_{ice} occurs due to ship-ice collisions at the bow area as well as the force due to floe sliding, thus the structural loads mainly locate around the waterline and especially around the bow, as shown in Figure 6-10. R_{ice} is calculated by summing of ship-ice contact impulses in the x-direction over a certain time period and then dividing the total impulse by the time. An example of the time-series impulse is shown in Figure 6-11, where the varying values correspond to ship contacts with floes of different sizes and relative locations. Randomness can be seen in the time-series, which is reasonable due to the nature of the floe-distribution algorithms. Therefore, before taking a resistance result, each simulation needs to be run for a sufficiently long time (more than 40 seconds) to offset this randomness (until R_{ice} does not noticeably change with runtime, as shown in Figure 6-12).

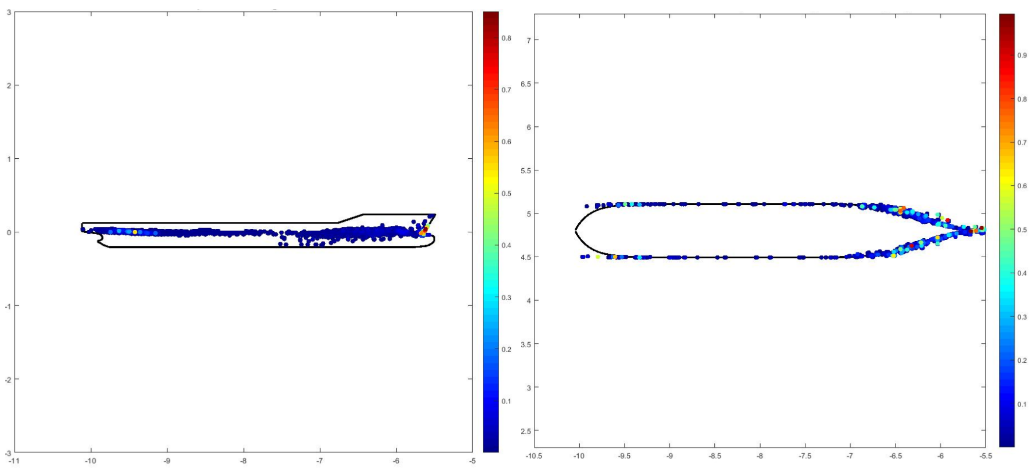

(a) Profile view **(b)** Plan view

Figure 6-10: Heatmap of the ice-induced collisions on the KCS hull

6.2.1 Validation

The predicted resistance has been validated against the experiments conducted in the towing tank of Harbin Engineering University [23]. The computational resistance is compared with available experimental data, where ship speeds ranged from Froude number Fr = 0.06 to 0.18, and ice concentration C = 60% and 70%, ice thickness h = 0.02 m. The comparison between computational and experimental results is presented in Figure 6-13, and the good agreement indicates a reliable accuracy of the model in predicting ship resistance in ice floes. Figure 6-13 also

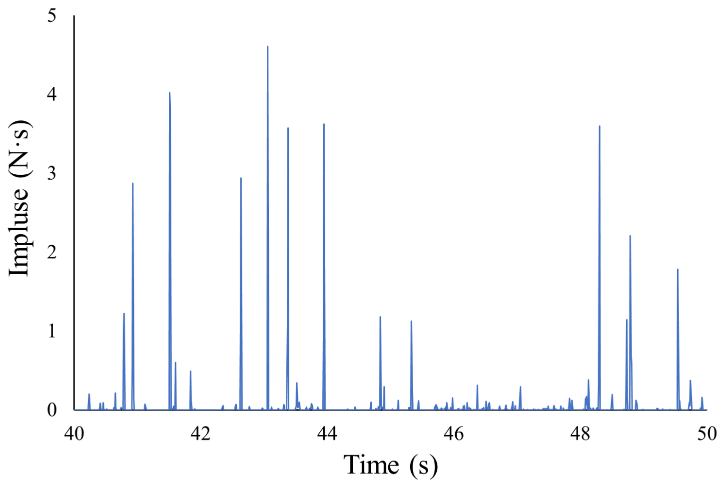

Figure 6-11: Time series of ice-induced impulse against the direction of ship advancement (obtained when $Fr = 0.12$, $C = 60\%$, $h = 0.02$ m and FSD follows [24])

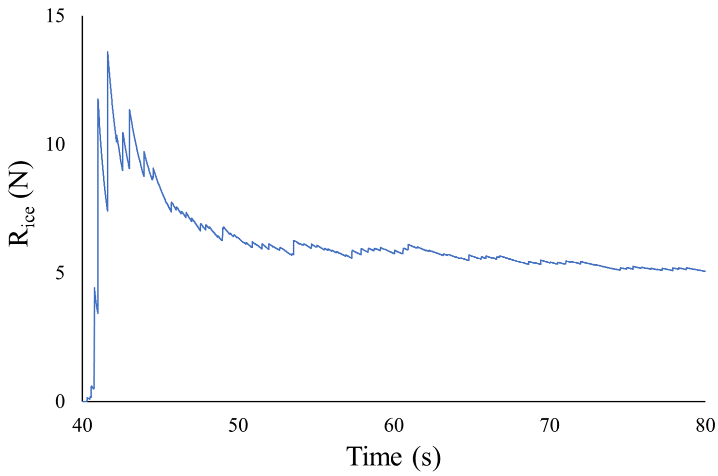

Figure 6-12: Time series of ice resistance: an oscillation is shown when the ship just enters the floe field, and then R_{ice} approaches a steady value over time

shows the open water component, and R_{ice} can be seen as the difference between the total-resistance curve and the water-resistance curve. This work only considers ice concentrations of up to 70%, since ice rafting may occur with higher concentrations (when $C > 79\%$ according to the result of Hopkins and Tuhkuri [119]), while the capability of introduced CFD+DEM approach on modelling ice rafting needs further verifications, where the floe contact is between surfaces rather than edges.

Despite the good agreement between the resistance curves from the experiments

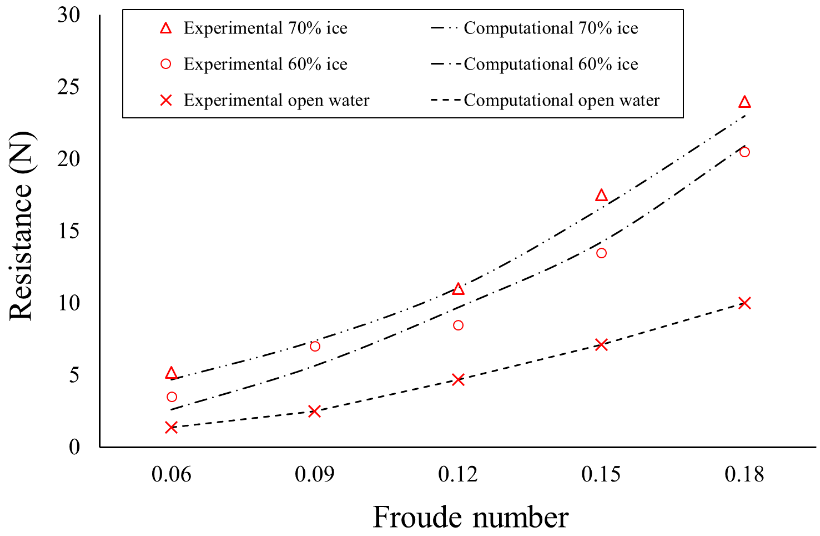

Figure 6-13: Experimental [23] and computational total resistance of the model-scale KCS operating in ice concentration 60% and 70%, alongside the water component

and simulations, there are certain differences between the experimental and computational setups. Firstly Guo et al. [23] applied square shapes of ice, while in the present study the ice was defined to be circular. The reason for this is that the circular ice is closest to the potential Arctic nature. Secondly, the ship heave and pitch were allowed in the experiments, but they are not included in the simulations since both motions were reported to be negligible in the experimental tests. Beyond these two points, the simulations have realistically replicated the experiments; other parts of the model setup, particularly the mass of each floe and the FSD, have been matched.

To ensure the shape difference does not cause large uncertainty in the resistance prediction, a supplementary study is conducted; as shown in Figure 6-14, a simplified test was conducted in which one piece of ice colliding with the KCS bow in different scenarios: (a) circular ice (b) square ice with a flat side towards the bow (c) square ice with a sharp edge towards the bow. This simplified setup can provide valid representation for the simulations shown in Figure 6-9, where each ship-ice collision occurs mostly between the ship and a single floe. In the three scenarios, the ship speed and ice thickness are the same (Fr = 0.12 and h = 0.02 m), and the ice surface area is taken as the median value of the validation experiment [23].

In the three scenarios, the ice-induced impulse against the direction of ship advancement was respectively found to be 16.49, 16.35 and 17.47 $N \cdot s$. This indicates scenarios (a) and (b) cause a similar ice load, and the shape would cause a difference between scenarios (a) and (c), although it is less than 10%. For circular ice, the ice load is the same regardless which side is encountered by the ship; for square ice, the ice load is subjected to the contact angle, which should lay in a spectrum between scenarios (b) and (c). In the simulations shown in Figure 6-9, the ship resistance is a statistical result from a sufficiently large number of floes and a sufficiently long operation time, thus the uncertainty caused by shape difference would be less than 10% too. This agrees with small deviations shown in Figure 6-13 and supports the reasonable adjustment of the ice shape to obtain findings based upon a more realistic ice condition. However, this conclusion cannot be taken as that ice shape is not important in ship-ice interactions; it is based on certain features in this work:

- Ice floes are modelled as rigid in both the simulation and experiment. In reality, the ice could fracture especially in Scenario (c), which would cause a different load.

- The ship speed is relatively fast ($0.06 < Fr < 0.21$), so the ice response is mainly bouncing away, rather than continuous contacts with the ship. In a slow speed condition (usually for ice-structure interactions, considering ice drift speed and a static structure, $Fr < 0.02$), the shape difference would be more influential [151].

- This study limits C to be no more than 70%. With a higher C, a floe would be harder to be pushed away due to the obstacle of other floes; in such a situation, force chains between floes [152, 153] are likely to form, which may make the floe shape important for ship resistance [151].

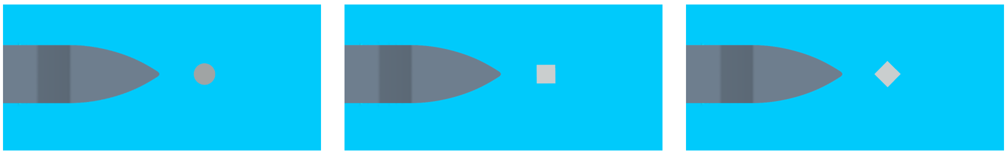

(a) Circular ice **(b)** Square ice flat side **(c)** Square ice sharp edge

Figure 6-14: Ship advancement to make contacts with ice in different floe-shape scenarios

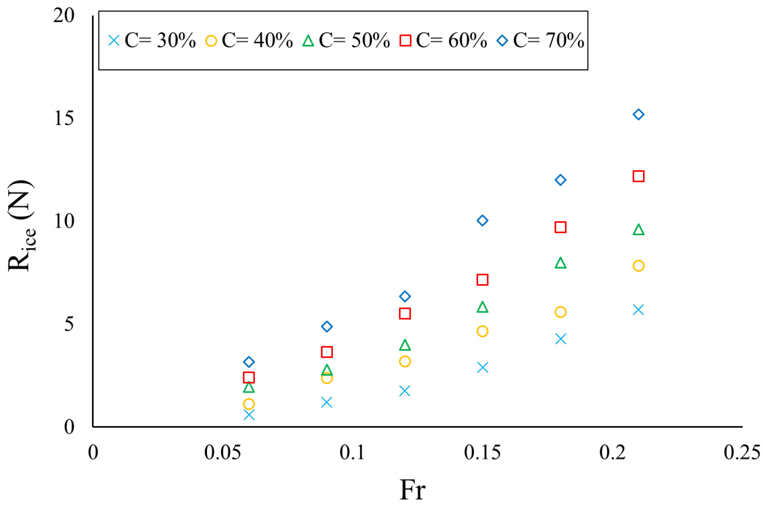

(a) Ice resistance values

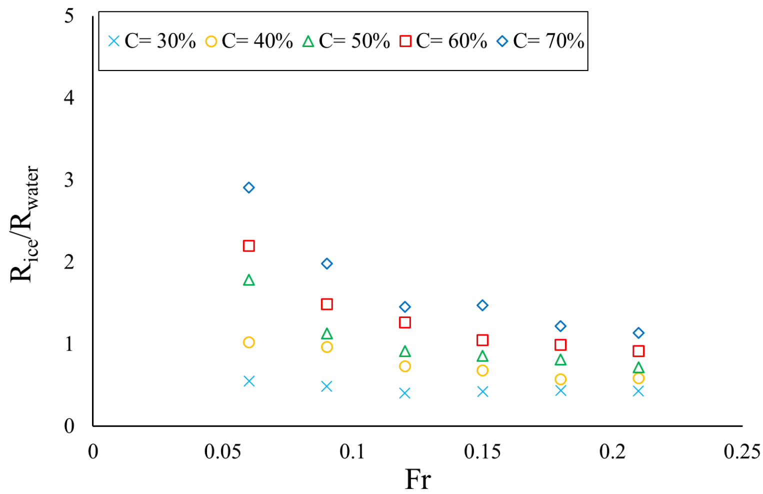

(b) Ice resistance normalised by water resistance

Figure 6-15: Ice-floe resistance for different ice concentrations and ship speeds

6.2.2 Analyses on the ship resistance with ice

Extended simulations were performed to investigate how the ice resistance is influenced by most influential variables, including ship speed, ice concentration, floe diameter, ice thickness and ship beam. Figure 6-15 presents the ice resistance for different ship speeds and ice concentrations. Figure 6-15a shows the variation trend of R_{ice}; regression analyses indicate that the increasing powers of ship speed and ice concentration are around 1.2 and 1.5 respectively in the examined range. Thus, the increase of R_{ice} with an increasing ship speed is slower than that of R_{water} whose power is recognised to be 2. Figure 6-15b presents the ratio of R_{ice} to the corresponding R_{water}, indicating the ice-induced resistance increments in the specific conditions, important for powering and fuel estimates. The ratio is higher when the ship is relatively slow; this is because R_{ice} increases more slowly than R_{water}, also it could be affected by ship-generated waves which tend to push the floes away and reduce the ship-ice contact, as the wave is stronger for a faster ship.

To distinguish the effect of ship-generated wave, comparisons were made between simulations with and without the wave enabled, as illustrated in Figure 6-16. This clearly shows the wave can push the floes away from the hull, while when the wave is eliminated, floes slide closely along the hull and present more contacts. The wave-reduced ship-ice contacts reflect in a reduced R_{ice}, as shown in Table 6-1. The reduction in R_{ice} takes up around 30% in a range of velocities, i.e. considerable but not dictated by the wave strength, which means this effect is essentially about avoiding contacts, rather than how far the floes are pushed away. As the ship-generated wave are shown to significantly influence the ship-ice interaction and ice resistance, it corroborates the importance of the inclusion of CFD flow in the present work. Since previous sole-DEM work in literature reported inaccuracies in certain ranges, it can now be deduced that those inaccuracies may result from the exclusion of ship-generated wave; by contrast, the R_{ice} curves from the current CFD+DEM approach demonstrated to be accurate in the whole examined range.

The influence of floe diameter is analysed by globally scaling all floes, i.e. multiplying the FSD curve with a factor. Figure 6-17 shows the ice resistance with varying floe-diameter input and constant ice concentration. It can be seen that larger floe diameters lead to sparser ice (fewer floes) and lower the collision frequency, while significantly increasing the peak impulses. The overall ice resistance with differ-

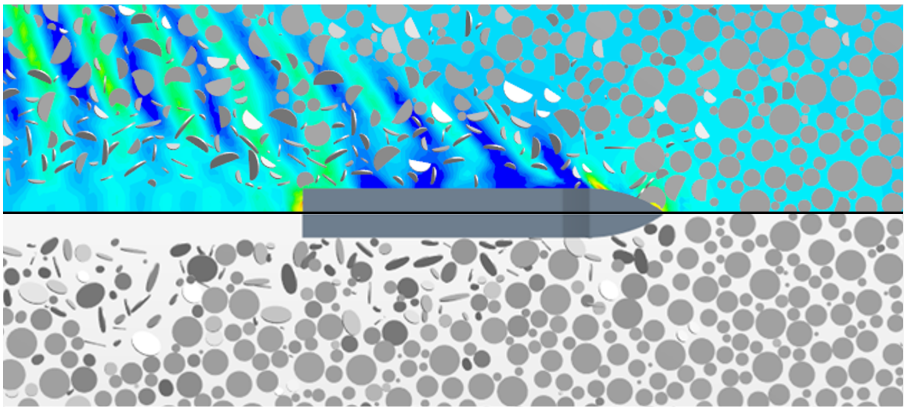

Figure 6-16: Comparison between ship-ice interactions with and without waves

Table 6-1: Comparison of Ice Resistance between with & without Ship-generated Waves, when C = 60%

	Fr = 0.06	Fr = 0.12	Fr = 0.18
R_{ice} with wave (N)	2.40	5.52	9.70
R_{ice} without wave (N)	3.50	8.31	14.49
Relative reduction by the wave	31.4%	33.5%	33.0%

ent floe diameters are plotted in Figure 6-18, in which the resistance obviously increases with increased floe diameters; despite a lower collision frequency, the force integration over time still increases due to the peak values. This indicates that, with the same ice concentration, the effect of floe diameter on ship resistance is more dominant than that of collision frequency. Overall, R_{ice} reveals a linear trend with varying floe diameter.

The influence of ice thickness on the resistance is studied by varying h while keeping other parameters constant. Figure 6-19 presents the ice resistance when h = 0.004 $\sim$ 0.02 m, and for C = 40% and 60%. Similar to floe diameter, R_{ice} reveals a linear trend with varying ice thickness. When FSD and C are held constant, varying h can also be considered as varying the mass of each floe, thus total ice mass ($\sum m_{ice}$) is varied according; similarly, Gong et al. [154] reported a quasi-linear relationship between $\sum m_{ice}$ pushed by a ship and the corresponding resistance. However, in Figure 6-15, $\sum m_{ice}$ changes linearly with ice concentration, while R_{ice} changes at

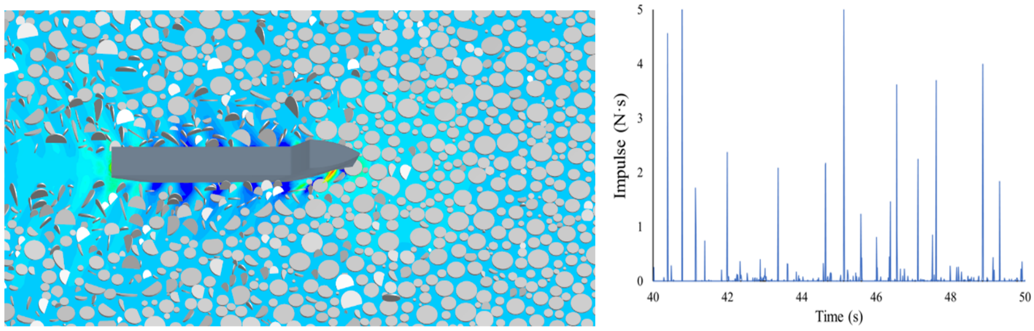

(a) Floe diameters are the same as those in [24]

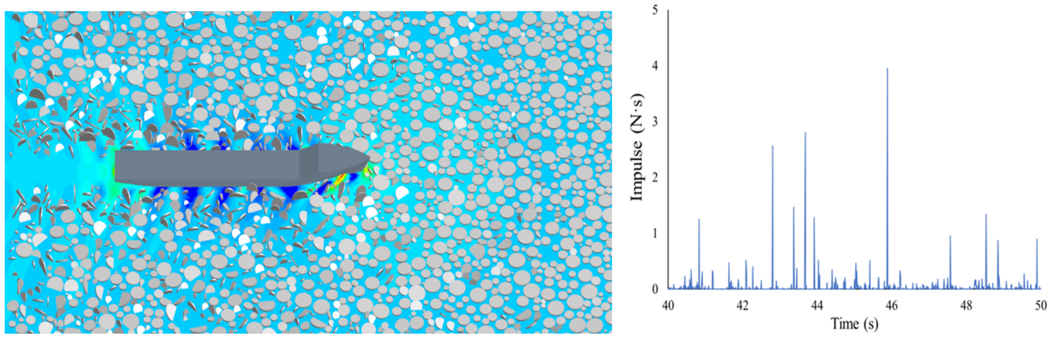

(b) Floe diameters are 60% of those in [24]

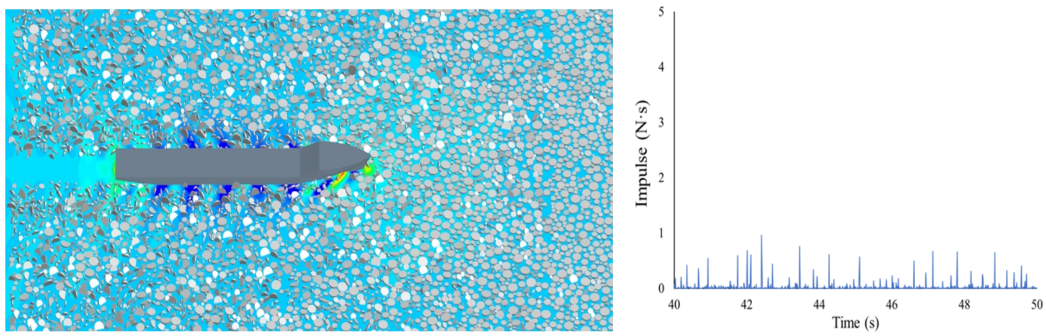

(c) Floe diameters are 20% of those in [24]

Figure 6-17: Ship advancing in different-sized floes (left side) and corresponding time-series of resistance impulse (right side); obtained when Fr = 0.15, h = 0.02 m and C = 60%

power of 1.5; and in Figure 6-17 and 6-18, $\sum m_{ice}$ remains constant when floe diameters are changed, while R_{ice} distinctly changes. This indicates it cannot conclude that ship resistance varies linearly with $\sum m_{ice}$ in this ice-floe scenario, since waves and FSD have introduced high complexities into the associated physics. Each variable needs to be analysed separately in this case.

The influence of ship beam is also investigated, via scaling the ship beam while

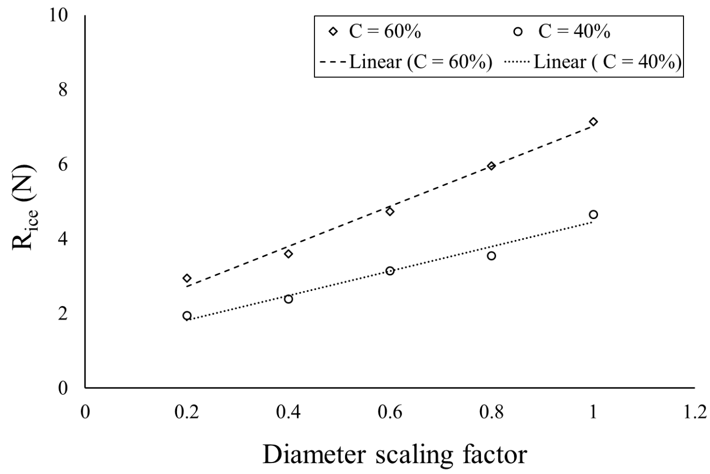

Figure 6-18: Ice-floe resistance in different-sized floes (floe diameters of [23] globally scaled by a factor), obtained when $Fr = 0.15$ and $h = 0.02$ m

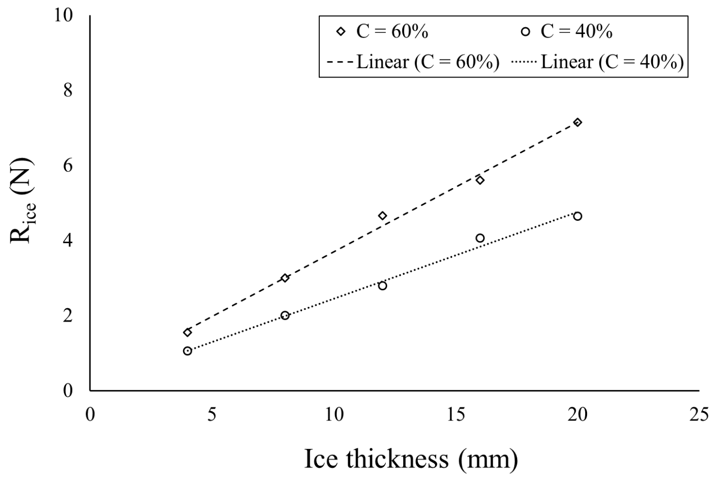

Figure 6-19: Ice-floe resistance in varying ice thickness, obtained when $Fr = 0.15$

keeping a constant displacement by changing the draught accordingly. The impact power appears to be unit, as present in Figure 6-20. This can be attributed to a change in contact surface between the ship and ice. As shown in Figure 6-10, the contacts mainly happen around the waterline at the bow, which makes ship beam an essential parameter because more floes would be contacted if a wider ship is moving. Nonetheless, more advanced bow parameters, such as the shape of fore-ship/stem/bulb [155, 156, 157], could make a different, which is worth further investigations.

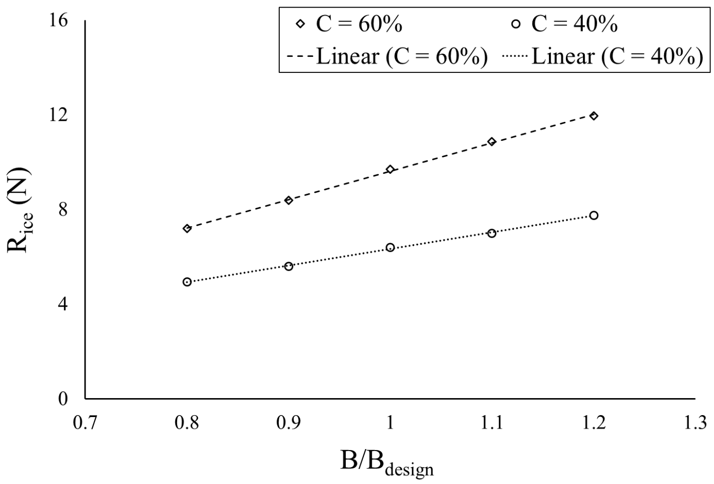

Figure 6-20: Ice-floe resistance as a function of ship beam (normalised by the design beam), obtained when Fr = 0.18 and h = 0.02 m

6.3 Conclusions

In this chapter, a CFD+DEM approach has been developed to simulate a ship advancing in floating ice floes, since this condition has been predicted to be a primary environment of Arctic shipping. Relevant numerical theories and practicalities have been presented in detail: CFD is incorporated with DEM to model desirable ship-wave-ice interactions, and two algorithms for generating natural ice-floe fields have been provided. The developed model shows the capability to simulate and analyse the proposed problem with high fidelity, and it is validated to be accurate in predicting the ship resistance induced by ice floes. Based on the developed model, a series of simulations have been performed to investigate how the ice resistance is influenced by ship speed, ice concentration, ice thickness, floe diameter and ship beam.

This chapter has demonstrated a new computational technique that can be used to perform ship power estimates and hull form design for ice-floe conditions. Nonetheless, the simulations require a relatively long time to run, so it is limited from applications that require rapid computing. In the next chapter, a procedure will be developed to derive swift equations based on the simulation results, followed by the corresponding incorporation into a set of real-time applications.

Chapter 7

Incorporation of simulation results with real-time applications

A CFD-based simulation requires a relatively long time to complete, so they may not be directly compatible with applications requiring rapid computing. For example, a Voyage Planning Tool (VPT) for Arctic shipping requires real-time metocean and ice data to calculate a ship's resistance along potential routes, so as to suggest routes with lower energy costs. Although valid computational models have been provided by the precedent work, the speed of performing the simulations still cannot meet the speed requirement of a VPT to update results.

To overcome the speed limitation, this chapter presents a procedure developed to derive rapid ice-floe resistance equations based on the computational results from Chapter 6, which in turn enables real-time prediction of ship resistance in ice floe fields. The derived equation is validated against model tests and full-scale measurements, and demonstrations are given on the incorporation of the empirical equation into a set of new Arctic ship performance model and VPT.

A version of this chapter has been submitted for publication as: Huang, L., Li, Z., Ryan C., Ringsberg, J., Pena, B., Li, M., Ding, L. and Thomas, G. Ship resistance when operating in floating ice floes: derivation, validation, and application of an empirical equation. *Under Review*.

7.1 Derivation of an equation for ice-floe resistance

This section starts by introducing a non-dimensional procedure to derive a rational expression of R_{ice} for ice floe fields. Subsequently, the ice resistance equations for the three different ships are derived, and their differences are discussed to further derive a generic equation to account for different ships. Then, the derived generic equation is validated by predicting ice resistance for existing experimental conditions. Furthermore, a discussion is given on the extrapolation of the equation from model-scale to full-scale.

7.1.1 Non-dimensional analysis

To obtain a rational expression of R_{ice}, it is first expanded using principal parameters identified in Chapter 6. This gives:

$$R_{ice} = A \times \rho_{ice}^{a} \times h^{b} \times D^{c} \times U^{d} \times B/L_{pp}{}^{m} \times C^{n} \tag{7.1}$$

where A is a coefficient dependent on the specific ship, and ρ_{ice} is the ice density used for matching up the units between the left and right hand sides of the equation. Subsequently, using a standard non-dimensional method to fit the units of both sides, it gives: $a = 1, b + c = 2$ and $d = 2$, thus:

$$R_{ice} = A \times \rho_{ice} \times h^{b} \times D^{c} \times U^{2} \times B/L_{pp}{}^{m} \times C^{n} \tag{7.2}$$

Then, according to the regression powers shown for h, D, B and C, it gives $b = 1, c = 1, m = 1$ and $n = 1.5$. Since the power of speed was found to be 1.2 while its unit-based power is 2, the dimensionless parameter Froude number is introduced to fulfil both the power and unit; thereby the power of Fr derives to be -0.8, therefore:

$$R_{ice} = A \times \rho_{ice} \times h \times D \times U^{2} \times B/L_{pp} \times C^{1.5} \times Fr^{-0.8} \tag{7.3}$$

In reality, ice floes in a given region are of different dimensions, where h has little variation while D of floes can be notably different. Thus, it is recommended to input a constant h and calculate an average D based on an average Aspect Ratio (AR), i.e. $D = h \times AR$. Field measurements reported that a common average value for AR is 10 for ice floe fields [110]. The ice density, ρ_{ice}, can be held constant as 900 kg/m^3.

7.1.2 Unification for multiple hull forms

Equation 7.3 has accounted for the influence of ship beam, while other parameters of the hull geometries still make the ice resistance coefficient (A) different for different ships. To investigate the underlying reasons and derive a generic equation, the ship-wave-ice interactions of three hulls were analysed; they are the KRISO Container Ship (KCS), the Japan Bulk Carrier (JBC), and a real Arctic In-service Vessel (AIV). These are three typical ship types that are expected to operate on future Arctic shipping routes, and they have significantly different hull forms that represent the diversity of current shipping fleets. Their dimensions and hull geometries are shown in Table 7-1 and Figure 7-1.

Table 7-1: Main Particulars of the Studied Hull Forms

	KCS	**JBC**	**AIV**
Ship type	Container ship	Bulk carrier	General cargo carrier
Length between perpendiculars [m]	230.0	280.0	186.4
Waterline beam [m]	32.2	45.0	28.5
Draught midships [m]	10.8	16.5	11.0
Block coefficient [-]	0.651	0.858	0.79
Wetted surface area [m^2]	9424.0	19556.1	8153.0

These three ships are separately incorporated within the CFD+DEM model, as shown in Figure 7-2. The inserted hull geometries are in a model scale of 1:52.667, which was chosen to allow comparison of the simulations against model tests [23]. For each of the three ships, systematic simulations were conducted to study relevant environmental variables, which is done by varying one parameter and holding others constant. These regression powers obtained for KCS do not have a notable

(a) Profile view

(b) Plan view

(c) Front view

Figure 7-1: Geometries of the KCS, JBC and AIV ships, in the order of KCS, JBC and AIV (image sizes correspond to the actual ship sizes)

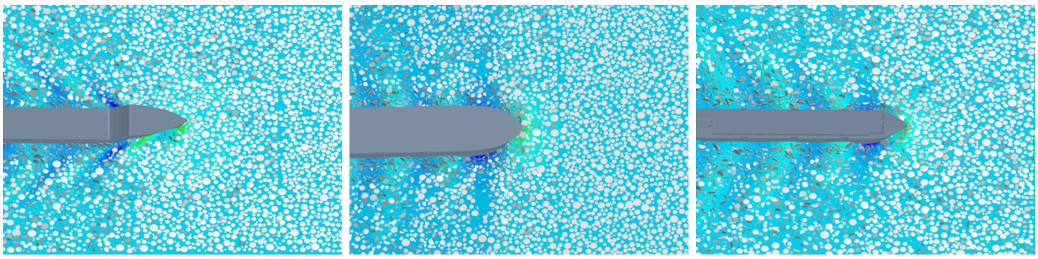

(a) KCS **(b)** JBC **(c)** AIV

Figure 7-2: Simulations of different ships advancing in ice floe fields

difference from those obtained for JBC and AIV. However, after inserting the parameters of KCS, JBC and AIV hulls into Equation 7.3 to find their coefficients (A), it gives A_{KCS} = 7.64, A_{JBC}= 11 and A_{AIV}= 5.5.

To investigate the reasons for these hulls to have different R_{ice} coefficients, the ship-wave-ice interactions of these three hulls were analysed, by which, two influential bow parameters were identified: buttock angle (γ) and waterline angle (α), which are illustrated in Figure 7-3.

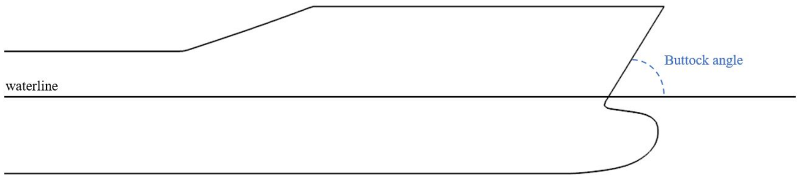

(a) Central plane of the KCS hull

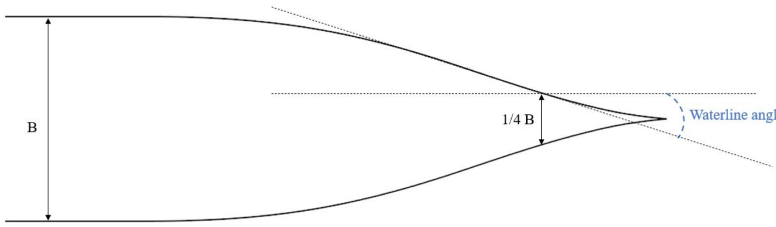

(b) Waterline plane of the KCS hull

Figure 7-3: Graphic expression of buttock angle and waterline angle, defined following the International Association of Classification Societies [25]

The buttock angle mainly influences the ship-wave-ice interaction in the vertical direction. It may be observed in Figure 7-1a that the bow of KCS or JCS has a buttock angle of around 60°, while the AIV has a vertical stem, i.e. buttock angle is 90°; the buttock angle dictates the contact surface between the ship and floes, which influences the ice resistance.

The waterline angle mainly influences the ship-wave-ice interaction in the transverse direction. KCS has a sharp bow shape across the waterline, while JBC and AIV have relative round shapes across the waterline. The round shape tends to generate a wave profile that pushes ice floes aside from the ship, as shown in Figure 7-4. This wave profile results in a reduction in the ice resistance.

To unify the ice-floe equation for multiple hull forms, the bow angles of KCS, JBC and AIV were measured and shown in Table 7-2. γ and α are required to be inserted in Equation 7.3 to account for their influences. The influence of buttock angle on the ice-induced resistance was discussed by Riska et al. [85], where the authors note

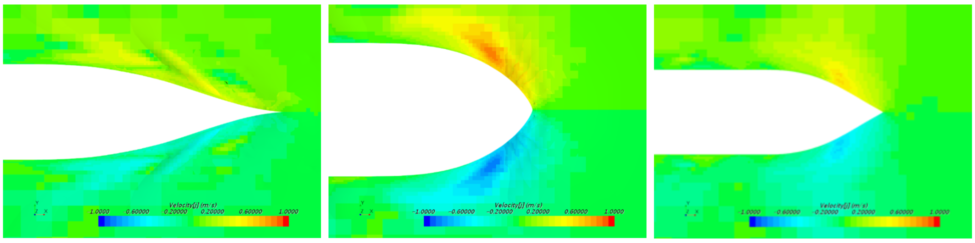

(a) KCS **(b)** JBC **(c)** AIV

Figure 7-4: Waterline velocity fields around different bows ($Fr = 0.12$), colour contours show the velocity magnitude in the transverse direction

Table 7-2: Bow Angles of the Candidate Ships and the Corresponding R_{ice} Coefficients in Equation 7.3

	KCS	JBC	AIV
Buttock angle (γ) [degrees]	58	61	90
Waterline angle measured at 1/4 beam (α) [degrees]	18	50	30
Calculated ice floe resistance coefficients [-]	7.64	5.5	11

that, for icebreaking vessels, R_{ice} tends to be proportional to the tangent of γ, but their extensive experience shows that the influence of γ on R_{ice} is less dominating than a tangent function for non-icebreaking vessels; thus, γ is instead taken to have a unit-power correlation with R_{ice}. After normalising a unit power of γ against the ice-resistance coefficients for the three ships, the reduction effect of α on R_{ice} is shown to be a cosine function. Therefore, Equation 7.3 becomes:

$$R_{ice} = 0.13665 \times \gamma \times \cos\alpha \times \rho_{ice} \times h \times D \times U^2 \times B/L_{pp} \times C^{1.5} \times Fr^{-0.8} \quad (7.4)$$

Equation 7.3 and Equation 7.4 provide identical results, while Equation 7.4 is applicable for all the three investigated ships without requiring the calculation of a specific coefficient for a specific vessel. Equation 7.4 can provide relatively accurate prediction of ice-floe resistance for all the three ships investigated in this study, as shown in Figure 7-5, 7-6 and 7-7. Following the same approach, further parameters and relationships could be identified when more data becomes available in future work.

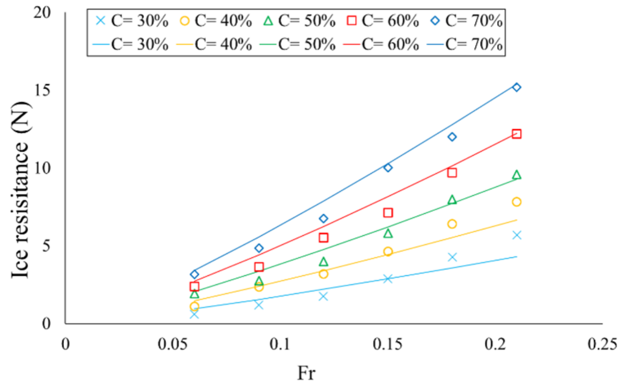

Figure 7-5: Ice-floe resistance calculated by simulations (dots) and Equation 7.4 (lines), for KCS hull at model scale (1:52.667), when h = 0.02 m

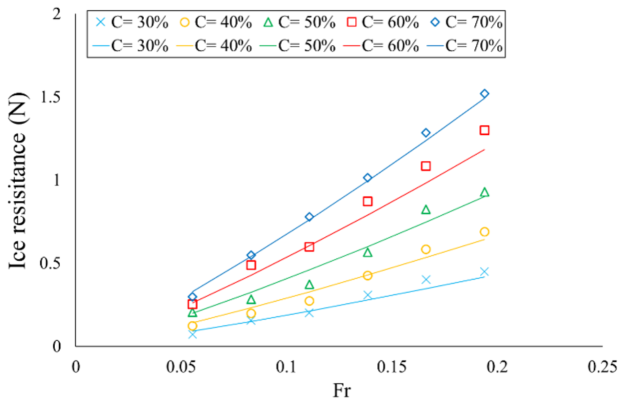

Figure 7-6: Ice-floe resistance calculated by simulations (dots) and Equation 7.4 (lines), for JBC hull at model scale (1:52.667), when h = 0.0066 m

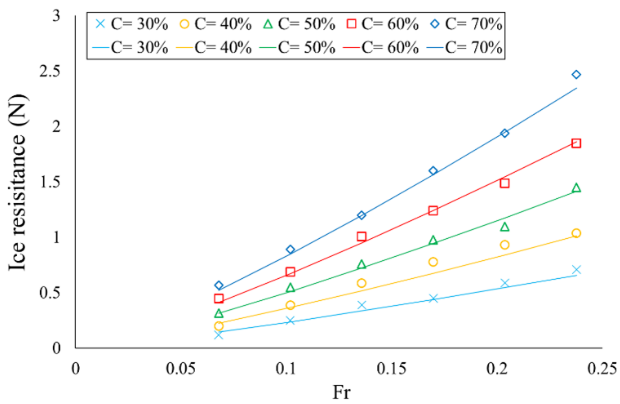

Figure 7-7: Ice-floe resistance calculated by simulations (dots) and Equation 7.4 (lines), for AIV hull at model scale (1:52.667), when h = 0.0066 m

The uncertainty of the derivation process is analysed through nondimensionalising R_{ice} by parameters of Equation 7.4. As shown in Figure 7-8, most of the nondimensionalised R_{ice} lays in a range of $0.13665 \times (1 \pm 15\%)$, which indicates the inherent residual. The residual is expected due to the nature of empirical derivation, and the 15% level has made an improvement than previous work (e.g. Figure 19 of [23]) by including more parameters that were not considered in previous simpler ice-floe resistance derivation. However, the residual could be further reduced by applying advanced machine learning algorithms [158, 159, 160]. When predicting ship fuel consumption of an ice-infested route, the uncertainty level is expected to be less than 15% as highly variable ice conditions should offset the residual of each other.

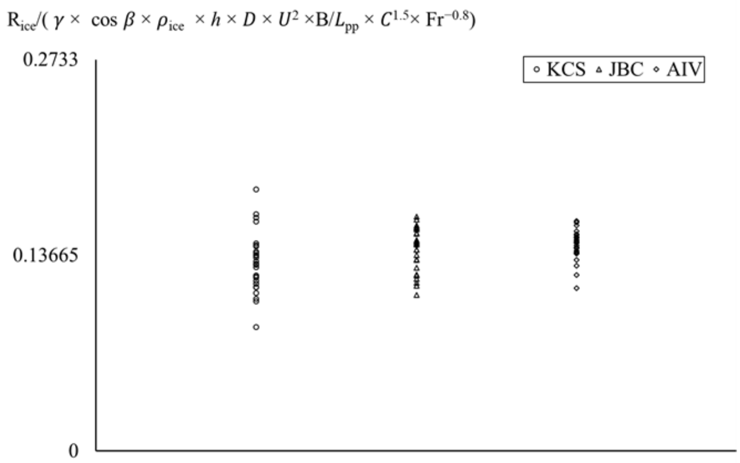

Figure 7-8: R_{ice} data from simulations nondimensionalised according to Equation 7.4

7.1.3 Validation

The equation to predict ice-floe resistance was validated against two sets of model tests with different hull, ice and speed conditions:

Firstly, Equation 7.4 was used to provide prediction against the experiments conducted in the towing tank of Harbin Engineering University in China [23], where a model-scale KCS hull was towed through a field of numerous pieces of floating paraffin wax, mimicking rigid ice floes. The floe resistance was interpreted as being the total ship resistance in floes minus the corresponding calm water resistance without floes. To make the comparison, Equation 7.4 was directly inputted with the same ship, ice, operating parameters used in the experiments, where the ship speed ranges from $Fr = 0.03$ to 0.18, ice concentration ranges from C = 60% to 90%, and ice thickness $h = 0.02$ m. The comparison between computational and experimental results is presented in Figure 7-9, where Equation 7.4 is shown to be fairly accurate and the deviations are reasonably within the range of derivational and experimental uncertainties.

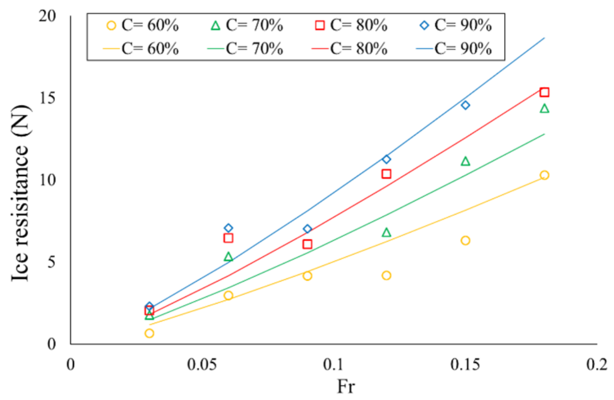

Figure 7-9: Comparison between ice-floe resistance of 1:52.667 KCS hull model measured by experiments [23] (dots) and calculated by Equation 7.4 (lines)

To further confirm the accuracy of Equation 7.4, another set of experiments were found that were recently conducted in the Korea Research Institute of Ships and Ocean Engineering [26]. Towing tests were carried out in laboratory ice floes for an Araon ship whose hull form considerably differs from the three hulls studied earlier, as shown in Figure 7-10. Equation 7.4 was directly inputted with the same ship, ice, operating parameters that used in the experiments, where the ship speeds are $Fr = 0.017$, 0.05 and 0.084, ice concentrations are C = 60% and 80%, and ice thickness $h = 0.057$ m. The comparison presented shown in Figure 7-11 shows good agreement; in particular, this demonstrates the derived equation can be applicable to other hull shapes, speeds, and ice conditions that were not considered in the derivation process.

For the lowest speed and $C = 80\%$ in Figure 7-11, it may be seen that the experimental resistance is significantly larger than predicted by Equation 7.4. Kim et al.

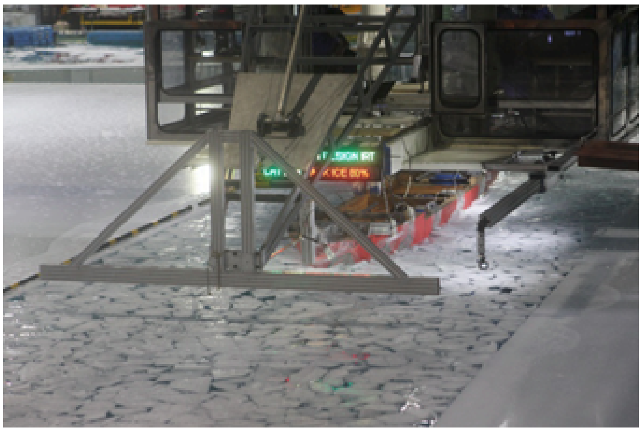

Figure 7-10: Ice model tests of 1:18.667 Araon hull model reported by Kim et al. [26]

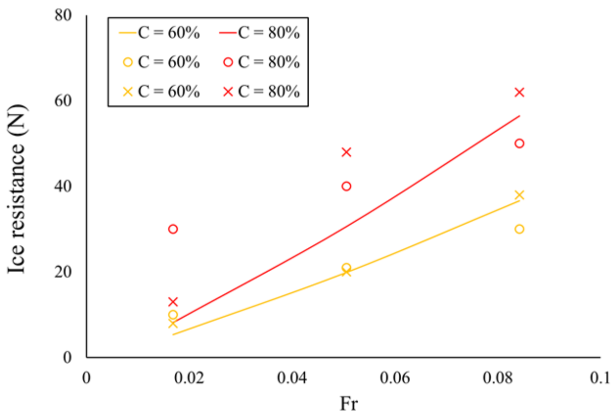

Figure 7-11: Comparison among ice-floe resistance of 1:18.667 Araon hull model given by Equation 7.4 (lines), by experiments (circles), and by the finite-element method (crosses) of Kim et al. [26]

[26] indicate that this test condition could be a special case, as the reported value is also much higher than that predicted by their finite-element model. It is expected that R_{ice} should equal 0 when $Fr = 0$, while the experimental R_{ice} is approximate 30 N when Fr is very small at 0.017 and the slope would lead to a clearly unphysical R_{ice} (larger than 20 N) even when $Fr = 0$. The same phenomenon is discussed by Riska et al. [85], where they indicated that at very low speeds ships cannot proceed continuously in ice towing tanks, thus the measured average towing force is not directly applicable to the prediction of R_{ice}.

In addition, noting that the floe shape is circular in the present work, square in Guo et al. [23], and an irregular polygon in Kim et al. [26], the coincident trends and agreement among these works indicate that floe shape may not be a critical parameter for the ice resistance of the studied conditions.

7.1.4 Full-scale extrapolation

The computational modelling was conducted at model scale to allow validation against experiments, so it is important to discuss how the derived R_{ice} equation can be applied to full-scale ships. For water resistance (R_{water}), the derivation of formulae from model tests usually needs to apply the ITTC extrapolation procedure [161], since it is impossible to ensure Froude and Reynolds numbers are both equal between full scale and model scale, in which, the former governs gravity/inertia (waves) forces and the latter governs viscous forces. R_{water} can be divided into a wave component and a frictional component; in model tests, scaling based on a consistent Froude number is practical, which scales the wave component correctly yet brings about certain errors within the friction component due to changes in Reynolds number. The errors in friction may be corrected using the ITTC method [161].

Similarly, for the extrapolation of ice resistance, Froude and Cauchy numbers should be both equal between full scale and model scale, otherwise a correction procedure would also be required [162]; Cauchy number relates to the elasticity of ice, whose consistence is for ensuring the elastic reaction forces of ice are correctly scaled, which is essential to accurately represent the icebreaking process. However, in the present ice-floe case, in principle the small floes are pushed away rather than broken by the ship, so the floes can be assumed to be rigid [147], thus the Cauchy number is infinitely small in both scales and relevant corrections do not need to be applied. Therefore, the present work proposes that Equation 7.4 can be directly applied to full scale, as the non-dimensional derivation has already kept the expression in line with Froude's law.

7.2 Arctic ship performance model and voyage planning tool

The achievement of Equation 7.4 is to provide a rapid estimate of ice-floe resistance for a given ship in a given ice condition, which in turn enables its incorporation within real-time applications. The derived ice-floe resistance equation has already been incorporated into a new Arctic Ship Performance Model (ASPM) and VPT [163], which is briefly introduced in this section.

The calculation procedure of the ASPM is given in Figure 7-12. It can be seen that most of the procedure can be completed using classical naval architecture methods [164, 165, 166], whilst an essential addition is the calculation of added resistance due to ice. In the ASPM, ice resistance is classified into large ice floes and small ice floes. These two conditions correspond to significantly different physics during the ship-ice interactions. Large ice floes undergo crushing and break-up when ships are operating through them, and the ultimate of this case is level ice. By contrast, small ice floes have a high degree of freedom, thus their response to ships is mainly being pushed away rather than fractured. Extreme ice conditions, such as ice ridges, are not considered in the ASPM, since they are designed to be detected by the crew and avoided during operations. Therefore, two different methods were required to account for the ice resistance in large and small ice-floe scenarios, for which the ASPM respectively incorporated the empirical method provided by FSICR using the equivalent ice thickness [144, 167] and Equation 7.4 derived in the present work. After incorporating ice-resistance equations, the ASPM has the capability of predicting the fuel consumption and attained speed for ships navigating in ice-infested routes. The threshold between large and small floes in the current ASPM is $C \times h = 0.3$ meter, which is based upon the classification of UK Met Office that when $C \times h > 0.3$ meter, first-year ice starts to grow and ship-induced fracture is expected occur, and when $C \times h \leq 0.3$ meter, ice types are young grey, pancake and grease floes that do not expect ship-induced fracture [168].

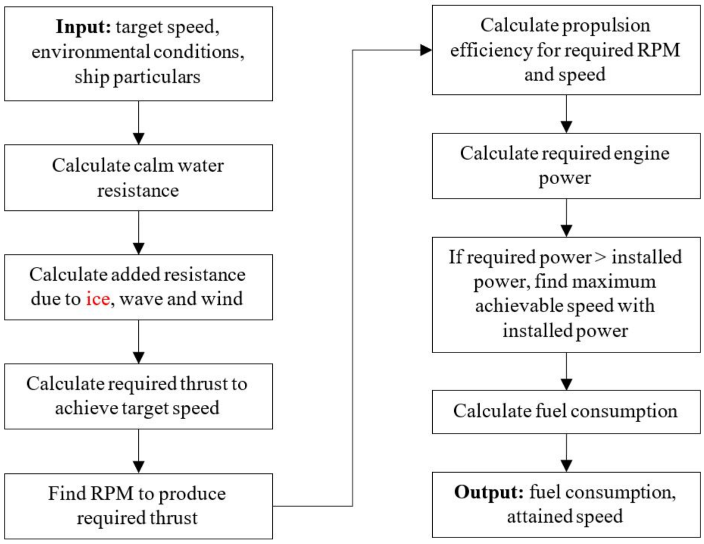

Figure 7-12: Calculation procedure of the Arctic Ship Performance Model

The ASPM was integrated into a VPT [169] which links with real-time weather and ice forecasting systems to calculate a ship's fuel consumption along all potential routes. Then the VPT performs two steps to determine the optimised route: (a) eliminate any route that contains an ice condition to violate the POLARIS standard to cause a structural risk [170] (b) suggest the route with the least fuel consumption. The coupled weather systems include the Copernicus Marine Environment Monitoring Service that provides metocean data, and the UK Met Office Forecast Ocean Assimilation Model that provides sea ice data [168]. Figure 7-13 provides two examples of suggested routes for a ship travelling through the Northern Sea Route, obtained using the VPT based on historical metocean and ice data in 2018. In Figure 7-13(a), it can be seen that the majority of the Arctic was covered by sea ice at that time (early summer), and the VPT chose a route close to the Russian coastline, where the ice conditions were not severe; in Figure 7-13(b), the Arctic sea ice reached the annual minimum (late summer), and the VPT chose a shorter route via the higher-latitude Arctic Ocean. These route choices show the VPT can minimise the ship fuel consumption based on a comprehensive consideration of shorter voyage distance and less ice impacts, which signifies its practical value to Arctic shipping.

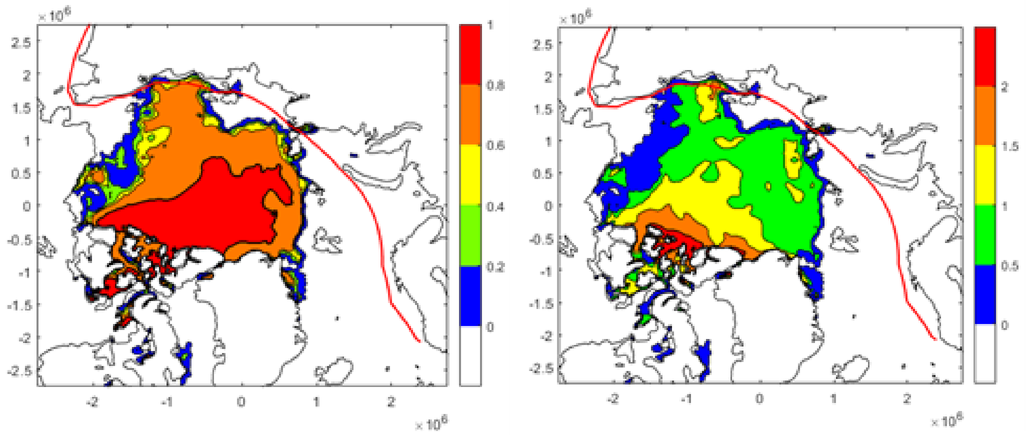

(**a**) 20 July 2018 - 15 August 2018, when the majority of the Arctic was covered by sea ice

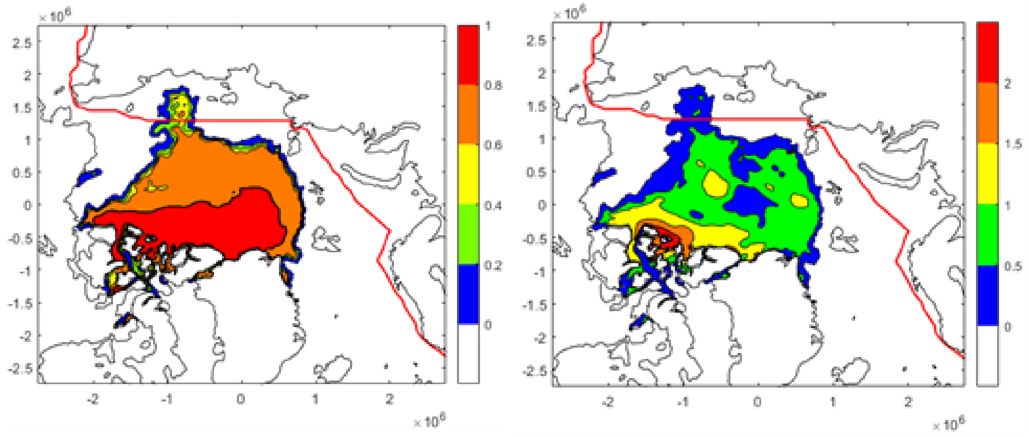

(**b**) 01 September 2018 - 24 September 2018, when Arctic ice was the least of the year

Figure 7-13: Two VPT-suggested routes for a ship travelling through the Northern Sea Route, obtained using the metocean and ice data of early & late summer 2018. Colour bars show ice concentration in the left panels and ice thickness (meter) in the right panels, and the x and y axes denote the distance (meter) with respect to the North Pole origin

7.3 Comparison with full-scale measurements

Full-scale measurements were collected for the real AIV ship during a voyage through a segment of NSR near the East Siberian Sea. The data were recorded from 03:00 AM 05/08/2018 to 11:30 PM 07/08/2018. The ship's central computer recorded the ship's engine RPM, GPS position, encountered wind speed and direction, and attained speed. The encountered sea ice concentration was collected by the onboard cameras that were specifically equipped for sea ice monitoring. Figure

7-14 plots the measured RPM and ice concentration along the voyage. The figure shows that the RPM is first manually reduced by the crew, before entering the ice-floe field, which is to slow and protect the ship. After entered the ice floe field, the RPM is increased due to the additional ice resistance and fluctuates with the variation of ice condition. After the ship passed by the ice-floe field, the RPM is manually increased to speed up the ship in open water.

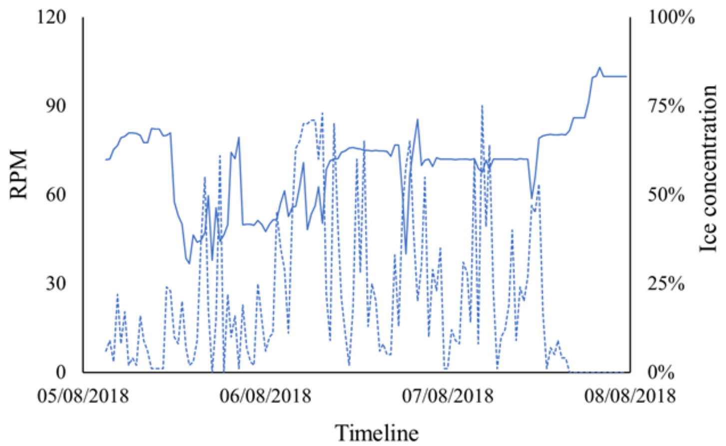

Figure 7-14: Full-scale measurement of engine RPM (solid line) and sea ice concentration (dashed line)

This particular voyage was replicated using the ASPM and VPT. The inputs included (a) the onboard recorded ice concentration, wind data and ship RPM; (b) ice thickness that was inputted from historical satellite data of the UK Met Office, where the ice thickness did not show a notable variation along the voyage, thus a constant value of 0.35 m was taken, which is the average of the encountered sea ice thickness; (c) the historical metocean data from the Copernicus Marine Environment Monitoring Service, which includes waves and currents. Throughout the whole voyage, the encountered sea ice was observed to be small ice floes that have negligible ship-induced fracture; therefore the ice resistance was calculated by Equation 7.4 rather than FSICR.

Using the ASPM and VPT, the ship was set to sail at the measured RPM following the same route that recorded by the GPS. Based on the inputs of the environmental variables, Equation 7.4 and open-water ship resistance equations were used to calculate the variation of ship total resistance along the route. Then, the predicted total resistance is combined together with the RPM and propulsion system (Table 7-3) to calculate the attained speed and fuel consumption of the ship. The measured ship speed was compared with the predicted value in Figure 7-15. The comparison shows good agreement, justifying the rationality of using Equation 7.4 to account for ice-floe resistance in such a VPT application.

This example presents a workable approach that uses the derived ice-floe equation to rapidly predict ship performance in ice-infested seas, which meets relevant engineering requirements for a real-time application. Nonetheless, it should be noted that this full-scale validation has only been performed against a three-day voyage, due to the scarcity of available data containing ice-floe conditions. A complete validation procedure for a mature ice-floe equation will need more field and experimental data to help confirm its accuracy.

Table 7-3: Particulars of the Propulsion System of AIV

Main engine	WinGD 6RT-flex50-D
Maximum Continuous Rating (MCR)	10,470kW * 124 r/min
Continuous Synopsis Record (CSR = 65% MCR)	6,806 kW * 107.4 r/min

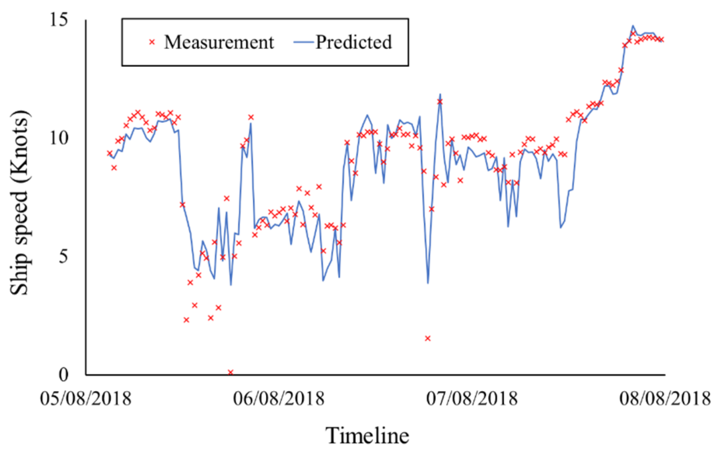

Figure 7-15: Predicted attained ship speed against full-scale measurements

Table 7-4: Comparison of Journey Time, Fuel and Cost between Voyages through the NSR and the Suez Route. VPT Simulations were Made from Shanghai to Rotterdam based on the Historical Weather Data of 2018 [27]. The Consumed Fuel is Assumed to be the IFO380 Type and the Price is £298 per Tonnes

		190-meter general cargo			**245-meter container ship**		
	Sailing season	Journey time (days)	Fuel (tonnes)	Fuel cost (GBP)	Journey time (days)	Fuel (tonnes)	Fuel cost (GBP)
NSR	July	25.2	484.6	144.4k	25.2	996.5	297.1k
	September	24.6	519.2	154.8k	24.6	983.8	293.3k
Suez Route	July	28.6	709.4	211.5k	28.6	1453.4	433.4k
	September	28.3	667.9	199.2k	28.3	1406.7	419.5k

7.4 Fuel and cost comparison between the Arctic and traditional routes

To further explore the profit afforded by Arctic shipping, it is of interest to discuss the potential saving of adopting an Arctic sea route with shorter distance but involving additional ice resistance and icebreaker assistance cost. A comparison here is made between the NSR and its traditional counterpart, the Suez route. The comparison is not made for the NWP because the practicality for employing the NSR is currently greater than for the NWP. As introduced by Ryan et al. [171], the NWP is made up of straits through the Canadian Arctic Archipelago that are both narrow and shallow. These straits are easily clogged by free floating ice, and are still insufficiently surveyed, presenting the very real risks of ship grounding or stuck in ice; By contrast, the NSR presents a less complex geography, which is currently the most promising Arctic route and under development by substantial international efforts [172].

Using the VPT, Li et al. [27] compared Shanghai-Rotterdam voyages during the same period of time while via the NSR and the Suez route separately. Their study considered different periods of summer 2018 and different vessel types. The result shows that the NSR voyage consumed $22 \sim 32\%$ less fuel than the Suez route, even having considered ice resistance. The saved fuel is around 200 tonnes for a 190 m general cargo and 400 tonnes for a 245 m container ship, respectively signifying a cost saving of around £60k and £120k. The potential icebreaker assistance cost through the NSR is roughly equal to the toll of the Suez Canal. A detailed calculation based on Li et al.'s data is given in Table 7-4.

7.5 Conclusions

This chapter has presented an approach to derive a computationally cheap empirical equation for predicting ship resistance when operating in floating ice floes. Based upon extensive computational simulations and analyses, the equation explicates how the ice resistance is related to hull, speed and ice parameters, providing valuable insights for polar ship design and engine power estimation. In particular, the influences of buttock and waterline angles were investigated.

Furthermore, the derived equation enables the quick prediction of ice-floe resistance on a given ship in given ice conditions, which has facilitated the development of an Arctic ship performance model and voyage planning tool. These applications reveal significant practical value through demonstrating the ability to estimate fuel consumption for ice-going ships and optimise their routes on a real-time basis.

Validation against both model-scale and full-scale results demonstrate the rationality of the non-dimensional derivation procedure and the accuracy of the proposed ice resistance equation. However, since available experimental and field data on the present problem are still scarce, there could be extra parameters and relationships of the equation to be identified, as more data becoming available in the future.

Chapter 8

Concluding remarks

8.1 Summary

In the Arctic shipping routes, consolidated ice cover has been extensively replaced by ice floes and open water. This new environment allows waves to propagate in the region and is navigable for commercial ships without icebreaking capabilities. To study the emerging Arctic ice condition and ship operation, this work identified four primary scenarios and developed models to accurately simulate each of them. The first two models simulated wave-ice interactions, considering ice first as rigid and then as elastic. The third model simulated the operation of a ship in an open-water channel between two ice sheets, applicable when level ice is encountered in certain routes and icebreaker assistance would be required. The fourth model simulated the process of a ship advancing in floating ice floes, particularly having achieved realistic modelling of floe size distribution. Following validation against experiments, this work demonstrated high-fidelity reproduction of the scenarios and accurate prediction of the ice resistance on a ship.

Through development and validation of these new models, this work answered the question of how to accurately model the potential ship-wave-ice interactions: CFD was used to model ship and wave hydrodynamics and it was coupled with (a) six-degree-of-freedom equations to model rigid ice motions (b) computational solid mechanics to model elastic ice deformations, and (c) discrete element method to model ice-floe collisions with each other or with a ship.

Subsequently, extensive simulations were performed to analyse the ship-wave-ice interactions, and the principal insights are summarised below:

- When ocean waves encounter an ice floe, the wave energy partially passes the floe and is partially reflected; meanwhile, the ice response is mainly rigid motions when the ice dimension is relatively small to the wavelength and elastic deformations when it is large. With an increased incident wavelength, the proportion of wave transmission is larger, and the ice response gets stronger; when the wavelength is larger than three times the ice dimension, most of the wave energy can effectively transmit and the ice floe contours on the free surface following the same amplitude as the wave motion. A specific phenomenon, overwash, was analysed in detail, since it was reported to be the main capability gap of contemporary analytical solutions. Overwash was demonstrated to be strongly dictated by incident wave amplitude, as a larger wave amplitude can increase the water depth on top of an ice floe. The effect of overwash is to reduce wave transmission and suppress the floe motions.

- When a ship is advancing in an open-water ice channel, the ice sheets on both sides were shown to reflect the vessel-generated waves and increase the ship resistance, and this effect gets stronger when the channel is narrower or the ice is thicker. The resistance increment is mainly attributed to the pressure component, caused by changes in the wave pattern due to the presence of the ice sheets. For the investigated container ship form, the channel can increase the ship's resistance by up to 15% of that in a pure open-water condition, and this relative increment is higher when the ship is operating at a lower velocity. The channel effect was most evident when its width is less than 2.5 times of the ship beam and when the ice thickness is greater than 5% of the ship draught; both the effective ranges are aligned to a practical ice channel created by icebreakers.

- When a ship is operating in floating ice floes, it is subjected to a considerable ice resistance resulting from the contacts between the ship and the floes. The magnitude of the ice-floe resistance can have the same order of the ship's open water resistance, which was found to be mainly dictated by ship beam, ship speed, ice concentration, ice thickness, and floe diameter. Regression analyses showed that ship speed and ice concentration govern the resistance with a power of 1.2 and 1.5 respectively, while ice thickness, floe diameter and ship beam revealed a linear relationship with the resistance. Using these relationships, a procedure was developed to express the ice-floe resistance as an empirical equation. The derived ice-floe resistance question was combined with classic naval architecture equations to facilitate a VPT that links with real-time metocean and ice data to calculate a ship's fuel consumption along potential routes, allowing ship operators to select routes with lower energy costs. This application was demonstrated and validated against full-scale measurements.

This work provided new models that can accurately simulate ship operation in floating ice floes and in open-water channels between ice sheets. The models can be applied to predict the ice resistance on a given ship. This will in turn allow naval architects to optimise ice-going vessels by comparing potential hull forms and comparing retrofits of a hull form; marine engineers to equip the vessels with adequate propulsion systems; and structural engineers to assess ice loads on a hull and plan scantlings to strengthen key areas.

The output of this work can also contribute to future international guidelines and regulations for polar maritime transportation. For example, based on the developed simulation approaches, associations such as the International Towing Tank Conference could develop a fuller guideline on how to model ship-wave-ice interactions. The findings regarding ice resistance on ships could help the International Maritime Organisation to extend their Polar Code to formulate advice on ship operations in floating ice floes and in open-water ice channels, and the Finnish-Swedish Ice Class Rules may do the same to expand their scenarios.

Moreover, this work provides higher education and research institutions with tools and knowledge to account for the transforming Arctic environment. As the Arctic used to be covered by continuous level ice all year round, new knowledge for the emerging ice-floe environment has been urgently required, not only for shipping, but also to gain a better understanding of global warming and how to deal with it. For example, contemporary climate models still cannot accurately predict Arctic ice evolution and global temperature change. One of the main reasons is that they need to improve the parametrisation that represents wave-ice interactions [37], because ocean waves propagating in the ice fields dictate the ice layout and the associated ice-reflected solar radiation. The provided computational models for wave-ice interactions could fill this gap and potentially help remedy the inaccuracies in current analytical methods.

Nevertheless, the applicability of this work is subjected to certain limitations. Firstly, the ice floes applied in all the simulations are currently assumed to remain intact following contact with a wave or ship. For wave-ice interactions, although ice deformation was considered in this work, the model would be unrealistic should the maximum stress inside the ice exceed its breaking threshold; this is unlikely to happen for scenarios analysed in this work, which focussed on common Arctic wave conditions that have a large wavelength and a small amplitude, but the limitation could be influential for scenarios including wave-induced ice fracture. For ship operations under ice conditions, the simulations' applicability is also limited to scenarios where ice fracture is negligible, such as the pancake ice condition studied in this work, where the floes are sufficiently small that their response to a moving ship is being pushed away rather than broken up.

It is also worth noting that computational simulations require a relatively long time to run, so they are not suitable for applications requiring rapid computing, e.g. real-time forecasting and optimisation. Nonetheless, the present work demonstrated a procedure to derive fast equations from simulation results, which can be a solution to get around this common limitation of similar computational approaches.

8.2 Recommendations for future research

This section suggests several research directions that can be conducted based on the accomplishments of this work:

- Following the limitation in current modelling methods, the present methods could be extended to include the capability to model ice fracture. Thus the work would be able to simulate wave-ice or ship-wave-ice interactions including icebreaking. A possible solution for this is to clump numerous DEM particles together to form one ice piece, and the DEM particles are connected through bonds. Appropriate criteria can be set to trigger the bonds to break, and then the ice piece can split. This DEM approach has already been made available but not yet validated in the current topic [173].

- Using the provided CFD+DEM approach, further analyses could be conducted on ship performance in ice-floe conditions. Extended simulations can be conducted to study the sensitivity of more advanced hull parameters and more diverse hull forms. On the other hand, more ice-floe shapes can be studied to investigate in what scenarios the floe shape is influential and how it changes the ship resistance. Based on extended simulations and validation, a more mature version of the ice-floe resistance equation could be developed, which will be a significant contribution as demonstrated for ship design and voyage planning. In addition, it will be of interest to investigate the seakeeping and manoeuvring of ships in floating ice floes.

- Further analyses can be carried out of wave-ice interactions in order to obtain insights into the transforming Arctic environment. For studying the MIZ, a two-way coupling CFD+DEM approach could be used to simulate the wave attenuation through a field of numerous ice floes, aiming to enhance current wave transmission and dissipation functions. Furthermore, the CFD+CSM simulation can obtain the maximal stress inside an ice sheet during a wave event and then compare this stress with the ice's breaking threshold, which can predict whether the ice should break; in this way, systematic simulations may give a function of the maximal ice dimension that can survive a specific wave condition.

- Beyond the applications of this work, the developed approaches could be applied to other engineering problems. The CFD+DEM method could also be used to assess ice impacts on other polar structures, such as lifeboats, offshore platforms and port facilities; alongside ships themselves, these installations are also essential for the safety and sustainability of the maritime Arctic. The hydroelastic CFD+CSM method can be used to simulate other deformable marine structures in waves or currents, such as to predict the relevant deformations of offshore wind turbines, bridges, and wavebreakers. The two-way fully coupled FSI algorithm allows the process to be simulated dynamically, presenting the flow change and load change whilst the structure is deforming; this would be a great improvement to current analyses used by designers, as contemporary methods still assume the structural deformations in a quasi-static way. Similarly, the method can model wave energy converters that are based on a deformation mechanism, e.g. the bulge type [174].

References

[1] J. Richter-Menge, J. Overland, and J. Mathis, *Arctic Report Card*. NOAA Arctic Programme, 2016.

[2] L. Dicks, *Arctic Climate Issues 2011: Changes in Arctic Snow, Water, Ice and Permafrost. SWIPA 2011 Overview Report.* Arctic Monitoring and Assessment Programme (AMAP), 2012.

[3] J. Cosmisco, C. Parkinson, T. Markus, D. Cavalieri, and R. Gersten, "Current state of the sea ice cover," *National Aeronautics and Space Administration*, 2016.

[4] Deshielo polo norte 1978-2010. GMES. [Online]. Available: https://www.youtube.com/watch?v=CpU6W8x23ME

[5] R. Kwok and D. Rothrock, "Decline in arctic sea ice thickness from submarine and icesat records: 1958–2008," *Geophysical Research Letters*, vol. 36, no. 15, 2009.

[6] A. Alberello, L. Bennetts, P. Heil, C. Eayrs, M. Vichi, K. Machutchon, M. Onorato, and A. Toffoli, "Drift of pancake ice floes in the winter Antarctic marginal ice zone during polar cyclones," *Journal of Geophysical Research: Oceans*, vol. 125, no. 3, 2020.

[7] P. Lu, Z. Li, Z. Zhang, and X. Dong, "Aerial observations of floe size distribution in the marginal ice zone of summer prydz bay," *Journal of Geophysical Research: Oceans*, vol. 113, no. C2, 2008.

[8] N. Melia, K. Haines, and E. Hawkins, "Future of the sea: implications from opening Arctic sea routes," Government Office for Science, Gov.uk., Tech. Rep., 2017.

[9] J. Gascard, K. Riemann-Campe, R. Gerdes, H. Schyberg, R. Randriamampianina, M. Karcher, J. Zhang, and M. Rafizadeh, "Future sea ice conditions and weather forecasts in the arctic: Implications for arctic shipping," *Ambio*, vol. 46, no. 3, pp. 355–367, 2017.

[10] V. Khon, I. Mokhov, M. Latif, V. Semenov, and W. Park, "Perspectives of northern sea route and northwest passage in the twenty-first century," *Climatic Change*, vol. 100, no. 3-4, pp. 757–768, 2010.

[11] L. Zhou, K. Riska, R. Polach, T. Moan, and B. Su, "Experiments on level ice loading on an icebreaking tanker with different ice drift angles," *Cold Regions Science and Technology*, vol. 85, pp. 79–93, 2013.

[12] L. Braesch. Icebreaker polar sea sidelined by engine troubles. Coast Guard. [Online]. Available: http://coastguard.dodlive.mil/2010/06/icebreaker-polar-sea-sidelined-by-engine-troubles/

[13] W. Luo, C. Guo, T. Wu, and Y. Su, "Experimental research on resistance and motion attitude variation of ship–wave–ice interaction in marginal ice zones," *Marine Structures*, vol. 58, pp. 399–415, 2018.

[14] J. Thomson, S. Ackley, F. Girard-Ardhuin, F. Ardhuin, A. Babanin, G. Boutin, J. Brozena, S. Cheng, C. Collins, M. Doble *et al.*, "Overview of the arctic sea state and boundary layer physics program," *Journal of Geophysical Research: Oceans*, 2018.

[15] S. Sun and H. Shen, "Simulation of pancake ice load on a circular cylinder in a wave and current field," *Cold Regions Science and Technology*, vol. 78, pp. 31–39, 2012.

[16] P. Schmitt, C. Windt, J. Davidson, J. Ringwood, and T. Whittaker, "Beyond vof: alternative openfoam solvers for numerical wave tanks," *Journal of ocean engineering and marine energy*, vol. 6, no. 3, pp. 277–292, 2020.

[17] A. Wimshurst, *Fluid Mechanics 101*. Youtube, 2021.

[18] D. Kuzmin, *A guide to numerical methods for transport equations*. University Erlangen-Nuremberg, 2010.

[19] L. Yiew, L. Bennetts, M. Meylan, B. French, and G. Thomas, "Hydrodynamic responses of a thin floating disk to regular waves," *Ocean Modelling*, vol. 97, pp. 52–64, 2016.

[20] D. Sree, A. Law, and H. Shen, "An experimental study on the interactions between surface waves and floating viscoelastic covers," *Wave Motion*, vol. 70, pp. 195–208, 2017.

[21] F. Nelli, L. Bennetts, D. Skene, J. Monty, J. Lee, M. Meylan, and A. Toffoli, "Reflection and transmission of regular water waves by a thin, floating plate," *Wave Motion*, vol. 70, pp. 209–221, 2017.

[22] D. Skene, L. Bennetts, M. Meylan, and A. Toffoli, "Modelling water wave overwash of a thin floating plate," *Journal of Fluid Mechanics*, vol. 777, 2015.

[23] C. Guo, C. Xie, J. Zhang, S. Wang, and D. Zhao, "Experimental investigation of the resistance performance and heave and pitch motions of ice-going container ship under pack ice conditions," *China Ocean Engineering*, vol. 32, no. 2, pp. 169–178, 2018.

[24] D. Colbourne, "Scaling pack ice and iceberg loads on moored ship shapes," *Oceanic engineering international*, vol. 4, no. 1, pp. 39–45, 2000.

[25] IACS, "Requirements concerning polar class," International Association of Classification Societies, Tech. Rep., 2016.

[26] J. Kim, Y. Kim, H. Kim, and S. Jeong, "Numerical simulation of ice impacts on ship hulls in broken ice fields," *Ocean Engineering*, vol. 180, pp. 162–174, 2019.

[27] Z. Li, J. Ringsberg, L. Ding, F. Rita, N. Fournier, and J. Mendes, "Safe and fuel-efficient voyage planning for the northeast passage by combining reliable ship performance, weather and ice forecast models," in *International Conference on Offshore Mechanics and Arctic Engineering*, vol. 84393. American Society of Mechanical Engineers, 2020, p. V007T07A005.

[28] R. Pachauri, M. Allen, V. Barros, J. Broome, W. Cramer, R. Christ, J. Church, L. Clarke, Q. Dahe, P. Dasgupta *et al.*, *Climate change 2014: synthesis report. Contribution of Working Groups I, II and III to the fifth assessment report of the Intergovernmental Panel on Climate Change*. IPCC, 2014.

[29] P. Wadhams, *A Farewell to Ice: A Report from the Arctic*. Oxford University Press, 2017.

[30] L. Smith and S. Stephenson, "New trans-Arctic shipping routes navigable by midcentury," *Proceedings of the National Academy of Sciences*, vol. 110, no. 13, pp. E1191–E1195, 2013.

[31] C. Hansen, P. Grønsedt, C. Graversen, and C. Hendriksen, *Arctic Shipping: Commercial Opportunities and Challenges*. CBS Maritime, 2016.

[32] S. Prinsenberg and I. K. Peterson, "Observing regional-scale pack-ice decay processes with helicopter-borne sensors and moored upward-looking sonars," *Annals of Glaciology*, vol. 52, no. 57, pp. 35–42, 2011.

[33] F. Montiel, V. Squire, and L. Bennetts, "Attenuation and directional spreading of ocean wave spectra in the marginal ice zone," *Journal of Fluid Mechanics*, vol. 790, pp. 492–522, 2016.

[34] C. Horvat, L. Roach, R. Tilling, C. Bitz, B. Fox-Kemper, C. Guider, K. Hill, A. Ridout, and A. Shepherd, "Estimating the sea ice floe size distribution using satellite altimetry: theory, climatology, and model comparison," *The Cryosphere*, vol. 13, no. 11, pp. 2869–2885, 2019.

[35] M. Steele, "Sea ice melting and floe geometry in a simple ice-ocean model," *Journal of Geophysical Research: Oceans*, vol. 97, no. C11, pp. 17 729–17 738, 1992.

[36] R. Massom and S. Stammerjohn, "Antarctic sea ice change and variability–physical and ecological implications," *Polar Science*, vol. 4, no. 2, pp. 149–186, 2010.

[37] V. Squire, "Ocean wave interactions with sea ice: a reappraisal," *Annual Review of Fluid Mechanics*, vol. 52, 2020.

[38] J. Stroeve, V. Kattsov, A. Barrett, M. Serreze, T. Pavlova, M. Holland, and W. Meier, "Trends in arctic sea ice extent from cmip5, cmip3 and observations," *Geophysical Research Letters*, vol. 39, no. 16, 2012.

[39] S. Laxon, K. Giles, A. Ridout, D. Wingham, R. Willatt, R. Cullen, R. Kwok, A. Schweiger, J. Zhang, C. Haas *et al.*, "Cryosat-2 estimates of Arctic sea ice thickness and volume," *Geophysical Research Letters*, vol. 40, no. 4, pp. 732–737, 2013.

[40] C. Deser and H. Teng, "Evolution of Arctic sea ice concentration trends and the role of atmospheric circulation forcing, 1979–2007," *Geophysical Research Letters*, vol. 35, no. 2, 2008.

[41] The marginal ice zone. Norwegian Polar Institute. [Online]. Available: http://www.npolar.no/en/facts/the-marginal-ice-zone.html

[42] C. Strong and I. G. Rigor, "Arctic marginal ice zone trending wider in summer and narrower in winter," *Geophysical Research Letters*, vol. 40, no. 18, pp. 4864–4868, 2013.

[43] SEDNA. Safe maritime operations under extreme conditions: the Arctic case. [Online]. Available: https://www.sedna-project.eu/

[44] D. Gautier, K. Bird, R. Charpentier, A. Grantz, D. Houseknecht, T. Klett, T. Moore, J. Pitman, C. Schenk, J. Schuenemeyer *et al.*, "Assessment of undiscovered oil and gas in the Arctic," *Science*, vol. 324, no. 5931, pp. 1175–1179, 2009.

[45] A. Anderson, *After the ice: Life, death and politics in the New Arctic*. Random House, 2009.

[46] S. Martin and P. Becker, "High-frequency ice floe collisions in the greenland sea during the 1984 marginal ice zone experiment," *Journal of Geophysical Research: Oceans*, vol. 92, no. C7, pp. 7071–7084, 1987.

[47] P. Wadhams, "A mechanism for the formation of ice edge bands," *Journal of Geophysical Research: Oceans*, vol. 88, no. C5, pp. 2813–2818, 1983.

[48] M. Dai, H. H. Shen, M. A. Hopkins, and S. F. Ackley, "Wave rafting and the equilibrium pancake ice cover thickness," *Journal of Geophysical Research: Oceans*, vol. 109, no. C7, 2004.

[49] M. Meylan, L. Yiew, L. Bennetts, B. French, and G. Thomas, "Surge motion of an ice floe in waves: comparison of a theoretical and an experimental model," *Annals of Glaciology*, vol. 56, no. 69, pp. 155–159, 2015.

[50] R. Grotmaack and M. Meylan, "Wave forcing of small floating bodies," *Journal of waterway, port, coastal, and ocean engineering*, vol. 132, no. 3, pp. 192–198, 2006.

[51] M. Meylan and V. Squire, "Response of a circular ice floe to ocean waves," *Journal of Geophysical Research: Oceans*, vol. 101, no. C4, pp. 8869–8884, 1996.

[52] F. Montiel, "Numerical and experimental analysis of water wave scattering by floating elastic plates," Ph.D. dissertation, University of Otago, 2012.

[53] H. Jasak, "CFD analysis in subsea and marine technology," in *IOP Conference Series: Materials Science and Engineering*, vol. 276, no. 1. IOP Publishing, 2017.

[54] W. Bai, T. Zhang, and D. McGovern, "Response of small sea ice floes in regular waves: a comparison of numerical and experimental results," *Ocean Engineering*, vol. 129, pp. 495–506, 2017.

[55] H. Jasak, A. Jemcov, and Z. Tukovic, "OpenFOAM: a C++ library for complex physics simulations," in *International workshop on coupled methods in numerical dynamics*. IUC Dubrovnik, Croatia, 2007.

[56] V. Squire, "Past, present and impendent hydroelastic challenges in the polar and subpolar seas," *Philosophical Transactions of the Royal Society of London A: Mathematical, Physical and Engineering Sciences*, vol. 369, no. 1947, pp. 2813–2831, 2011.

[57] M. Meylan, L. Bennetts, C. Cavaliere, A. Alberello, and A. Toffoli, "Experimental and theoretical models of wave-induced flexure of a sea ice floe," *Physics of Fluids*, vol. 27, no. 4, 2015.

[58] D. Sree, A. Law, and H. Shen, "An experimental study on gravity waves through a floating viscoelastic cover," *Cold Regions Science and Technology*, vol. 155, pp. 289–299, 2018.

[59] A. Dolatshah, F. Nelli, L. Bennetts, A. Alberello, M. Meylan, J. Monty, and A. Toffoli, "Letter: Hydroelastic interactions between water waves and floating freshwater ice," *Physics of Fluids*, vol. 30, no. 9, 2018.

[60] V. Squire, "Synergies between VLFS hydroelasticity and sea-ice research," in *18th International Offshore and Polar Engineering Conference*. International Society of Offshore and Polar Engineers, 2008.

[61] C. Fox and V. Squire, "On the oblique reflexion and transmission of ocean waves at shore fast sea ice," *Phil. Trans. R. Soc. Lond. A*, vol. 347, no. 1682, pp. 185–218, 1994.

[62] H. Chung and C. Fox, "Calculation of wave-ice interaction using the wiener-hopf technique," *New Zealand J. Math*, vol. 31, no. 1, pp. 1–18, 2002.

[63] A. Hermans, "Free-surface wave interaction with a thick flexible dock or very large floating platform," *Journal of Engineering Mathematics*, vol. 58, no. 1-4, pp. 77–90, 2007.

[64] L. Bennetts, N. Biggs, and D. Porter, "A multi-mode approximation to wave scattering by ice sheets of varying thickness," *Journal of Fluid Mechanics*, vol. 579, pp. 413–443, 2007.

[65] T. Williams and V. Squire, "The effect of submergence on wave scattering across a transition between two floating flexible plates," *Wave Motion*, vol. 45, no. 3, pp. 361–379, 2008.

[66] T. Williams and R. Porter, "The effect of submergence on the scattering by the interface between two semi-infinite sheets," *Journal of Fluids and Structures*, vol. 25, no. 5, pp. 777–793, 2009.

[67] M. Meylan and V. Squire, "Finite-floe wave reflection and transmission coefficients from a semi-infinite model," *Journal of Geophysical Research: Oceans*, vol. 98, no. C7, pp. 12 537–12 542, 1993.

[68] Meylan, Michael and Squire, V, "The response of ice floes to ocean waves," *Journal of Geophysical Research: Oceans*, vol. 99, no. C1, pp. 891–900, 1994.

[69] C. Wang and M. Meylan, "A higher-order-coupled boundary element and finite element method for the wave forcing of a floating elastic plate," *Journal of Fluids and Structures*, vol. 19, no. 4, pp. 557–572, 2004.

[70] M. Smith and M. Meylan, "Wave scattering by an ice floe of variable thickness," *Cold Regions Science and Technology*, vol. 67, no. 1-2, pp. 24–30, 2011.

[71] A. Toffoli, L. Bennetts, M. Meylan, C. Cavaliere, A. Alberello, J. Elsnab, and J. Monty, "Sea ice floes dissipate the energy of steep ocean waves," *Geophysical Research Letters*, vol. 42, no. 20, pp. 8547–8554, 2015.

[72] Z. Tukovic and H. Jasak, "Updated lagrangian finite volume solver for large deformation dynamic response of elastic body," *Transactions of FAMENA*, vol. 31, no. 1, 2007.

[73] Z. Tukovic, P. Cardiff, A. Karac, H. Jasak, and A. Ivankovic, "OpenFOAM library for fluid structure interaction," in *The 9th OpenFOAM Workshop*, 2014.

[74] Ž. Tuković, A. Ivanković, and A. Karač, "Finite-volume stress analysis in multi-material linear elastic body," *International journal for numerical methods in engineering*, vol. 93, no. 4, pp. 400–419, 2013.

[75] T. Tang, O. Hededal, and P. Cardiff, "On finite volume method implementation of poro-elasto-plasticity soil model," *International journal for numerical and analytical methods in geomechanics*, vol. 39, no. 13, pp. 1410–1430, 2015.

[76] P. Cardiff, A. Karač, P. De Jaeger, H. Jasak, J. Nagy, A. Ivanković, and Ž. Tuković, "An open-source finite volume toolbox for solid mechanics and fluid-solid interaction simulations," *arXiv preprint arXiv:1808.10736*, 2018.

[77] K. Rege and B. Hjertager, "Application of foam-extend on turbulent fluid-structure interaction," in *IOP Conference Series: Materials Science and Engineering*, vol. 276, no. 1. IOP Publishing, 2017.

[78] C. Hirt and B. Nichols, "Volume of fluid (VOF) method for the dynamics of free boundaries," *Journal of computational physics*, vol. 39, no. 1, pp. 201–225, 1981.

[79] S. Jeong, K. Choi, K. Kang, and J. Ha, "Prediction of ship resistance in level ice based on empirical approach," *International Journal of Naval Architecture and Ocean Engineering*, vol. 9, no. 6, pp. 613–623, 2017.

[80] D. Myland and S. Ehlers, "Theoretical investigation on ice resistance prediction methods for ships in level ice," in *ASME 2014 33rd International Conference on Ocean, Offshore and Arctic Engineering*. American Society of Mechanical Engineers, 2014, pp. V010T07A015–V010T07A015.

[81] J. Tatinclaux, "Model tests on two models of wtgb 140-foot icebreaker," Cold Regions Research and Engineering Lab Hanover NH, Tech. Rep., 1984.

[82] A. Freitas and R. Nishizaki, "Model test of an ice class bulk carrier with the thyssen/waas bow form," *Journal of energy resources technology*, vol. 108, no. 2, pp. 168–172, 1986.

[83] E. Enkvist, "On the ice resistance encountered by ships operating in the continuous mode of icebreaking," Swedish Academy of Engineering Sciences in Finland. Report no. 24, Tech. Rep., 1972.

[84] G. Lindqvist, "A straightforward method for calculation of ice resistance of ships," in *The 10th International Conference on Port and Ocean Engineering Under Arctic Conditions, POAC89*, 1989.

[85] K. Riska, "Performance of merchant vessels in ice in the baltic," Helsinki University of Technology, Ship Laboratory, Tech. Rep., 1997.

[86] J. Hu and L. Zhou, "Experimental and numerical study on ice resistance for icebreaking vessels," *International Journal of Naval Architecture and Ocean Engineering*, vol. 7, no. 3, pp. 626–639, 2015.

[87] F. Li, M. Kotilainen, F. Goerlandt, and P. Kujala, "An extended ice failure model to improve the fidelity of icebreaking pattern in numerical simulation of ship performance in level ice," *Ocean Engineering*, vol. 176, pp. 169–183, 2019.

[88] F. Li, M. Kõrgesaar, P. Kujala, and F. Goerlandt, "Finite element based metamodeling of ship-ice interaction at shoulder and midship areas for ship performance simulation," *Marine Structures*, vol. 71, p. 102736, 2020.

[89] F. Li, F. Goerlandt, and P. Kujala, "Numerical simulation of ship performance in level ice: A framework and a model," *Applied Ocean Research*, vol. 102, 2020.

[90] Y. Xue, R. Liu, Z. Li, and D. Han, "A review for numerical simulation methods of ship–ice interaction," *Ocean Engineering*, vol. 215, 2020.

[91] T. Kitazawa and R. Ettema, "Resistance to ship-hull motion through brash ice," *Cold Regions Science and Technology*, vol. 10, no. 3, pp. 219–234, 1985.

[92] T. Kitazawa and R. Ettema, "Guidelines for the application the Finnish-Swedish ice class rules," Finnish Transport and Communications Agency, Tech. Rep., 2011.

[93] S. Jeong, J. Jang, K. Kang, and H. Kim, "Implementation of ship performance test in brash ice channel," *Ocean Engineering*, vol. 140, pp. 57–65, 2017.

[94] A. Konno, O. Saitoh, and Y. Watanabe, "Numerical investigation of effect of channel condition against ships resistance in brash ice channels," in *The 21st International Conference on Port and Ocean Engineering Under Arctic Conditions, POAC11*, 2011.

[95] P. Cundall and O. Strack, "A discrete numerical model for granular assemblies," *geotechnique*, vol. 29, no. 1, pp. 47–65, 1979.

[96] J. Tuhkuri and A. Polojärvi, "A review of discrete element simulation of ice–structure interaction," *Philosophical Transactions of the Royal Society A: Mathematical, Physical and Engineering Sciences*, vol. 376, no. 2129, p. 20170335, 2018.

[97] A. Konno, A. Nakane, and S. Kanamori, "Validation of numerical estimation of brash ice channel resistance with model test," in *Proceedings of the International Conference on Port and Ocean Engineering Under Arctic Conditions*, 2013.

[98] W. Luo, D. Jiang, T. Wu, C. Guo, C. Wang, R. Deng, and S. Dai, "Numerical simulation of an ice-strengthened bulk carrier in brash ice channel," *Ocean Engineering*, vol. 196, 2020.

[99] P. Koskinen and J. Savikurki, "A propulsion system based on azimuth thrusters and its possibilities in icebreaking technology," in *The 12th International Conference on Port and Ocean Engineering Under Arctic Conditions, POAC93*, 1993, pp. 249–258.

[100] T. Leiviskä, J. Tuhkuri, and K. Riska, "Model test on resistance in ice-free ice channels," in *The 16th International Conference on Port and Ocean Engineering Under Arctic Conditions, POAC01*, 2001.

[101] T. Heinonen, "Kokeellinen tutkimus nopeuden vaikutuksesta laivan jaavastukseen (Finnish)," Master's thesis, Helsinki University of Technology, 2010.

[102] M. Terziev, T. Tezdogan, E. Oguz, T. Gourlay, Y. Demirel, and A. Incecik, "Numerical investigation of the behaviour and performance of ships advancing through restricted shallow waters," *Journal of Fluids and Structures*, vol. 76, pp. 185–215, 2018.

[103] P. Mucha, G. Deng, T. Gourlay, E. Moctar, and B. Ould, "Validation studies on numerical prediction of ship squat and resistance in shallow water," in *4th MASHCON-International Conference on Ship Manoeuvring in Shallow and Confined Water with Special Focus on Ship Bottom Interaction*, 2016, pp. 122–133.

[104] E. Hansen and S. Løset, "Modelling floating offshore units moored in broken ice: comparing simulations with ice tank tests," *Cold regions science and technology*, vol. 29, no. 2, pp. 107–119, 1999.

[105] M. Lau, K. Lawrence, and L. Rothenburg, "Discrete element analysis of ice loads on ships and structures," *Ships and Offshore Structures*, vol. 6, no. 3, pp. 211–221, 2011.

[106] S. Ji, Z. Li, C. Li, and J. Shang, "Discrete element modeling of ice loads on ship hulls in broken ice fields," *Acta Oceanologica Sinica*, vol. 32, no. 11, pp. 50–58, 2013.

[107] J. Wackers, B. Koren, H. C. Raven, A. Van der Ploeg, A. Starke, G. Deng, P. Queutey, M. Visonneau, T. Hino, and K. Ohashi, "Free-surface viscous flow solution methods for ship hydrodynamics," *Archives of Computational Methods in Engineering*, vol. 18, no. 1, pp. 1–41, 2011.

[108] C. Janßen, D. Mierke, and T. Rung, "On the development of an efficient numerical ice tank for the simulation of fluid-ship-rigid-ice interactions on graphics processing units," *Computers & Fluids*, vol. 155, pp. 22–32, 2017.

[109] S. Mintu and D. Molyneux, "Simulation of ice-structure interactions using a coupled SPH-DEM method," in *OTC Arctic Technology Conference*. Offshore Technology Conference, 2018.

[110] A. Alberello, M. Onorato, L. Bennetts, M. Vichi, C. Eayrs, K. MacHutchon, and A. Toffoli, "Brief communication: Pancake ice floe size distribution during the winter expansion of the Antarctic marginal ice zone," *The Cryosphere*, vol. 13, no. 1, pp. 41–48, 2019.

[111] D. Wilcox, *Turbulence modeling for CFD*. DCW industries La Canada, CA, 1998, vol. 2.

[112] B. Launder and B. Sharma, "Application of the energy-dissipation model of turbulence to the calculation of flow near a spinning disc," *Letters in heat and mass transfer*, vol. 1, no. 2, pp. 131–137, 1974.

[113] H. Weller, "Derivation, modelling and solution of the conditionally averaged two-phase flow equations," in *Technical Report TR/HGW/02*. Nabla Ltd, 2002.

[114] H. Rusche, "Computational fluid dynamics of dispersed two-phase flows at high phase fractions," Ph.D. dissertation, Imperial College London (University of London), 2003.

[115] V. Vukčević, "Numerical modelling of coupled potential and viscous flow for marine applications," Ph.D. dissertation, University of Zagreb, 2016.

[116] R. Dean and R. Dalrymple, *Water wave mechanics for engineers and scientists*. World Scientific Publishing Company, 1991, vol. 2.

[117] G. Wei, "The sponge layer method in FLOW-3D," Flow Science Report 07-15, Tech. Rep., 2015.

[118] Ž. Tuković, A. Karač, P. Cardiff, H. Jasak, and A. Ivanković, "OpenFOAM finite volume solver for fluid-solid interaction," *Transactions of FAMENA*, vol. 42, no. 3, pp. 1–31, 2018.

[119] M. Hopkins and J. Tuhkuri, "Compression of floating ice fields," *Journal of Geophysical Research: Oceans*, vol. 104, no. C7, pp. 15 815–15 825, 1999.

[120] G. Timco and W. Weeks, "A review of the engineering properties of sea ice," *Cold regions science and technology*, vol. 60, no. 2, pp. 107–129, 2010.

[121] H. Versteeg and W. Malalasekera, *An introduction to computational fluid dynamics: the finite volume method*. Pearson Education, 2007.

[122] H. Jasak, "Error analysis and estimation for the finite volume method with applications to fluid flows," Ph.D. dissertation, Imperial College London (University of London), 1996.

[123] M. Bhinder, C. Mingham, D. Causon, M. Rahmati, G. Aggidis, and R. Chaplin, "A joint numerical and experimental study of a surging point absorbing wave energy converter (wraspa)," in *ASME 2009 28th International Conference on Ocean, Offshore and Arctic Engineering*. American Society of Mechanical Engineers, 2009, pp. 869–875.

[124] Flow Science Inc, "Flow-3D user's manual, v11.1," 2015.

[125] V. Yakhot and S. A. Orszag, "Renormalization group analysis of turbulence. i. basic theory," *Journal of scientific computing*, vol. 1, no. 1, pp. 3–51, 1986.

[126] K. Connell and A. Cashman, "Development of a numerical wave tank with reduced discretization error," in *2016 International Conference on Electrical, Electronics, and Optimization Techniques (ICEEOT)*. IEEE, 2016, pp. 3008–3012.

[127] C. Freitas, "The issue of numerical uncertainty," *Applied Mathematical Modelling*, vol. 26, no. 2, pp. 237–248, 2002.

[128] L. Bennetts and T. Williams, "Water wave transmission by an array of floating discs," in *Proceedings of the Royal Society of London A: Mathematical, Physical and Engineering Sciences*, vol. 471, no. 2173. The Royal Society, 2015.

[129] Ž. Tuković and H. Jasak, "A moving mesh finite volume interface tracking method for surface tension dominated interfacial fluid flow," *Computers & fluids*, vol. 55, pp. 70–84, 2012.

[130] J. McVicar, J. Lavroff, M. Davis, and G. Thomas, "Fluid–structure interaction simulation of slam-induced bending in large high-speed wave-piercing catamarans," *Journal of Fluids and Structures*, vol. 82, pp. 35–58, 2018.

[131] M. Masoomi and A. Mosavi, "The one-way fsi method based on rans-fem for the open water test of a marine propeller at the different loading conditions," *Journal of Marine Science and Engineering*, vol. 9, no. 4, 2021.

[132] N. Di Domenico, C. Groth, A. Wade, T. Berg, and M. Biancolini, "Fluid structure interaction analysis: vortex shedding induced vibrations," *Procedia Structural Integrity*, vol. 8, pp. 422–432, 2018.

[133] C. Groth, U. Cella, E. Costa, and M. Biancolini, "Fast high fidelity cfd/csm fluid structure interaction using rbf mesh morphing and modal superposition method," *Aircraft Engineering and Aerospace Technology*, 2019.

[134] H. Jellinek and R. Brill, "Viscoelastic properties of ice," *Journal of Applied Physics*, vol. 27, no. 10, pp. 1198–1209, 1956.

[135] S. Beltaos, "Wave-generated fractures in river ice covers," *Cold Regions Science and Technology*, vol. 40, no. 3, pp. 179–191, 2004.

[136] W. Kim, S. Van, and D. Kim, "Measurement of flows around modern commercial ship models," *Experiments in fluids*, vol. 31, no. 5, pp. 567–578, 2001.

[137] Z. Zhang, L. Hui, S. Zhu, and Z. Feng, "Application of cfd in ship engineering design practice and ship hydrodynamics," *Journal of Hydrodynamics, Ser. B*, vol. 18, no. 3, pp. 315–322, 2006.

[138] ITTC, "Guidelines: Practical guidelines for ship CFD applications," International Towing Tank Conference, Tech. Rep., 2014.

[139] T. Phillips and C. Roy, "A new extrapolation-based uncertainty estimator for computational fluid dynamics," *Journal of Verification, Validation and Uncertainty Quantification*, vol. 1, no. 4, 2016.

[140] ITTC, "Uncertainty analysis in CFD: verification and validation methodology and procedures," International Towing Tank Conference, Tech. Rep., 2008.

[141] I. Celik, U. Ghia, P. Roache, C. Freitas, H. Coleman, P. Raad, Ì. Celik, C. Freitas, and H. Coleman, "Procedure for estimation and reporting of uncertainty due to discretization in CFD applications," 2008.

[142] T. Gourlay, J. Ha, P. Mucha, and K. Uliczka, "Sinkage and trim of modern container ships in shallow water," in *Australasian Coasts & Ports Conference 2015: 22nd Australasian Coastal and Ocean Engineering Conference and the 15th Australasian Port and Harbour Conference*. Engineers Australia and IPENZ, 2015, p. 344.

[143] P. Mucha, O. el Moctar, T. Dettmann, and M. Tenzer, "An experimental study on the effect of confined water on resistance and propulsion of an inland waterway ship," *Ocean Engineering*, vol. 167, pp. 11–22, 2018.

[144] M. Juva and K. Riska, "On the power requirement in the Finnish-Swedish ice class rules," *Winter Navigation Research Board*, vol. 53, 2002.

[145] F. Menter, "Zonal two equation kw turbulence models for aerodynamic flows," in *23rd fluid dynamics, plasmadynamics, and lasers conference*, 1993, p. 2906.

[146] O. Baran, "Discrete element method in STAR-CCM+," in *STAR Japanese conference*, 2012.

[147] A. Polojärvi, J. Tuhkuri, and O. Korkalo, “Comparison and analysis of experimental and virtual laboratory scale punch through tests,” *Cold regions science and technology*, vol. 81, pp. 11–25, 2012.

[148] P. Mucha, “Fully-coupled cfd-dem for simulations of ships advancing through brash ice,” in *SNAME Maritime Convention*. The Society of Naval Architects and Marine Engineers, 2019.

[149] F. Parmiggiani, M. Moctezuma-Flores, P. Wadhams, and G. Aulicino, “Image processing for pancake ice detection and size distribution computation,” *International journal of remote sensing*, vol. 40, no. 9, pp. 3368–3383, 2019.

[150] J. Holland, *Adaptation in natural and artificial systems: an introductory analysis with applications to biology, control, and artificial intelligence*. MIT press, 1992.

[151] M. van den Berg, R. Lubbad, and S. Løset, “The effect of ice floe shape on the load experienced by vertical-sided structures interacting with a broken ice field,” *Marine Structures*, vol. 65, pp. 229–248, 2019.

[152] J. Paavilainen and J. Tuhkuri, “Pressure distributions and force chains during simulated ice rubbling against sloped structures,” *Cold Regions Science and Technology*, vol. 85, pp. 157–174, 2013.

[153] A. Polojärvi, J. Tuhkuri, and A. Pustogvar, “Dem simulations of direct shear box experiments of ice rubble: Force chains and peak loads,” *Cold Regions Science and Technology*, vol. 116, pp. 12–23, 2015.

[154] H. Gong, A. Polojärvi, and J. Tuhkuri, “Discrete element simulation of the resistance of a ship in unconsolidated ridges,” *Cold Regions Science and Technology*, vol. 167, p. 102855, 2019.

[155] M. Kim, W. Lee, and Y. Shin, “Comparative study on the resistance performance of an icebreaking cargo vessel according to the variation of waterline angles in pack ice conditions,” *International Journal of Naval Architecture and Ocean Engineering*, vol. 6, no. 4, pp. 876–893, 2014.

[156] F. Noblesse, G. Delhommeau, M. Guilbaud, and C. Yang, “The rise of water at a ship stem,” *Journal of ship research*, vol. 52, no. 2, pp. 89–101, 2008.

[157] A. Grech La Rosa, G. Thomas, E. Muk-Pavic, and T. Dinham-Peren, “Bulbous bows for energy efficient ships: A novel approach,” in *RINA Energy Efficient Ships Conference*, 2015.

[158] A. Milaković, F. Li, M. Marouf, and S. Ehlers, “A machine learning-based method for simulation of ship speed profile in a complex ice field,” *Ships and Offshore Structures*, vol. 15, no. 9, pp. 974–980, 2020.

[159] B. Pena, L. Huang, and F. Ahlgren, “A review on applications of machine learning in shipping sustainability,” in *SNAME Maritime Convention*. The Society of Naval Architects and Marine Engineers, 2020.

[160] B. Pena and L. Huang, “Wave-GAN: a deep learning approach for the prediction of nonlinear regular wave loads and run-up on a fixed cylinder,” *Coastal Engineering*, vol. 167, 2021.

[161] ITTC, “1978 ITTC performance prediction method,” International Towing Tank Conference, Tech. Rep., 2017.

[162] ITTC, “General guidance and introduction to ice model test,” International Towing Tank Conference, Tech. Rep., 2017.

[163] Z. Li, C. Ryan, L. Huang, L. Ding, J. Ringsberg, and G. Thomas, “A comparison of two ship performance models against full-scale measurements on a cargo ship on the northern sea route,” *Ships and Offshore Structures*, pp. 1–8, 2021.

[164] J. Calleya, “Ship design decision support for a carbon dioxide constrained future,” Ph.D. dissertation, UCL (University College London), 2014.

[165] F. Tillig, J. Ringsberg, W. Mao, and B. Ramne, “A generic energy systems model for efficient ship design and operation,” *Proceedings of the Institution of Mechanical Engineers, Part M: Journal of Engineering for the Maritime Environment*, vol. 231, no. 2, pp. 649–666, 2017.

[166] F. Tillig, “Simulation model of a ship’s energy performance and transportation costs,” Ph.D. dissertation, Chalmers University of Technology, 2020.

[167] A. Milaković, F. Li, R. Polach, and S. Ehlers, “Equivalent ice thickness in ship ice transit simulations: overview of existing definitions and proposition of an improved one,” *Ship Technology Research*, vol. 67, no. 2, pp. 84–100, 2020.

[168] E. Fiedler, M. Martin, E. Blockley, D. Lea, and N. Fournier, “Future of the sea: implications from opening Arctic sea routes,” *Report. SEDNA D3.1*, 2019.

[169] Z. Li, J. Ringsberg, and F. Rita, “A voyage planning tool for ships sailing between Arctic and Arctic via the Arctic,” *Ships and Offshore Structures*, pp. 1–10, 2020.

[170] IACS, “POLARIS–proposed system for determining operational limitations in ice,” International Association of Classification Societies, Tech. Rep., 2014.

[171] C. Ryan, D. Stagonas, and T. G, “Arctic shipping trends 2050,” University College London, Tech. Rep., 2021.

[172] Y. Peng, Z. Li, W. Duan, X. Li, and Q. Bao, “Evolution of the hinterlands of eight chinese ports exporting to europe under the polar silk road: Three hypothetical scenarios,” *Ocean & Coastal Management*, vol. 205, 2021.

[173] S. Bateman, M. Orzech, and J. Calantoni, “Simulating the mechanics of sea ice using the discrete element method,” *Mechanics Research Communications*, vol. 99, pp. 73–78, 2019.

[174] J. Chaplin, V. Heller, F. Farley, G. Hearn, and R. Rainey, “Laboratory testing the anaconda,” *Philosophical Transactions of the Royal Society A: Mathematical, Physical and Engineering Sciences*, vol. 370, no. 1959, pp. 403–424, 2012.